Doklady Physics, Vol. 47, No. 12, 2002, pp. 839–841. Translated from Doklady Akademii Nauk, Vol. 387, No. 4, 2002, pp. 468–470.

PHYSICS

Formulation of the Shafranov Method for Rotating Plasma

N. D. Naumov

Presented by Academician A.F. Andreev August 12, 2002

Received June 3, 2002

The development of methods for constructing exact solutions to a nonlinear system of equations of magnetic hydrodynamics is of undoubted interest. The Shafranov method [1] is applied to an axisymmetric configuration of immobile plasma bounded in space. This method allows us to reduce the system of equations

$$\operatorname{div}\mathbf{B} = 0, \quad \frac{1}{4\pi}[\mathbf{B}\operatorname{curl}\mathbf{B}] + \nabla p = 0$$

to the solution of the equation

$$\operatorname{div}\frac{\nabla\psi}{r^2} = -16\pi^3\frac{dP}{d\psi} - \frac{8\pi^2}{c^2r^2}\frac{dJ^2}{d\psi}. \quad (1)$$

Here, $p = P(\psi)$ is the plasma pressure and $\psi(r, z)$, $J(\psi)$ are the magnetic flux and the total electric-current across a circle of the radius r, which is perpendicular to the z axis:

$$\psi = \int_0^r B_z 2\pi r dr, \quad J = \int_0^r j_z \times 2\pi r dr.$$

In this paper, we analyze a system of steady-state equations of magnetic hydrodynamics [2]:

$$\operatorname{curl}[\mathbf{VB}] = 0, \quad \operatorname{div}\rho\mathbf{V} = 0, \quad (2)$$

$$\rho(\mathbf{V}\nabla)\mathbf{V} = -\frac{1}{4\pi}[\mathbf{B}\operatorname{curl}\mathbf{B}] - \nabla p. \quad (3)$$

The problem posed is to formulate a method for constructing a solution to the system of Eqs. (2) and (3) for an axisymmetric plasma configuration rotating as a single whole. This construction is realized on the basis of a known solution to Eq. (1) for the same configuration of the immobile plasma.

For $\mathbf{V} = V_\varphi\mathbf{e}_\varphi$, the condition for magnetic-field line freezing-in in the case of an axially symmetric plasma configuration has the form

$$\frac{\partial V_\varphi B_r}{\partial r} + \frac{\partial V_\varphi B_z}{\partial z} = 0. \quad (4)$$

Clearly, this condition is fulfilled for $V_\varphi = \Omega r$, where Ω is a constant value since, in this case, expression (4) is equivalent to the condition $\operatorname{div}\mathbf{B} = 0$.

It is evident that, in order to confine a rotating plasma configuration, we need to use another distribution of the electric-current density as compared to the case of an immobile plasma. First, we consider the particular case when, in the rotating plasma, only the total current varies across the circle of radius r, which is perpendicular to the z-axis, whereas the azimuth component of the current density conserves the previous form.

We now denote by G the total current across the circle of radius r and substitute expressions for the magnetic-field components

$$B_r = -\frac{1}{2\pi r}\frac{\partial\psi}{\partial z}, \quad B_\varphi = \frac{2G}{cr}, \quad B_z = \frac{1}{2\pi r}\frac{\partial\psi}{\partial r}$$

into Euler equation (3) with account of Shafranov Eq. (1) for immobile plasma. Then, we arrive at the following equations:

$$\rho\Omega^2 r = \frac{\partial}{\partial r}(P - p) - \frac{1}{2\pi c^2 r^2}\frac{\partial F}{\partial r}, \quad (5)$$

$$\frac{\partial\psi}{\partial r}\frac{\partial G}{\partial z} = \frac{\partial\psi}{\partial z}\frac{\partial G}{\partial r}, \quad (6)$$

$$\frac{\partial}{\partial z}\left(p + \frac{F}{2\pi c^2 r^2} - P\right) = 0. \quad (7)$$

Here, the notation $F = G^2 - J^2$ is introduced.

It follows from Eq. (6) that the function G depends on the coordinates in the same manner as the function J: $G = G(\psi)$. Since the boundary of the plasma configuration is determined by the condition $\psi(r, z) = C$, where C is a certain constant value, the function $P(\psi)$ satisfies the condition $P(C) = 0$. Therefore, with allowance for vanishing pressure on the surface of the configuration, we find from Eq. (7) for the rotating plasma

$$p = P(\psi) - \frac{1}{2\pi c^2 r^2}[F(\psi) - F(C)]. \quad (8)$$

1028-3358/02/4712-0839$22.00

In contrast to the case of immobile plasma, whose density is not determined concretely when constructing a solution for axisymmetric configurations, the density of rotating plasma, as follows from Eq. (5), has a definite form:

$$\rho = \frac{1}{\pi c^2 r^4 \Omega^2}[F(\psi) - F(C)]. \quad (9)$$

The obvious limitation when choosing the function G is providing both nonnegative values of functions (8) and (9) and the absence of singularities in the region occupied with plasma. It is worth noting that expressions (8) and (9) correspond to the known procedure of allowance for a centrifugal force in the rotating coordinate system by means of introducing an effective pressure [3]

$$p = P(\psi) - \frac{1}{2}\rho\Omega^2 r^2.$$

As a particular example, we consider a spherical configuration of immobile plasma [1], for which the solution is similar to the hydrodynamic Hill vortex:

$$\psi = \frac{3}{2}\pi B_0 r^2\left(\frac{r^2 + z^2}{R^2} - 1\right).$$

Here, B_0 is the magnitude of the external confining uniform magnetic field and R is the radius of the plasma ball whose surface is defined by the condition $\psi = 0$. For this configuration, the current density is distributed in the azimuth direction: $j_\varphi = -\frac{15cB_0 r}{8\pi R^2}$, $J = 0$, and the function P linearly depends on the magnetic flux: $P(\psi) = -\frac{15B_0\psi}{16\pi^2 R^2}$.

It follows from expression (9) that for the configuration under consideration and the choice $G(\psi) = \alpha\psi^\beta$, the density of the rotating plasma in the case $\beta \geq 1$ has a finite value at the origin. In particular, assuming $\beta = 1$, $\alpha = \frac{Ac}{R}$, where A is a certain constant, we find the following solution to the system of equations (2) and (3):

$$\rho = \frac{9}{4}\pi\left[\frac{AB_0}{R\Omega}\left(1 - \frac{r^2 + z^2}{R^2}\right)\right]^2, \quad \mathbf{V} = \Omega r\mathbf{e}_\varphi, \quad (10)$$

$$B_r = -B_0\frac{3rz}{2R^2}, \quad B_\varphi = 3\pi AB_0\frac{r}{R}\left(\frac{r^2 + z^2}{R^2} - 1\right),$$

$$B_z = \frac{3}{2}B_0\left(\frac{2r^2 + z^2}{R^2} - 1\right),$$

$$p = \frac{45B_0^2}{32\pi R^2}r^2\left(1 - \frac{r^2 + z^2}{R^2}\right)\left[1 - \frac{4}{5}\pi^2 A^2\left(1 - \frac{r^2 + z^2}{R^2}\right)\right].$$

It is evident that the plasma pressure has nonnegative values inside the sphere of the radius R for $A \leq \frac{\sqrt{5}}{2\pi}$.

In the other variant of constructing a solution to the system of equations (2) and (3), the radial and axial components of the current density in the rotating plasma have the same form as for the immobile plasma, and only the azimuth component of the current density changes its form:

$$j_\varphi = -\frac{kc}{8\pi^2 r}\left(\frac{\partial^2\psi}{\partial r^2} - \frac{1}{r}\frac{\partial\psi}{\partial r} + \frac{\partial^2\psi}{\partial z^2}\right).$$

Here, k is a constant. In this case, the components of the magnetic field in the rotating plasma can be written out in the form

$$B_r = -\frac{k}{2\pi r}\frac{\partial\psi}{\partial z}, \quad B_\varphi = \frac{2J}{cr}, \quad B_z = \frac{k}{2\pi r}\frac{\partial\psi}{\partial r}.$$

Similarly, the following expressions are obtained from the Euler equation for the pressure and plasma density:

$$p = k^2 P(\psi) - \frac{k^2 - 1}{2\pi c^2 r^2}[J^2(C) - J^2(\psi)], \quad (11)$$

$$\rho = \frac{k^2 - 1}{\pi c^2\Omega^2 r^4}[J^2(C) - J^2(\psi)]. \quad (12)$$

We illustrate the latter variant by an example of the toroidal configuration:

$$\psi = \frac{1}{2}\psi_0\left[(bR^2 + r^2)z^2 + \frac{a-1}{4}(r^2 - R^2)^2\right], \quad (13)$$

where R is the radius of the magnetic axis and a, b, and ψ_0 are constants. Expression (13) describes the steady-state plasma, whose pressure and the total current across the circle of radius r is related to the magnetic flux by the following relationship [2]:

$$16\pi^3\frac{dP}{d\psi} = -a\psi_0, \quad \frac{8\pi^2}{c^2}\frac{dJ^2}{d\psi} = -b\psi_0 R^2.$$

In the case of $a > 1$, $b > 0$, and $\psi_0 > 0$, we find for the pressure and total current across the circle of radius r in the immobile plasma

$$p = P(\psi) = \frac{a\psi_0}{16\pi^3}(C - \psi),$$

$$J^2(\psi) = \frac{b\psi_0}{8\pi^2}c^2R^2(C - \psi).$$

According to expressions (11) and (12) obtained above,

the pressure and density of the rotating plasma are defined by the following expressions:

$$p = \frac{\psi_0}{16\pi^3}(C-\psi)\left[ak^2 - b(1-k^2)\frac{R^2}{r^2}\right],$$

$$\rho = \frac{b\psi_0 R^2}{8\pi^3\Omega^2 r^4}(1-k^2)(C-\psi).$$

The pressure and density of rotating plasma have nonnegative values inside the toroidal configuration provided that the conditions

$$1 < \frac{1}{k^2} < 1 + \frac{aR_1^2}{bR^2}$$

are fulfilled. Here, R_1 is the inner radius of the configuration in the plane $z = 0$:

$$R_1^2 = R^2 - \sqrt{\frac{8C}{(a-1)\psi_0}}.$$

The general formulation of the method for constructing the solution to the system of equations (2) and (3) for the axisymmetric configuration whose boundary is defined by the condition $\psi(r, z) = C$ corresponds to a change in all components of the current density in rotating plasma. It follows from formulas (8), (9), (11), and (12) above that, in this case, the plasma magnetic field, pressure, and density can be written out in the form

$$B_r = -\frac{k}{2\pi r}\frac{\partial\psi}{\partial z}, \quad B_\varphi = \frac{2G}{cr}, \quad B_z = \frac{k}{2\pi r}\frac{\partial\psi}{\partial r},$$

$$p = k^2 P(\psi) - \frac{1}{2\pi c^2 r^2}[f(\psi) - f(C)],$$

$$\rho = \frac{1}{\pi c^2\Omega^2 r^4}[f(\psi) - f(C)],$$

where the notation $f = G^2 - k^2J^2$ is used.

Thus, if a solution to the Shafranov equation is known for a certain axisymmetric configuration of immobile plasma, then, with the method described in this paper, we can construct the solution to equations of magnetic hydrodynamics for the same configuration of a uniformly rotating plasma.

In conclusion, we would like to note that for the plasma configuration with an azimuth distribution of the current density, i.e., for the case $J = 0$, the employment of an additional confining uniform magnetic field $\mathbf{B}_{ext} = B_{ext}\mathbf{e}_z$ is an alternative variant of constructing the solution to the system of equations (2) and (3).

In this case, the effect of the centrifugal force is compensated by the interaction of the azimuth current with this field. Then, the expression for the plasma density is written as

$$\rho = -\frac{j_\varphi B_{ext}}{cr\Omega^2}.$$

In other words, the direction of the additional external field depends on the sign of the azimuth component of the current density.

In particular, when using the additional external magnetic field for a rotating plasma ball, a following solution to the system of equations (2) and (3) is obtained:

$$\rho = \frac{15B_0 B_{ext}}{8\pi R^2\Omega^2}, \quad \mathbf{V} = \Omega r\mathbf{e}_\varphi,$$

$$p = \frac{45B_0^2}{32\pi R^2}r^2\left(1 - \frac{r^2+z^2}{R^2}\right),$$

$$B_r = -B_0\frac{3rz}{2R^2}, \quad B_\varphi = 0,$$

$$B_z = B_{ext} + \frac{3}{2}B_0\left(\frac{2r^2+z^2}{R^2} - 1\right).$$

We should note that in this case, in contrast to previous variant (10), the plasma-density distribution is uniform.

REFERENCES

1. V. D. Shafranov, Zh. Éksp. Teor. Fiz. **33**, 710 (1957) [Sov. Phys. JETP **33**, 545 (1958)].
2. L. D. Landau and E. M. Lifshitz, *Course of Theoretical Physics*, Vol. 8: *Electrodynamics of Continuum* (Nauka, Moscow, 1982; Pergamon Press, New York, 1984).
3. L. D. Landau and E. M. Lifshitz, *Course of Theoretical Physics*, Vol. 6: *Fluid Mechanics* (Nauka, Moscow, 1986; Pergamon Press, New York, 1987).

Translated by T. Galkina

Doklady Physics, Vol. 47, No. 12, 2002, pp. 842–845. Translated from Doklady Akademii Nauk, Vol. 387, No. 5, 2002, pp. 613–616.

PHYSICS

Spin-Selective Adsorption of Water Vapor

A. A. Vigasin*, A. A. Volkov, V. I. Tikhonov, and R. V. Shchelushkin**

Presented by Academician F.V. Bunkin June 21, 2002

Received July 1, 2002

The spin-selective adsorption of water vapor on an aluminum-oxide surface was discovered about a decade ago (see, e.g., [1]). As was shown in [2], this effect can be used to separate the spin isomers of water by frontal chromatography. When hydrogen spins in a water molecule are parallel and antiparallel to each other, the molecule is in the ortho and para states, respectively. The ratio of the statistical weights of the ortho and para states is equal to three; therefore, in an equilibrium water vapor under normal conditions, the ratio of ortho-to-para isomer content is equal to three. Since transitions between molecular ortho and para states are forbidden, water vapor is essentially a mixture of independent ortho and para fractions. In this paper, we describe a laboratory experiment in which the equilibrium ortho-to-para ratio 3 : 1 in water vapor was changed by at least a factor of 3 by spin-selective adsorption. This phenomenon is qualitatively explained. It is shown that the change in the ortho-to-para ratio in the real atmosphere can be responsible for marked variations in its radiative characteristics.

In this experiment, the violation of ortho–para equilibrium in water interacting with an adsorbent was determined by continuously monitoring the intensity of spectral ortho and para lines in the rotational spectrum of water molecules. For convenient detection, we took a pair of intense ortho and para lines that were close to each other in the rotational region of the spectrum (Fig. 1). The mixture of water vapor with nitrogen as the carrier gas passed through an adsorption column filled with porous carbon. The gas leaving the column was directed to a cell connected with a submillimeter BWO spectrometer. In the cell, the working mixture was probed at frequencies 30–40 cm^{-1} by a beam of tuned monochromatic radiation. In the piecewise-continuous mode with a rate of 10 points/s, a resolution of 0.0003 cm^{-1}, and a period of 1 min, we recorded the transmittance of the gas layer and observed the ortho–para doublet shown in Fig. 2. As water vapor passed through the adsorbent, a regular and well-reproducible redistribution of the line intensities was observed. Since water-vapor partial pressure in our experiment was lower than 1 Torr, the Doppler broadening was ignored, and only the collisional broadening was taken into account. The lines observed are assumed to have the Lorentz shape with integral intensities S^{ort}, S^{par}, and half-widths γ^{ort}, γ^{par}, respectively. The sum of two Lorentz contours in the real time scale was fitted into the measured line profiles, and thereby the change in the integral intensities of ortho and para lines and, correspondingly, the desired ortho-to-para ratio in water vapor were quantitatively estimated. The resulting ratio $\frac{S^{ort}}{S^{par}} = \frac{N^{ort}}{N^{par}}$ as a function of time is shown in Fig. 3. As is seen, ortho water molecules have higher mobility in the carbon filter. For this reason, the initial and later portions of water vapor diffusing through an adsorbent were enriched in ortho and para molecules, respectively. The ortho- and para-enriched portions of water vapor were extracted from the flow at the corresponding moments of time and frozen in a nitrogen trap. Thus, accumulated samples of spin-modified water with a volume up to 50 ml were stored in a household refrigerator. After a certain time, they were defrosted and subjected to repeated spectral analysis for the ortho/para content. Water that had been in solid and liquid phases and was enriched in ortho or para modifica-

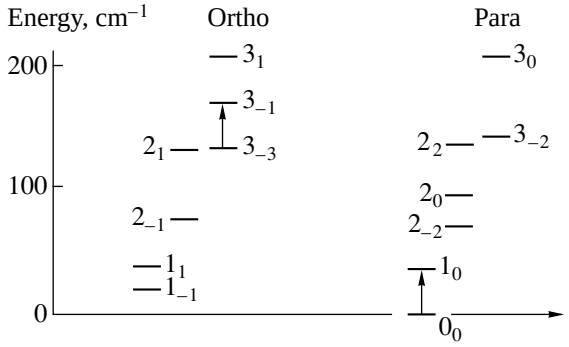

Fig. 1. Lower rotational levels of water. The arrows show the transitions used for monitoring the ortho-to-para ratio.

Institute of General Physics,
Russian Academy of Sciences,
ul. Vavilova 38, Moscow, 119991 Russia

** e-mail: vigasin@kapella.gpi.ru*

*** e-mail: vit1@mailru.com*

1028-3358/02/4712-0842$22.00 © 2002 MAIK "Nauka/Interperiodica"

tions again exhibited an ortho-to-para ratio different from the equilibrium value. The lifetime of the modifications was estimated to be tens of minutes for liquid water and months for ice. We also found that, in addition to carbon, many other developed-surface substances such as zeolite, silica gel, etc., could serve as spin modifiers of water.

The qualitative model of spin-selective adsorption can be represented as follows. Let the total number of water-vapor molecules be N_0 and N_0^{ort} and N_0^{par} molecules be in the ortho and para states, respectively, so that $N_0^{ort} + N_0^{par} = N_0$. Assuming that the spin fractions have different adsorption and desorption rates and do not interconvert in gas phase and on the surface, we can describe the diffusion process with the following set of equations:

$$\begin{aligned} \frac{dN^{ort}}{dt} &= -k_a^{ort} N^{ort} + k_d^{ort}(N_0^{ort} - N^{ort}), \\ \frac{dN^{par}}{dt} &= -k_a^{par} N^{par} + k_d^{par}(N_0^{ort} - N^{par}). \end{aligned} \quad (1)$$

Here, the subscripts a and d refer to adsorption and desorption, respectively. The solution to this set of equations can be represented in the form

$$\begin{aligned} N^{ort,\,par} &= N_0^{ort,\,par}(k_a + k_d)^{-1} \\ &\times [k_d + k_a \exp(-(k_a + k_d)t)], \end{aligned} \quad (2)$$

which must satisfy the initial conditions of thermodynamic equilibrium. Therefore,

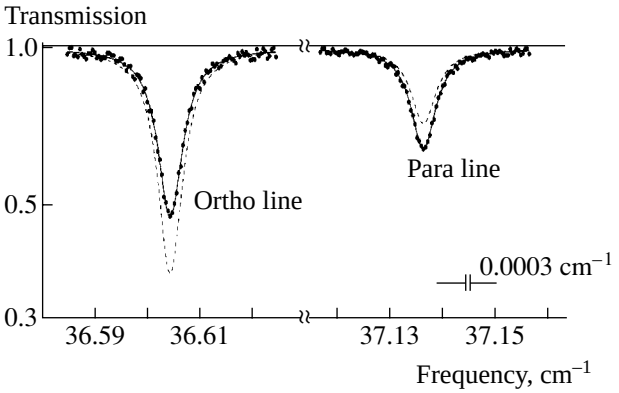

Fig. 2. Typical profiles of measured lines (dashed line) under the equilibrium and after six hours of the experiment.

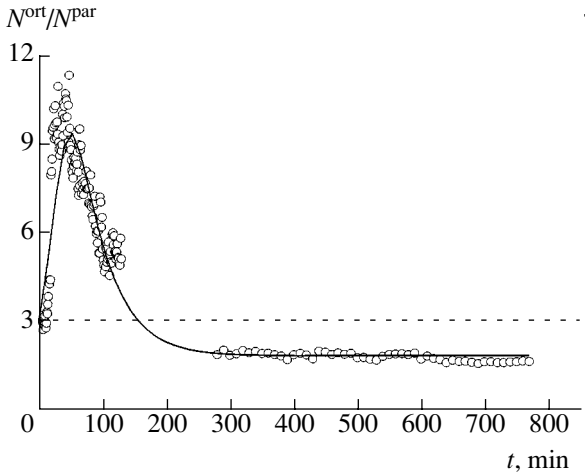

Fig. 3. Time evolution of the ortho-to-para ratio in water vapor after its passage through an adsorbent layer. The solid line is calculated by Eq. (3).

$$\frac{N^{ort}}{N^{par}} = 3\frac{(k_a^{par} + k_d^{par})[k_d^{ort} + k_a^{ort}\exp(-(k_a^{ort} + k_d^{ort})t)]}{(k_a^{ort} + k_d^{par})[k_d^{par} + k_a^{par}\exp(-(k_a^{par} + k_d^{par})t)]}. \quad (3)$$

Using this solution, we can describe the experimental data (Fig. 3) finding the adsorption and desorption rates by the method of least squares. At the initial time, the ratio $\frac{N_0^{ort}}{N_0^{par}} = 3$. The fit of the theory to experimental data gives $k_a^{ort} = 0.9$, $k_d^{ort} = 0.08$, $k_a^{par} = 3.5$, and $k_d^{par} = 0.5$ in relative units. Thus, the kinetic constants for para molecules are 3–6 times higher than the constants for ortho molecules, which is possibly explained as follows. For a rarefied gas, the desorption of molecules from a surface can be considered as a unimolecular process [3]. This means that a molecule desorbs when energy exceeding the separation energy from the surface is concentrated at the breaking bond. The corresponding rate can be represented in the form $k = \frac{\nu W}{Q}$. Here, ν is the activation rate, W is the number of states with energies higher than the dissociation threshold, and Q is the quantum partition function. The basic source of the excess internal energy is the intermolecular vibrational energy independent of the spin state of an adsorbed molecule. Therefore, the number of states W can also be considered as independent of the spin modification. In contrast, the partition function can involve the rotational component if the adsorbed molecule accomplishes hindered or free rotation within the molecule–surface complex. Therefore, the ratio

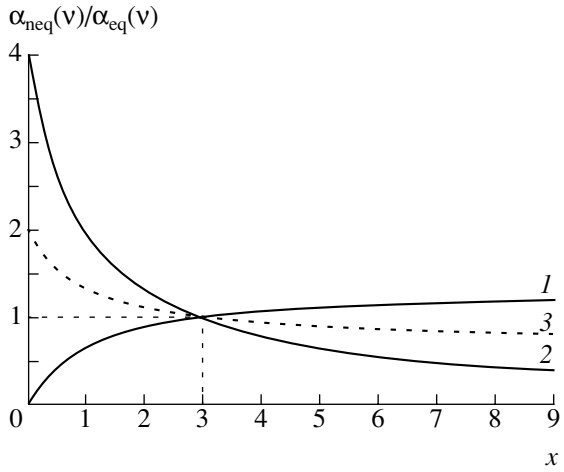

Fig. 4. Acceptable variations in the water-vapor absorption coefficient normalized to the equilibrium value in the case of violating the ortho–para equilibrium $\left(x = \frac{N^{ort}}{N^{par}}\right)$. Curves *1* and *2* correspond to the strong ortho and para lines, respectively. Absorption averaged over the spectral regions involving a large number of ortho and para lines is shown by curve *3*.

between the desorption constants is expected to be $\frac{k_d^{ort}}{k_d^{par}} \approx \frac{1}{3}$.

To characterize the difference in desorption constants, we introduce the equilibrium constant $K_{eq} = \frac{k_a}{k_d} = \frac{Q_{H_2O}Q_{surf}}{Q_{ads}}$, where Q_{H_2O}, Q_{surf}, and Q_{ads} are the partition functions for the water molecule, surface, and molecule–surface complex, respectively. Assuming that $\frac{Q_{H_2O}(ort)}{Q_{H_2O}(par)} = \frac{Q_{ads}(ort)}{Q_{ads}(par)} = 3$, we conclude that $\frac{k_a^{ort}}{k_a^{par}} = \frac{1}{3}$. Taking these ratios for the adsorption and desorption rates, it is easy to approximate the experimental dependence shown in Fig. 3 in the region where the ortho-to-para ratio exceeds the equilibrium value. However, it is impossible to describe the subsequent excess of the para fraction over the ortho fraction. To make this description complete, it is necessary to assume that the ratio $\frac{k_a^{ort}}{k_a^{par}}$ is approximately equal to 0.5–0.7 rather than to $\frac{1}{3} = 0.3(3)$. As is shown in Fig. 3, the qualitative behavior of the kinetics observed for the ortho-to-para ratio is quite accurately reproduced under this assumption. On the basis of the experiment and the model proposed above, it is possible to assume that the nonequilibrium separation of water into the ortho and para isomers occurs spontaneously in various natural processes in living organisms and environment. In particular, it is not improbable that long-term fluctuational violations of the ortho-to-para ratio 3 : 1 occur in the atmosphere.

Water vapor in the atmosphere is always under varying conditions and undergoes condensation and evaporation in air on particles of aerosols and impurities, in clouds, and on the ground. Therefore, the equilibrium ratio between the spin modifications is likely violated in water vapor under certain conditions during kinetic transformations. It is of interest to estimate how this violation can affect the transmission of the atmosphere. If variations in the atmosphere transmission for a violated spin composition turn out to be significant, the simulation of the radiative characteristics of the atmosphere is impossible without comprehensive data on the kinetic prehistory of water vapor in the atmosphere. To estimate this effect, we calculated the model transmission spectrum for a water-vapor layer under atmospheric conditions using the parameters of water-vapor lines from the HITRAN database [4]. The calculations were made for the spectral region near 10 μm, where the Planck radiation curve for the heated ground has its maximum. In addition to the "equilibrium" absorption coefficient α_{eq} corresponding to the radiation transmission through the water-vapor layer with the normal ortho-to-para ratio 3 : 1, we calculated the "nonequilibrium" absorption coefficient α_{neq} corresponding to a violated ortho-to-para ratio. Absorption at individual wavelengths and total absorption over the spectral region turned out to be markedly sensitive to the violation in the ortho-to-para equilibrium. It is easy to show that, depending on the degree of violation in the equilibrium spin composition, the water-vapor absorption coefficient normalized to its equilibrium value is in the range

$$\frac{4}{3}\frac{x}{(x+1)} < \frac{\alpha_{neq}}{\alpha_{eq}} < \frac{4}{x+1},$$

where $x = \frac{N^{ort}}{N^{par}}$ (see Fig. 4). The medium line shown in Fig. 4 by a dashed line characterizes the nonequilibrium absorption coefficient averaged over the region containing a large number of randomly arranged ortho and para absorption lines.

Thus, in this study, we showed that the equilibrium ortho-to-para ratio can be violated in water in contact with an adsorbent. Metastable ortho and para modifications can exist in the form of independent substances for a long time. We assumed that the ortho-to-para ratio

can be violated in natural processes. This spin-equilibrium violation accompanying the condensation of water vapor was shown to be of great importance for the propagation of radiation and for the radiation balance in the atmosphere.

ACKNOWLEDGMENTS

This work was supported in part by the Russian Foundation for Basic Research, project no. 02-05-64529.

REFERENCES

1. V. K. Konyukhov, V. I. Tikhonov, and T. I. Tikhonova, Proc. Gen. Phys. Inst. **12**, 208 (1990).
2. V. I. Tikhonov and A. A. Volkov, Science **296**, 2250 (2002).
3. N. M. Kuznetsov, *Kinetics of Unimolecular Reactions* (Nauka, Moscow, 1982).
4. L. S. Rothman, R. R. Gamache, R. H. Tipping, *et al.*, J. Quant. Spectrosc. Radiat. Transf. **48**, 469 (1992).

Translated by V. Bukhanov

Doklady Physics, Vol. 47, No. 12, 2002, pp. 846–848. Translated from Doklady Akademii Nauk, Vol. 387, No. 5, 2002, pp. 617–619.

PHYSICS

Physical Model of the Low-Temperature-Induced Change in the Structure and Properties of Amorphous Alloys

S. G. Zaĭchenko* and A. M. Glezer**

Presented by Academician O.A. Bannykh July 18, 2002

Received July 29, 2002

All the available experimental data, starting with those published in [1], indicate that the irreversible change in the structure and physical properties after low-temperature treatment (LTT) in liquid nitrogen or helium (low-temperature ΔT effect) is common for amorphous metal alloys (AMAs). Structural studies, including diffraction of thermal neutrons; small-angle scattering of neutrons and X-rays; Mössbauer, magneto-optical, and spectral ellipsometric measurements of both binary and multicomponent AMAs (a) Ni–P, (b) Fe–Co–Si–B, (c) Co–Ni–Fe-Si–B, (d) Fe–Si–B, (e) Fe–Ni–Si–B, and (f) Fe–Cu–Nb–Si–B testify to the irreversible changes in topological and compositional short-range order after low-temperature thermocycling. Low-temperature treatment reduces the yield stress, flow stress, Young modulus, and low- and high-temperature parts of the relaxation spectrum, shifts the optical conductivity spectra, attenuates the equatorial Kerr effect, changes the Curie temperature, and increases the saturation magnetization under a small decrease in the coercive force or considerably decreases the coercive force under a small increase in the saturation magnetization. Experimental data were described and systematized in [2], where it was emphasized that the properties and magnitude of the irreversible changes in the structure and physical properties of AMAs depend primarily on the parameters of LTT (temperature and duration) and the chemical composition of alloys.

The aim of this work was to elaborate a physical model of the low-temperature ΔT effect. The corresponding dynamical problem of thermoelasticity theory has not yet been solved the initial and boundary conditions for cooled AMA samples, which are thin plates with a typical thickness-to-width ratio of ~10^{-3} [3]. For this reason, we will first analyze the solution of the three-dimensional thermal-conductivity equation with the boundary conditions assuming that all the surfaces of the plate at the initial time $\tau = 0$ are cooled instantly to the coolant temperature T_c, which is maintained constant during the entire cooling process. The temperature distribution has the form [4]

$$T(x, y, z, \tau) = (T_c - T_k)\sum_{n=1}^{\infty}\sum_{m=1}^{\infty}\sum_{k=1}^{\infty} A_n A_m A_k \times \cos\frac{\mu_n x}{R_1}\cos\frac{\mu_m y}{R_2}\cos\frac{\mu_k z}{R_3} \times \exp\left[-(\mu_n^2 k_1^2 + \mu_m^2 k_2^2 + \mu_k^2 k_3^2)\frac{\alpha\tau}{R^2}\right] + T_k, \quad (1)$$

where $\frac{\alpha\tau}{R^2}$ is the Fourier number, α is the thermal diffusivity; R_1, R_2, R_3 are the plate length, width, and thickness, respectively; $A_i = (-1)^{i+1}\frac{2}{\mu_i}$, $i = n, m, k$; R is the generalized size determined from $R^{-2} = (R_1)^{-2} + (R_2)^{-2} + (R_3)^{-2}$; $\mu_i = (2i-1)\frac{\pi}{2}$; and $k_i = \frac{R}{R_i}$. Let us analyze the solution by substituting the typical parameters into Eq. (1). It is known that the thermal diffusivity α for an Fe-based AMA is equal to $\alpha \approx 1.3 \times 10^{-5}$ m^2 s^{-1} [5]. Therefore, it follows from Eq. (1) that the time of the complete cooling of the plate with $R_3 = 0.02$ mm for the relative temperature at its center $\theta = \frac{T(0, 0, 0, \tau) - T_k}{T_c - T_k}$ is equal to $\tau_0 = 3.2 \times 10^{-5}$ s with an accuracy of 0.01%. Therefore, the cooling rate for LTT in liquid nitrogen has a high value of $V \sim 10^4$–10^5 K s^{-1}, which is comparable to the cooling rate for amorphous ribbons under quenching from a melt. Thus, since the ribbon AMA samples have small thickness and relatively low thermal diffusivity, the cooling process can be treated as a "thermal shock" and its features can be analyzed by taking only ribbon thickness into account, which

Kurdyumov Institute for Metal Physics and Functional Materials, Bardin Central Research Institute for Ferrous Metallurgy, Vtoraya Baumanskaya ul. 9/23, Moscow, 107005 Russia

** e-mail: zaych@magn.phys.msu.su*

*** e-mail: glezer@imph.msk.ru*

1028-3358/02/4712-0846$22.00

reduces the problem to the one-dimensional case. The numerical solution of the thermal-conductivity equation with similar initial and boundary conditions coincides with the exact solution given by Eq. (1).

As the plate is cooled over the time interval $0 \le \tau \le \tau_0$, thermoelastic stresses appear in the plate. Taking into account the problem geometry ($R_1 \sim R_2 \ge R_3$), these stresses can be determined by solving the one-dimensional problem for the infinitely thin plate. The nonzero thermoelastic-stress tensor components are [3]

$$\sigma_{11} = \sigma_{22} = 2G\alpha_0[T(z,\tau) - T_c]\frac{1+\nu}{1-\nu}, \qquad (2)$$

where the Z axis is perpendicular to the plate surface, σ_{11} and σ_{22} are the components of the stress tensor acting at the unit areas that are perpendicular to each other and parallel to the Z axis, G is the shear modulus, α_0 is the coefficient of thermal expansion, and ν is the Poisson coefficient. Thermoelastic stresses move with the isotherm velocity, and their maximum magnitude $\sigma_{11} = \sigma_{22} \approx 10^7$–$10^8$ N m^{-2} is sufficient, as was shown in [2], to initiate irreversible change in the short-range order, which reduces density fluctuations in the AMA to their disappearance.

The thermal shock changes only the plate volume. Since the plate is thin, the problem of its oscillations reduces to the two-dimensional case. In addition, the plate can undergo only longitudinal oscillations, because the temperature field is symmetric about the neutral planes and, consequently, bending moments are identically equal to zero in any of its sections. It is physically clear that the plate cannot be cooled infinitely long, as follows from solution (1) of the thermal conductivity equation. Therefore, the characteristic cooling time (duration of the thermal shock) is taken to be equal to $\tau_0 = 3.2 \times 10^{-5}$ s. At the time τ_0, the deformation rates of the end surfaces are equal to $\frac{\partial \varepsilon_0}{\partial t} = \frac{\alpha_0 \Delta T}{\tau_0}$.

As is customary in thermoelasticity theory, the averaging is performed over the duration of the thermal shock [6]. The equation of plate longitudinal oscillations has the form [7]

$$\Delta D = \frac{\rho(1-\nu^2)}{E}\frac{\partial^2 D}{\partial t^2}, \qquad (3)$$

where Δ is the Laplace operator, $\alpha_1 = \left[\frac{E}{\rho(1-\nu^2)}\right]^{1/2}$ is the speed of sound in the AMA, ρ is the density, and E is the Young modulus. Solving Eq. (3) with the initial and boundary conditions and normalizing the eigenfunctions, we finally obtain

$$D = \sum_{n=1}^{\infty}\sum_{m=1}^{\infty} B_{n,m}\sin(\lambda_{1,n,m}^{1/2}\alpha_1 t)V_{n,m}(x,y), \qquad (4)$$

where

$$B_{n,m} = 32(\alpha_1\lambda^{1/2})^{-1}\frac{R_1R_2\alpha_0\Delta T}{nm\tau_0},$$

$$\lambda_{1,n,m} = \left(\frac{2\pi n}{R_1}\right)^2 + \left(\frac{2\pi m}{R_2}\right)^2,$$

and

$$V_{n,m}(x,y) = (R_1R_2)^{1/2}\sin\frac{\pi n x}{2R_1}\sin\frac{\pi m y}{2R_2}.$$

Shear oscillations in the plate are absent, because its shape does not change in the process of cooling, and, consequently, the elementary-volume rotation $2\Omega = \frac{\partial u_2}{\partial x} - \frac{\partial u_1}{\partial y}$ is identically equal to zero. The above discussion indicates that thermoelastic stresses initiate the process of changing the initial short-range order, and longitudinal oscillations giving rise to the drift of the mainly metalloid atoms make this process irreversible. The drift of atoms can proceed via, e.g., the mechanism proposed by Eiring [8]. Another possible mechanism of relaxation of internal stresses rearranges atoms. The irreversible displacement of one or several atoms under the action of either thermoelastic stresses or longitudinal oscillations of the plate can induce the avalanche displacement of the group of neighboring atoms, if it is accompanied by the reduction of their potential energy. Such a process was realized in computational models of amorphous clusters [9]. Thus, low-temperature thermal cycling induces homogenization of the AMA structure, which is accompanied by the lowering of the internal stress fields in the amorphous matrix.

In order to evaluate the physical model developed for the low-temperature ΔT effect, we carried out an experiment aimed to test the following main statements: (i) atomic drift responsible for the irreversible changes in the short-range order is caused by the longitudinal oscillations of the ribbon AMA samples and (ii) thermoelastic stresses induce the process of changing the initial short-range order.

The first statement is proved by analyzing the solution of Eq. (3) with various boundary conditions. It follows from Eq. (3) that longitudinal oscillations do not appear in samples with the ends fixed along the contour. The joint LTT of Fe–Co–Si–B and Fe–Ni–Si–B amorphous alloy samples of systems with free and fixed ends in liquid nitrogen demonstrated that both structural characteristics and physical (magnetic, magneto-optical, and ellipsometric) properties do not change in samples with fixed ends [10]. The second statement could be proved most conclusively by using an AMA ribbon with zero internal stresses ($\sigma_{int} = 0$). For this purpose, the Fe–Cu–Nb–Si–B AMA ribbon samples of 10-yr age, in which $\sigma_{int} \approx 0$ according to our studies, were subjected to a two-stage treatment: annealing with a

Magnetic characteristics of the Fe–Cu–Nb–Si–B amorphous metallic alloy in the initial state and after low-temperature treatment (LTT) with preliminary 2-h annealing

Initial state		Preliminary annealing (T = 493 K) with the subsequent LTT (T = 77 K)		
coercive force, A cm^{-1}	saturation induction, T	LTT duration, h	coercive force, A cm^{-1}	saturation induction, T
0.1121	1.183	2	0.1066	1.192
0.1243	1.180	3	0.1109	1.183
0.0914	1.177	4	0.0930	1.187
0.1012	1.181	5	0.0992	1.189

subsequent LTT in liquid nitrogen. The results of investigations and the treatment parameters are listed in the table. It follows from the table that the magnetic characteristics after such a treatment do not change, because a part of the LTT-induced thermoelastic stresses compensated stress σ_{int} caused by heating. The remaining part of thermoelastic stresses was insufficient to initiate structural changes in the amorphous matrix.

ACKNOWLEDGMENTS

This work was supported by the Russian Foundation for Basic Research, project no. 00-02-16312.

REFERENCES

1. S. G. Zaĭchenko, A. M. Glezer, E. A. Gan'shina, *et al.*, Dokl. Akad. Nauk **367**, 478 (1999) [Dokl. Phys. **44**, 545 (1999)].
2. A. M. Glezer, S. G. Zaĭchenko, N. S. Perov, and E. A. Gan'shina, Izv. Akad. Nauk, Ser. Fiz. **65** (10), 1472 (2001).
3. V. Novatskiĭ, *Problems of Thermoelasticity* (Akad. Nauk SSSR, Moscow, 1967).
4. A. V. Lykov, *Theory of Heat Transfer* (Vyssh. Shkola, Moscow, 1967).
5. I. V. Zolotukhin, *Physical Characteristics of Amorphous Metallic Materials* (Metallurgiya, Moscow, 1986).
6. N. Tong Kin, *Theory of Mechanical Vibrations* (GNTIML, Moscow, 1963).
7. A. Lyav, *Mathematical Theory of Elasticity* (ONTI NKTP SSSR, Moscow, 1935).
8. H. Eiring, Chem. Phys. **4** (4), 283 (1936).
9. D. Srolovitz, V. Vitek, and T. Egami, Acta Metal **31** (2), 335 (1983).
10. S. G. Zaĭchenko, A. A. Radkovkaya, E. A. Gan'shina, and F. N. Sivov, in *Proceedings of the International Conference on Magnetic Materials, 21–24 September, Irkutsk, 2001*, p. 55.
11. S. Zaĭchenko, S. Roth, and A. Glezer, in *Book of Abstracts of XV Conference on Soft Magnetic Materials, 5–7 September, Bilbao, 2001*, p. E-36.

Translated by T. Galkina

Doklady Physics, Vol. 47, No. 12, 2002, pp. 849–851. Translated from Doklady Akademii Nauk, Vol. 387, No. 6, 2002, pp. 757–759.

PHYSICS

Photoconductivity Spectrum of C_{60} Single Crystals Placed in a Magnetic Field

Yu. I. Golovin*, D. V. Lopatin*, R. K. Nikolaev, A. V. Umrikhin*, and S. Z. Shmurak****

Presented by Academician Yu.A. Ossipyan July 29, 2002

Received July 29, 2002

To explain mechanisms of generation of free charge carriers in C_{60} single crystals under the action of light or a penetrating radiation, we need to analyze both intramolecular and intermolecular electronic processes [1]. Theoretical calculations of the electronic structure [2, 3] were recently compared with experimentally observed optical transitions in molecular and solid (films and microcrystals) states of C_{60} [1, 4, 5]. This comparison testifies to the fact that the existence of a crystal field changes the energy of intermolecular excited states and forms a complicated electronic fine structure. In addition to the internal mechanisms, an external constant magnetic field can also noticeably affect the process of the photogeneration of charge carriers in C_{60} single crystals [6, 7]. The main goal of the present study is to clarify the role of intermolecular electronic processes in the photogeneration of charge carriers in fullerite single crystals and the possibility to affect these processes by a weak magnetic field ($B < 1$ T).

In this study, comparative investigations of the photoconductivity excitation spectra (within the photon energy range from 2 to 5 eV) for C_{60} single crystals in both the absence and presence of a magnetic field ($B =$ 0.4 T) at room temperature are made. Qualitative differences in the photoconductivity spectra of fullerite single crystals and films are determined in the absence of a magnetic field. An increase in the photoconductivity of C_{60} single crystals in a magnetic field within the photon energy range 2.4–4.5 eV is discovered. Local photoconductivity peaks in the presence of a magnetic field are shown to correspond to charge-transfer exciton states.

In this study, we dealt with high-purity (99.95%) C_{60} single-crystal samples grown by vapor transport (sublimation). In order to excite the photoconductivity, we used the light of a DKSSh-200 xenon lamp that has a virtually continuous emission spectrum in the visible and ultraviolet spectral regions. In order to measure the photoconductivity spectral curve, light from the lamp was transmitted through a high-aperture monochromator. The electric current I flowing through indium contacts that were fixed on one of the faces of a sample with a silver paste served as a measure of the photoconductivity. A constant voltage of 10–30 V was applied to the contacts. To prevent light-induced oxidation, the sample was placed into a sealed ampoule. A constant magnetic field with the induction of 0.4 T was obtained by means of an electromagnet.

The photoconductivity excitation spectra of C_{60} single crystals in the presence and absence of the magnetic field are shown in the figure. Decomposing the spectra into Lorentz components allowed us to select three optical transitions with energies of 2.64, 3.07, and 3.87 eV.

In the absence of a magnetic field, the photoconductivity excitation spectra of C_{60} single crystals had, in the first approximation, the same basic spectral features as thin fullerite films. Similarly to [1], the active generation of photocarriers occurred at photon energies $E >$ 2.35 eV. Following [8], the photoconductivity spectrum can be decomposed into three components. It was shown in spectral studies of C_{60} films [1] that a peak near 2.7 eV is the result of mixing of two types of exciton states with the charge transfer, which mix with forbidden intramolecular excited states. In [3, 4], it was found that the energy of 2.64 eV corresponds to the $h_u \longrightarrow t_{1g}$ allowed dipole optical transition.

The second optical transition, with the energy of 3.07 eV, is usually related to the charge-transfer excitons, since this energy corresponds to none of the transitions in C_{60} and is higher than the energy of the lowest Frenkel exciton [8].

At the same time, there exist qualitative differences between spectral features of the photoconductivity for fullerite single crystals and films. For example, the 3.5-eV peak observed for thin films and corresponding to the $h_g \longrightarrow t_{1u}$ allowed dipole optical transition [4] is shifted towards higher energies in the photoconductiv-

* *Tambov State University, ul. Internatsional'naya 33, Tambov, 392622 Russia*

** *Institute of Solid-State Physics, Russian Academy of Sciences, Chernogolovka, Moscow oblast, 132432 Russia*
e-mail: lopatin@tsu.tmb.ru

1028-3358/02/4712-0849$22.00 © 2002 MAIK "Nauka/Interperiodica"

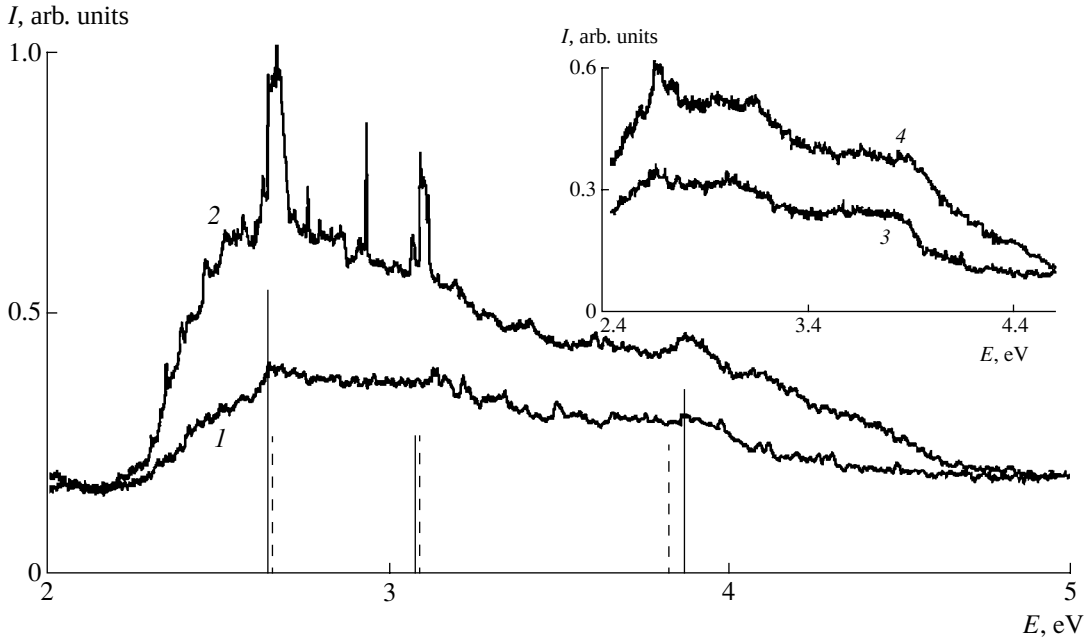

Photoconductivity spectra in the absence (curves *1* and *3*) and in the presence (curves *2* and *4*) of the magnetic field with the induction $B = 0.4$ T. Vertical solid and dashed lines indicate the positions of optical transitions in the presence of the magnetic field and in its absence, respectively. Photoconductivity spectra of a sample after 10-min photoexposure are shown in the insert.

ity excitation spectra of C_{60} single crystals. In our experiments, the shift of the optical transition in the energy scale can be explained by the complicated internal structure of molecular zones, which is caused by various disturbances in actual crystals. Owing to these disturbances, the $h_u(h_g)$ occupied five-fold degenerate levels and the $t_u(t_g)$ occupied three-fold free levels split [9].

Investigation of the photoconductivity spectra in the magnetic field with the induction $B = 0.4$ T yielded the following results. An increase in the photoconductivity of 5 to 15% was observed in the 0.4-T magnetic field within the photon energy range 2.5–4.5 eV. In addition, the photoconductivity spectra of C_{60} single crystals placed into a magnetic field have a characteristic difference from those at $B = 0$. In the presence of the magnetic field, the band corresponding to $E = 2.64$ eV is enhanced, and new maxima arise. The local photoconductivity peaks at the energy $E = 2.95$ and 3.13 eV are the most intense. The intensity of the local photoconductivity peaks rapidly decreases in a magnetic field with the oxidation of a sample (see insert in Fig. 1). This is caused by the fact that deep traps for charge carriers appear when fullerites interact with oxygen. Thereby, defects that promote the exciton dissociation are neutralized. Eventually, this results in a decrease in the charge-carrier number and quenching of the photoconductivity [10]. Decomposition into the Lorentz components showed that the energy of the optical transitions had not changed in the magnetic field but that the oscillator strength for the $h_u \longrightarrow t_{1g}$ transitions had increased (see figure).

Since features of the fullerite optical spectra are formed by the intramolecular and intermolecular interactions [1], we assume while discussing the mechanism of the effect of a magnetic field on the photoconductivity that the field affects the exciton states. This conclusion is also implied by the fact that the local photoconductivity peaks lie within the zone of the charge-transfer excitons. The effect of the magnetic field on the mechanism of charge-carrier generation can be represented in the form of the following scheme. The light absorption leads to the formation of an exciton. The scattering on the surface, on the lattice oscillations, and on the impurities, as well as on defects, results in the dissociation of the excitons and formation of free carriers. In [7], results were obtained that enable us to make definite statements on the influence of spin states of electron–hole pairs on transport processes in C_{60} single crystals. The role of the magnetic field can be reduced to only the variation of the spin state of an electron and a hole in the excitons. This results in an increased probability of the electron–hole pair dissociating into free charge carriers or in a reduced probability of their subsequent recombination and, as a consequence, in an enhancement of the photoconductivity in the presence of a magnetic field. Thus, the magnetic field is capable of governing intermolecular electronic processes of the photogeneration of charge carriers in C_{60} single crystals.

ACKNOWLEDGMENTS

This work was supported by the Program “Fullerenes and Atomic Clusters,” project

no. 40.012.1.1.11.47; by the Russian Foundation for Basic Research, project no. 02-02-17571; and by the Ministry of Education of the Russian Federation, project no. E 00-3.4-552.

REFERENCES

1. S. Kazaoui, N. Minami, Y. Tanabe, *et al.*, Phys. Rev. B **58**, 7689 (1998).
2. W. E. Pickett, Solid State Phys. **48**, 225 (1994).
3. S. S. Moliver and Yu. F. Biryulin, Fiz. Tverd. Tela (St. Petersburg) **43**, 944 (2001) [Phys. Solid State **43**, 982 (2001)].
4. J. Hora, P. Panek, K. Navratil, *et al.*, Phys. Rev. B **54**, 5106 (1996).
5. S. Mochizuki, M. Sasaki, and R. Ruppin, J. Phys.: Condens. Matter **10**, 2347 (1995).
6. Yu. A. Ossipyan, Yu. I. Golovin, D. V. Lopatin, *et al.*, Fiz. Tverd. Tela (St. Petersburg) **41**, 2097 (1999) [Phys. Solid State **41**, 1926 (1999)].
7. Yu. A. Ossipyan, Yu. I. Golovin, D. V. Lopatin, *et al.*, Phys. Status Solidi B **223**, R14 (2001).
8. T. L. Makarova and I. B. Zakharova, Fiz. Tverd. Tela (St. Petersburg) **44**, 478 (2002) [Phys. Solid State **44**, 500 (2002)].
9. N. Troullier and J. L. Martins, Phys. Rev. B **46**, 1754 (1992).
10. C. H. Lee, J. Yu, B. Kraabel, *et al.*, Phys. Rev. B **49**, 10572 (1994).

Translated by G. Merzon

Doklady Physics, Vol. 47, No. 12, 2002, pp. 852–855. Translated from Doklady Akademii Nauk, Vol. 387, No. 4, 2002, pp. 471–474.

TECHNICAL PHYSICS

Structural Mechanisms of Fracture in Amorphous Metallic Alloys

V. A. Pozdnyakov and A. M. Glezer*

Presented by Academician O.A. Bannykh July 18, 2002

Received July 19, 2002

Under the same external conditions, the fracture of an amorphous metallic alloy can be either brittle or ductile depending on its structural state, which is determined by the conditions of amorphization and structural relaxation [1–3]. Brittle fracture occurs as spalling in the planes corresponding to the maximum tensile stress and is not accompanied by any macroscopic flow below the yield point. The ductile fracture of amorphous metallic alloys occurs along the planes corresponding to the maximum shear stress after or simultaneously with plastic flow [1–3]. The fractographic pattern of the fracture surface usually involves both a nearly smooth zone caused by shear along a band before the formation of a crack and a zone of vein-shaped (brook-shaped) tracery. "Veins" are projections produced at both surfaces due to the formation of a local neck in the course of ductile fracture. Their thickness is about 0.1 μm [1–3]. The morphology of the fracture surface stems from the meniscus instability accompanying the development of viscous discontinuity in a layer of a viscous material. It is a special case of the Taylor instability.

However, the fracture surface in the samples of amorphous metallic alloys sometimes has a cup-shaped structure; i.e., a cellular pattern is observed. Such a pattern results from fracture caused by the nucleation, growth, and coalescence of pores. For instance, the entire fracture surface of the FeBSiCo alloy that is partially embrittled by thermal treatment had a cup-shaped relief [4]. Veins in the FeBSb(Ce) amorphous metallic alloy have a rather complicated structure: they consist of chains formed by small pores and are separated by chains of rather large pores [1]. The fracture pattern in the $Fe_{82}B_{18}$ alloy is a combination of spalling regions and domains of ductile fracture [1].

Kurdyumov Institute for Metal Physics and Functional Materials, Bardin Central Research Institute for Ferrous Metallurgy, Vtoraya Baumanskaya ul. 9/23, Moscow, 107005 Russia

** e-mail: glezer@imph.msk.ru*

Many details of the fracture of amorphous metallic alloys still remain unclear, including the structural mechanisms of their fracture and the conditions of the implementation of these mechanisms. The aim of this work is to analyze the structural mechanisms and conditions of the fracture of amorphous metallic alloys along shear bands and to classify the mechanisms of the brittle, quasi-brittle, and ductile fracture of these materials.

BRITTLE AND QUASI-BRITTLE FRACTURE

Brittle and quasi-brittle fracture is initiated by technological or structural defects. In brittle materials, where the stress σ_f of the nucleation and development of cracks is lower than the yield point σ_y and local stress concentration cannot decrease owing to the plastic flow, fracture stress is determined by the most dangerous structural defects, i.e., those resulting in the maximum stress concentration.

When $\sigma_f \simeq \sigma_y$, a plastic zone is formed near the crack tip and has the form of a shear band or an array of such bands. If the transverse size of the plastic zone is much smaller than its length, it is the quasi-brittle fracture of amorphous metallic alloys. The size of the thin plastic zone arising near the tip of a crack under the plane stress conditions and the displacement accompanying crack opening can be well described quantitatively as functions of the crack length δ in the framework of the Dugdale or Bilby–Cottrell–Swinden models [5, 6]. In these models, the material is assumed to be ideally elastoplastic, which is the case for amorphous metallic alloys. Assuming that fracture occurs when the displacement at the crack tip reaches the critical value, i.e., $\delta = \delta_c$, we obtain the fracture stress in the form

$$\sigma_f = 2\frac{\sigma_y}{\pi}\arccos\left\{\exp\left[-\frac{\pi E\delta_c}{8\sigma_y a}\right]\right\}. \qquad (1)$$

The fracture of an amorphous metallic alloy takes place when the plastic-zone size, crack opening width, and stress intensity factor reach certain critical values.

1028-3358/02/4712-0852$22.00

THE CONDITION FOR THE FORMATION OF SHEAR BANDS

The threshold flow stress τ_m in amorphous metallic alloys decreases with increasing excess free volume in the deformation process and reaches a certain steady-state value τ_0 [1–3]. This loss of the material strength (decrease in viscosity) causes the localization of plastic flow, i.e., the formation and propagation of shear bands. Ignoring the dependence of local flow stress on the strain rate, one can represent the local stress–strain curve of an amorphous metallic alloy in the simplified form

$$\begin{aligned} \tau(\gamma) &= \mu\gamma, \quad \gamma \le \frac{\tau_m}{\mu}, \\ \tau(y) &= \tau_0, \quad \gamma > \frac{\tau_m}{\mu}. \end{aligned} \tag{2}$$

In the framework of this approach, the stress τ_m of the initiation of heterogeneous plastic flow and steady-state stress τ_0 are the main microscopic parameters characterizing the plastic behavior of an amorphous metallic alloy.

The stress field in the tip of the shear band is similar to the stress field from a shear crack including stress τ_0 corresponding to the resistance to shear in the band. Using this analogy, we can introduce stress intensity factor K_b for the band. Under uniform applied shear stress τ, the stress intensity factor for the shear band of width L has the form

$$K_b = \beta(\tau - \tau_0)\left(\frac{L}{2}\right)^{1/2}, \tag{3}$$

where β is a numerical factor of about unity. When the stress intensity factor reaches a certain critical value determined by the mechanisms of energy dissipation accompanying the propagation of the shear band, this propagation becomes unstable. The energy dissipation per unit length of the propagation of the shear band can be represented as $G_b^* = (\tau_m - \tau_0)u_e$; here, u_e is the mean displacement at the end domain of the shear band, where shear stress decreases from τ_m to τ_0.

The criterion for the propagation of the band takes the form

$$K_b \ge K_{b1}^* = \left[\frac{2\mu(\tau_m - \tau_0)u_e}{1-\nu}\right]^{1/2}, \tag{4}$$

which is the Griffiths-type energy-balance equation determining the critical size of the shear band with respect to the applied stress.

Various structural inhomogeneities of different scales in amorphous metallic alloys modify the condition for the development of shear bands and can induce internal stresses [7] and impede the propagation of the bands. The macroscopic condition for the development of bands in amorphous metallic alloys, i.e., the condition under which the shear band overcomes obstacles caused by meso- and macroscopic structural inhomogeneities, is represented in the form

$$K_b \ge K_{b2}^*, \tag{5}$$

where the second critical value K_{b2}^* of the stress intensity factor is determined by the nature, scale, and concentration of structural inhomogeneities in the amorphous metallic alloy and $K_{b2}^* < K_{b1}^*$.

DUCTILE FRACTURE ALONG SHEAR BANDS

At $\sigma_f > \sigma_y$, the fracture of amorphous metallic alloys is ductile; i.e, the nucleation of a microcrack is preceded by the formation of a shear band [1–3]. Steps arising at the free surface of a sample due to the development of shear bands are stress concentrators, whose sizes reach the critical value corresponding to the nucleation of a crack and its subsequent opening along the shear band. The crack is formed along the shear band, when the stress intensity factor K of the viscous crack exceeds the critical value K_c.

The rheological behavior of the material within the shear band is unknown. For this reason, the shear stress dependence of the shear strain rate is approximated by the power function

$$\tau = \eta_n(\dot\gamma)^n = \tau_0\left(\frac{\dot\gamma}{\dot\gamma_0}\right)^n, \tag{6}$$

where η_n and n are the parameter and exponent of nonlinear viscosity, respectively, and material parameters τ_0 and $\dot\gamma_0$ have dimensions of stress and inverse time, respectively. In [8, 9], the conditions and features of the formation and development of the meniscus instability were analyzed for the fracture of amorphous metallic alloys along shear bands. However, the fracture mechanism associated with the nucleation and growth of pores can be energetically and kinetically more favorable than the meniscus instability.

Let us discuss the conditions for the fracture of amorphous metallic alloys along shear bands due to the development of the system of pores. The kinetics of pore nucleation in a deformed material were repeatedly analyzed earlier [10]. The rate of the heterogeneous nucleation of pores at structural inhomogeneities in the shear band of amorphous metallic alloys under normal stress σ_n is

$$J = C_0 Z R \exp\left(-\frac{G^*}{kT}\right), \tag{7}$$

where C_0 is the concentration of the potential sites for pore nucleation, $Z = \frac{\sigma_n^2\Omega}{4}(3\pi F\Gamma^3 kT)^{-1/2}$ is the Zel'dovich factor, $R = \frac{2kT}{a\Omega\eta}$, Ω is the atomic volume, $G^* =$

$\frac{4F\Gamma^3}{\sigma_n^2}$ is the nucleation energy for a pore of the critical size at a structural inhomogeneity, F is the pore shape factor, and Γ is the fracture energy.

In the kinetic calculations of the growth of pores in the shear band, where the stress dependence of the material strain rate is described by Eq. (6), the stress distribution in the ensemble of growing pores confined within the shear band is preliminary calculated [11]. The rate of increase of the volume fraction of pores in the shear band is written as

$$\dot{f} = \frac{h_0^{(1+n)/n}\dot{\gamma}_0}{(1-f)^{(3+n)/n}L^{(1+n)/n}\psi^{1/n}\tau_0^{1/n}} \times\left[\sigma - \frac{2\Gamma}{h_0}(1-f)^2\right]^{1/n}, \quad (8)$$

where $\psi = \frac{2^{1+n}(1+2n)^n}{(2+n)n^n}$, L is the mean distance between the pore centers in the plane of the shear band, and h_0 is the initial thickness of the shear band at the beginning of the development of the pore system.

It is assumed that fracture occurs when the volume fraction f of pores in the shear band reaches the critical value f^*. Then, the time until fracture as a function of the applied stress and material viscosity in the band has the form

$$t_p = \psi^{1/n}\left(\frac{\tau_0}{\dot{\gamma}_0}\right)\tau_0^{(1-n)/n}\left(\frac{L}{n}\right)^{(1+n)/n} \times\int_{f_0}^{f^*}\frac{(1-f)^{(3+n)/n}df}{\sigma^{1/n}\left[1-\frac{2\Gamma}{h_0\sigma}(1-f)^2\right]^{1/n}} \quad (9)$$

and is proportional to material viscosity in the shear band.

The fracture mechanism in an amorphous metallic alloy changes from the finger-shaped development of a viscous crack to the nucleation, growth, and coalescence of pores, when the characteristic time t_3 of pore nucleation in the volume $v_b = \Delta x h$ of unit width and length Δx in the shear band is much smaller than the characteristic time t_{crack} of passing distance Δx by the viscous crack. This kinetic criterion has the form

$$J \gg \frac{V}{h(\Delta x)^2}. \quad (10)$$

The velocity $v(\sigma, n)$ of the meniscus-instability-induced propagation of the viscous crack in the shear band was calculated in [9] for different n values. The mean distance between the sites of the heterogeneous nucleation of pores can be used as the characteristic size Δx in Eq. (10).

It is well known that structural relaxation in amorphous metallic alloys embrittles a material [1–3]. This embrittlement is caused by the decrease in the excess free volume, pore nucleation, and segregation of metalloids at the free and pore surfaces. The more relaxed the state of an amorphous metallic alloy, the higher the concentration of the potential nucleation sites for microscopic discontinuities, $C_0 \sim (\Delta x)^{-3}$, and, therefore, the higher the nucleation rate J and material viscosity; i.e., the V value for fixed σ is lower.

The above analysis leads to the following conclusions concerning the mechanisms and conditions of fracture along shear bands in an amorphous metallic alloy. When $K_{b2}^* > K_b > K_{b1}^*$ and $K > K_c$, a crack develops along the shear band inhibited by structural inhomogeneities. This process can be accompanied by the brittle fracture of large structural inhomogeneities in the amorphous metallic alloy, which impede band development. As a result, mixed ductile–brittle fracture occurs along shear bands. When $K_b > K_{b2}^*$ and $K > K_c$, ductile fracture occurs along shear bands. When criterion (10) is met, this ductile fraction is due to the mechanism of the nucleation, growth, and coalescence of pores. When the opposite criterion is satisfied, the fracture is attributed to the meniscus instability. When the conditions for both these mechanisms are close to each other, the mixed mechanism of the development of the ductile crack is realized.

In conclusion, we can list the following main fracture mechanisms in amorphous metallic alloys.

(i) Brittle fracture, where the crack plane is perpendicular to the tension axis.

(ii) Quasi-brittle fracture, i.e., the combined development of a crack and a shear band and the formation of an array of secondary bands near the crack tip.

(iii) Mixed brittle–ductile fracture along shear bands, i.e., either the formation of pores in the shear band, which are united by brittle cracks, or the development of the main viscous crack due to the formation of brittle cracks–satellites.

(iv) Ductile fracture along shear bands due to the nucleation, growth, and coalescence of pores.

(v) Ductile fracture along shear bands due either to the meniscus instability of the viscous crack front or to the mixed mechanism of the nucleation and growth of pores combined with the meniscus instability.

(vi) Ductile fracture accompanying homogeneous flow in amorphous metallic alloys due to the development of the pore system in the entire sample.

REFERENCES

1. A. M. Glezer and B. V. Molotilov, *Structure and Mechanical Characteristics of Amorphous Alloys* (Metallurgiya, Moscow, 1992).

2. V. P. Alekhin and V. A. Khonik, *Structure and Physical Mechanisms of Deformation of Amorphous Alloys* (Metallurgiya, Moscow, 1992).
3. *Amorphous Metal Alloys*, Ed. by F. E. Lyubarskiĭ (Metallurgiya, Moscow, 1987).
4. T. W. Wu and F. Spaepen, Embrittlement of a Metallic Glass, in *Mechanical Behavior of Rapidly Solidified Materials*, Ed. by S. M. L. Sastry and B. A. MacDonald (Metal. Soc. of AIME, New York, 1985), pp. 293–305.
5. D. Broek, *Elementary Engineering Fracture Mechanics* (Noordhoff, Groningen, 1974; Vysshaya Shkola, Moscow, 1980).
6. G. F. Nott, *Elementary Fracture Mechanics* (Metallurgiya, Moscow, 1978).
7. V. A. Pozdnyakov, Izv. Akad. Nauk, Ser. Fiz. **65** (10), 1412 (2001).
8. F. Spaepen, Acta Metal **23** (3), 615 (1975).
9. A. S. Argon and M. Salama, Mater. Sci. Eng. **23**, 219 (1976).
10. H. Trinkaus and M. H. Yoo, Philos. Mag. A **57** (4), 543 (1988).
11. V. A. Pozdnyakv, V. V. Fedorov, and V. T. Borisov, *Physics and Chemistry of Amorphous (Glass) Metallic Alloys* (Inst. Metallurgii im. A.A. Baĭkova, Akad. Nauk SSSR, Moscow, 1989), p. 7.

Translated by K. Kugel

Doklady Physics, Vol. 47, No. 12, 2002, pp. 856–858. Translated from Doklady Akademii Nauk, Vol. 387, No. 4, 2002, pp. 475–477.

TECHNICAL PHYSICS

Shock-Wave Egress from a Nozzle into a Bounded Space

Academician V. E. Fortov*, Corresponding Member of the RAS Yu. S. Solomonov, V. V. Golub*, T. V. Bazhenova*, T. A. Bormotova*, V. V. Volodin*, V. P. Efremov*, A. A. Makeich*, and S. B. Shcherbak***

Received August 2, 2002

Studies of high-speed unsteady supersonic flows are of great importance from the standpoint of the development of modern aviation and rocket engineering. Unsteady effects become especially significant in the case of controlling and correcting rocket engines, whose operating times are comparable to those required for attainment of the steady-state regime. The same problem is urgent for telescopic nozzles and engines with strong thrust control in the takeoff paths of a rocket and at the moment of its launch. In these regimes, unsteady effects are crucial; therefore, disregarding them may cause an emergency situation. The structure of corresponding flows cannot be described analytically. Therefore, it must be studied by experimental and numerical methods.

Unsteady effects must be taken into account when developing efficient methods for high-altitude captive tests of rocket engines. To decrease loads on the nozzle at the moment of initiating engines and to provide an initial rarefaction in the gas path of the test bed, ejectors are used [1]. However, when testing promising engines with shorter settling times, it is difficult to ensure the integrity of the nozzle.

On starting a rocket-engine nozzle, a starting shock wave accompanied by an unsteady supersonic flow propagates in the nozzle [2, 3]. Entering into the ejector, the shock wave interacts with an inducing jet. Perturbations caused by the shock–jet interaction can move upstream along the boundary layer formed by the flow behind the shock and can reach the region near the nozzle, which may result in nozzle failure. This effect is a specific danger for nozzles subjected to high-altitude captive tests.

The effect of the starting shock wave can be another possible cause for an increase in the pressure on the exterior wall of the nozzle.

Tentative experiments have shown that when a shock wave escapes from a channel into semi-infinite space, the diffracted shock wave propagates outside the channel in the opposite direction along the channel generatrix (Fig. 1) [4]. When the diffracted shock wave reaches the rear wall, the pressure on the wall rises by a factor of 1.5. Such an effect was registered by pressure transducers in the experiment described in [4]. When a shock wave escapes from a nozzle into a bounded volume in conditions of high-altitude captive tests or in flight conditions, an increase in the pressure on the noz-

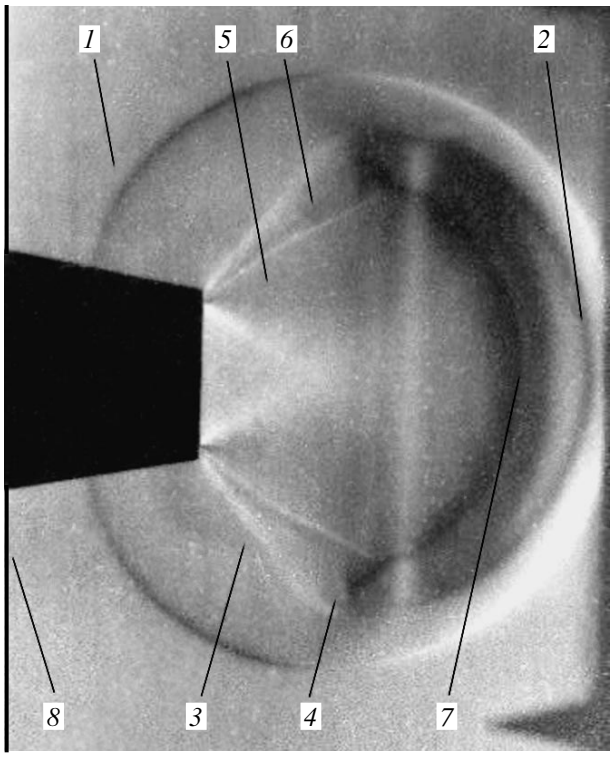

Fig. 1. Shadow photograph of the shock-wave egress from a cylindrical channel: (*1*) diffracted shock wave; (*2*) surface separating the outward gas flow and environmental gas; (*3*) line of flow separation, which convolutes into a vortex (*4*); (*5*) fan of rarefaction waves, which is closed by the oblique shock (*6*); (*7*) stagnation shock wave separating the expanded gas escaping from the nozzle and the denser gas behind the diffracted shock wave; and (*8*) back wall.

* *Institute of High Energy Densities, Joint Institute of High Temperatures, Russian Academy of Sciences, ul. Izhorskaya 13/19, Moscow, 127412 Russia*

** *Moscow Institute of Heat Engineering, Berezovaya alleya 10/1, Moscow, 127276 Russia*

1028-3358/02/4712-0856$22.00

zle exterior walls is also possible, which may lead to the nozzle fracture.

In the present paper, we propose a method of experimental and numerical analyses of perturbations that originate when starting a rocket engine and affect its nozzle under high-altitude captive tests. Modeling of the captive tests of a rocket engine was carried out with a test facility composed of a shock tube and a supersonic wind tunnel (Fig. 2). Our model was composed of an axisymmetric diffuser with a nozzle installed and an ejector providing the desired rarefaction in the diffuser. The model was fixed to the shock-tube end wall. The ejector was a square channel with two metallic walls. Two other walls were formed by thick plane-parallel glasses used for shadow photographing processes that occur in the ejector. All features of the axisymmetric gas-dynamic channel used in the high-altitude captive-test bed were reproduced in the model presented in Fig. 2. Moreover, complete geometric similarity was provided in all of the sections except for the square-shaped ejector. Such a change does not affect the gas flow in the vicinity of the nozzle. In the ejector, the change in the shape of the channel cross section causes negligible perturbations with respect to the effect of the ejector jets.

The process of starting the nozzle is simulated for the case when a gas heated behind the reflected shock wave in the shock tube escapes from the nozzle. The desired pressure drop at the nozzle inlet is provided by choosing initial pressures in the shock tube and diffuser, and, in addition, the Mach numbers M_0 for the shock wave in the shock tube.

Visualization and registration of the starting process were performed using an IAB-451 shadow device and a VSK-5 high-speed camera. PSV dynamic-pressure transducers with a time resolution of 1 μs were used for measuring pressure in the diffuser.

Before the onset of the experiment, air in the low-pressure channel of the shock tube was maintained at atmospheric pressure. In order to provide the required rarefaction in the diffuser, compressed air under a stagnation pressure up to 40 atm was injected into the ejector. Then, hydrogen under a pressure of 80 atm was injected into the high-pressure chamber of the shock tube. After a diaphragm between the high-pressure and low-pressure chambers of the shock tube had been broken, a shock wave was formed that reached the shock-tube end with the nozzle installed. As a result of the shock wave's reflection from the shock-tube end, a gas volume appeared at a high pressure and with a high temperature, both determined by the shock Mach number in the shock tube.

The experiments were carried out over a wide range of diffuser pressures (from 0.15 to 1.0 atm) and for various Mach numbers (from 3.05 to 4.28) of the shock in the shock tube. These values of the Mach number ensure a pressure drop near the nozzle inlet of 100 atm with varying diffuser pressure. The pressure transducer *1* (see Fig. 2) measured pressure behind the nozzle, while transducers *2*, *3*, and *4* recorded the propagation of the starting shock wave in the diffuser. As the shock wave propagated in the channel, the pressure amplitude dropped (Fig. 3). Motion of the shock wave reflected by the ejector towards the nozzle was not observed. Shadow photographs of the gas flow in the ejector mixing chamber showed that, when entering the ejector-jet region, the starting shock wave introduced an additional turbulence into the flow, although it subsequently decomposed and transformed into acoustic perturbations.

The experiments have shown that the increase in the pressure on the nozzle exterior wall is caused by the

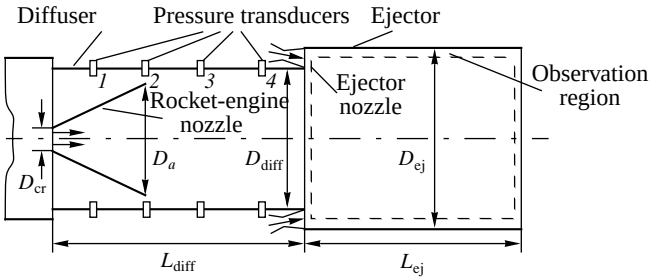

Fig. 2. Layout of the physical model for starting an engine. D_{cr}, D_a, D_{diff}, and D_{ej} are the diameters for the critical cross section of the nozzle, for the nozzle exit section, for the diffuser, and for the ejector, respectively; L_{diff} and L_{ej} are the lengths of the diffuser and ejector. $\frac{D_a}{D_{\text{cr}}} = 6.5$, $\frac{D_{\text{diff}}}{D_a} = 1.1$, $\frac{D_{\text{ej}}}{D_{\text{diff}}} = 1.1$, $\frac{L_{\text{diff}}}{D_{\text{diff}}} = 6$, and $\frac{L_{\text{ej}}}{D_{\text{ej}}} = 9.1$.

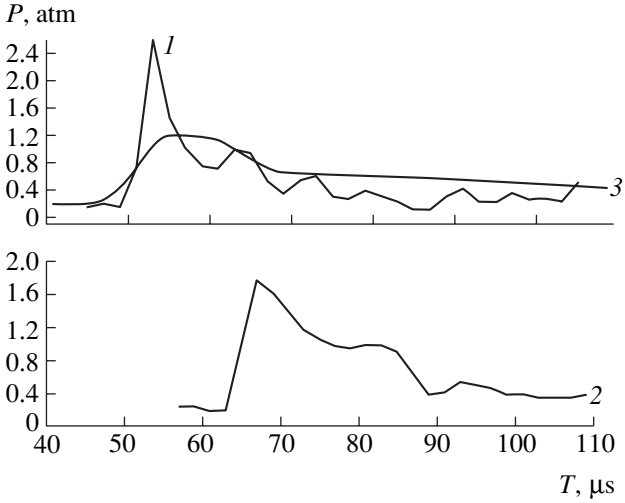

Fig. 3. Readings of the pressure transducers nos. 2 and 3 positioned in the diffuser (curves *1* and *2*, respectively) as functions of time (see Fig. 1). The diffuser pressure is P_0 = 0.15 atm and the shock-wave Mach number is $M_0 = 4.18$. Curve *3* shows the time dependence of the pressure drop calculated for the position of the transducer no. 2.

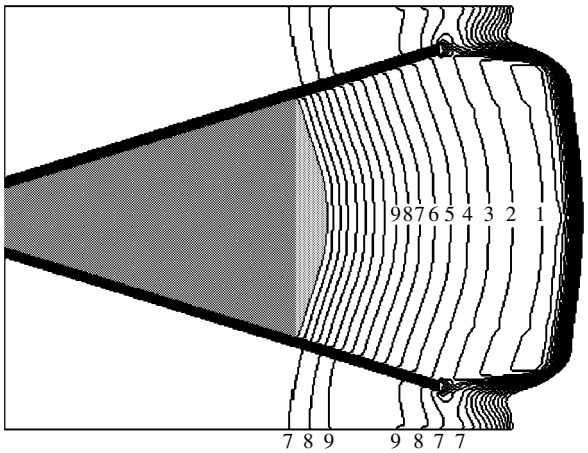

Fig. 4. Isobars found numerically for a two-dimensional unsteady flow at a time moment of 70 μs (the corresponding dimensionless time is equal to unity) after the onset of the outflow from the nozzle. The pressure in the diffuser is P_0 = 0.2 atm, and the rocket-engine jet pressure is 120 atm. Curves from *1* to *9* correspond to pressures of 0.12, 0.14, 0.16, 0.18, 0.20, 0.22, 0.24, 0.26, 0.28 of P_0, respectively.

starting shock wave, while the perturbation due to the interaction of the shock wave with the ejected jet does not affect the nozzle.

The same result follows from our numerical simulation of the process. We have developed an algorithm for evaluating the flow field, which is based on the Steger–Warming finite-difference scheme for solving time-dependent two-dimensional Euler equations. The computational meshes used make it possible to resolve the fronts of leading and secondary shocks with relative errors of about 1% and 10%, respectively. We solved the problem in dimensionless variables, choosing the throat diameter d_1 as the spatial scale and the quantity $\sqrt{\frac{P_2}{\rho_2}}$ as the velocity scale, the latter being smaller by a factor of $\sqrt{\gamma}$ than the sonic velocity in the initial gas. We chose the quantity $\frac{d_1}{\sqrt{P_2/\rho_2}}$ and initial values P_2 and ρ_2 as scales of time, pressure, and density, respectively.

We calculated the starting process of a rocket engine that had been initiated in a high-altitude test bed with an ejector. Initial values for pressure and Mach number corresponded to the experimental conditions. The layout of our facility is shown in Fig. 2. It should be emphasized that, in the mathematical model, the ejector is assumed to have a circular cross section, as in an actual test bed, in contrast to our experiments using the ejector with a square cross section.

The calculation results qualitatively describe the load distribution observed in the experiment. We imply a pressure increase in the region between the nozzle wall and diffuser after the egress of the shock wave from the nozzle (Fig. 4). At the initial time, the pressure outside the nozzle exceeds that inside it by a factor of about 1.5.

The time dependence calculated for the pressure in the diffuser cross sections containing the transducers is smoothed compared to the experimental curve (Fig. 3). At the stage of attaining steady-state flow near the nozzle, the total pressure impulse coincides with the experimental value. According to the calculation results, the reflection of the starting shock wave from the ejector is negligible.

Thus, the pressure measurements, visualization of the process, and numerical simulation show that no reflected shock wave is observed when the starting shock wave interacts with the ejector jets. The diffraction of the starting shock wave by the nozzle-exit section results in the pressure on the nozzle exterior wall becoming higher than that inside the nozzle, which may cause its rupture.

The unsteady wave processes observed should be taken into account when calculating the starting regimes of rocket engines. The proposed method of modeling the test-bed study of rocket engines significantly lowers its cost. The method allows us to optimize the operations of a high-altitude test bed with a full-scale engine and to obtain additional information on loads on the nozzle.

REFERENCES

1. A. A. Shishkov and B. M. Silin, *High-Altitude Tests of Reactive Engines* (Mashinostroenie, Moscow, 1985).
2. V. A. Belavin, V. V. Golub, and I. M. Naboko, Prikl. Mekh. Tekh. Fiz., No. 1, 56 (1979).
3. V. V. Golub, Shock Waves **3**, 279 (1994).
4. T. V. Bazhenova, S. B. Bazarov, O. V. Bulat, *et al.*, Izv. Akad. Nauk, Mekh. Zhidk. Gaza, No. 4, 204 (1993).

Translated by V. Chechin

Doklady Physics, Vol. 47, No. 12, 2002, pp. 859–862. Translated from Doklady Akademii Nauk, Vol. 387, No. 5, 2002, pp. 620–623.

TECHNICAL PHYSICS

Efficiency of the Two-Stage Acceleration of the Working Media of Laser Space Microthrusters

Yu. S. Protasov and Yu. Yu. Protasov

Presented by Academician V.E. Fortov July 25, 2002

Received July 25, 2002

The current status of the development of spacecraft is characterized by the creation of a highly integrated module architecture of a new class of small spacecraft (nanosatellites) for a wide range of scientific and applied problems [1].[1]

The basic requirements for space microthrusters of this class of spacecraft are associated with the possibility of reaching minimum thrust $J \sim 1$–5 nN s with a fine dosage of an individual pulse in a wide range (within four–five orders of magnitude) and high monochromaticity of the accelerated flow $\varepsilon > 0.8$ in the undeveloped micronewton propulsion range $F_p \sim 10^{-7}$–10^{-5} N and specific impulses $I_{sp} \geq 10^3$ s.

An energy–ballistic analysis of promising beam space thrusters (solar and laser thermal, detonation, solar sail [2, 3], etc.) indicates that the pulse and quasi-steady-state laser microthrusters of the erosion type with various mechanisms of creating propulsion (evaporation or detonation), where the working medium in vacuum is exposed to laser radiation with power density $I_0 \sim 10^6$–10^8 W/cm^2, fulfill these requirements most completely and use (as an energy source) high-brightness semiconductor laser diodes with energy efficiency higher than 60% and average radiation power $N_{rad} \sim$ 5–10 W for spacecraft [4].

In the parametric set of erosion-type laser space thrusters (with various forms of optic discharges in vacuum) under development, the generation, heating, and shock-wave acceleration of gas–plasma flows occur at the following successive stages: laser ablation (light erosion) of a solid working medium (easily vaporized dielectric materials and metals) in the target chamber of a thruster, radiative-gas dynamic heating, the formation and acceleration of the plasma under the optic breakdown of the medium, and the generation of a light detonation shock wave in the acceleration chamber of the thruster.

The primary fundamental limit of an erosion-type laser space thruster in the new range of propulsion and minimal thrust is associated with the fact that the ingress of an evaporated substance into the optical discharge in a laser space thruster is delayed by $\sim\Delta t_1 \sim (3$–$5) \times 10^{-6}$ s (Fig. 1b) with respect to the laser pulse due to the lag of phase transitions for any mechanism (resonance or thermal laser ablation, light erosion, or pyrolise) of the generation of the working medium [5]. The absence of a mass yield $\dot{m}(t)$ coordinated with

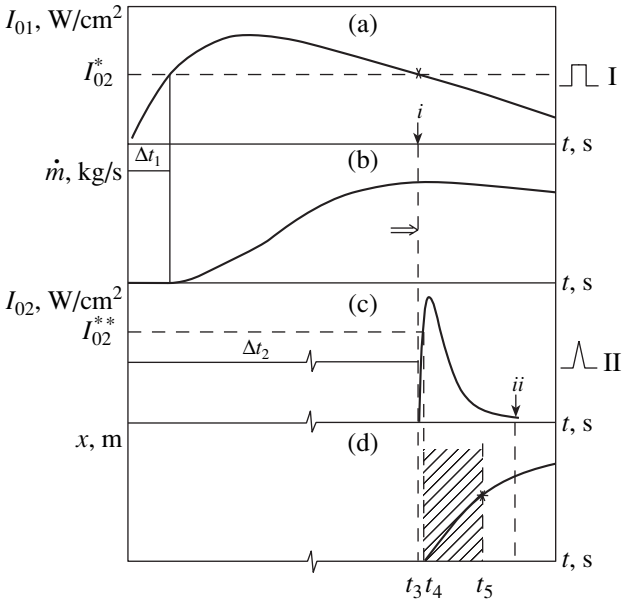

Fig. 1. Timing diagram of the operating processes in a two-stage erosion-type laser space thruster: (a) the power density of the first laser pulse in the irradiation area of a dielectric target, (b) the mass rate of the target working medium in the gaseous phase, (c) the power density of the second, accelerating, laser pulse in the optical-breakdown area, and (d) the x–t diagram of the gas–plasma flow behind the section of the laser space thruster.

[1] According to the definition of the International Aerospace Federation, the class of microspacecraft involves microsatellites with mass 10–20 kg, nanosatellites with mass 1–10 kg, and picosatellites with mass below 1 kg.

Bauman State Technical University,
Vtoraya Baumanskaya ul. 5, Moscow, 107005 Russia
e-mail: protasov@power.bmstu.ru

1028-3358/02/4712-0859$22.00

laser pulse dynamics $I_0(t)$ is responsible for not only the increase in the longitudinal dispersion of velocities and the decrease in the flow monochromaticity $\varepsilon \sim \frac{\overline{v}^2}{\overline{v^2}}$ but also for a considerable tail thrust, because a portion m_2 of the evaporated substance is not involved in the accelerating laser cycle and continues to enter with thermal velocity upon termination of the laser pulse.[2] This circumstance makes it impossible to achieve the necessary minimum thrust and to ensure a fine dosage of controlling pulses and restricts the range of mass-averaged velocities $\tilde{v} \sim 10^5$ cm/s (specific impulses $I_{sp} < 10^3$ s) and frequency characteristics of the laser space thruster.

New possibilities of overcoming these limits are associated with the combined (evaporation and detonation) mechanism of creating propulsion in one operating cycle of the laser thruster. This two-stage scheme of the laser space thruster implies the use of two consistent (in spectral energy and dynamic parameters) laser pulses (heating with $\tau_{p_1} \sim 10^{-4}$ s and accelerating with $\tau_{p_2} \sim 10^{-6}$ s) at the generation stage of the working medium and acceleration stage of the gas–plasma flow in the front of the laser detonation wave.

The aim of our experimental investigations is to determine the capabilities of the two-stage acceleration of active gas–plasma media of erosion-type laser space thrusters. This two-stage mechanism of laser acceleration in a laser space thruster was analyzed theoretically in [6].

Radiation gas dynamics and thermophysical processes in chambers at all stages of transformation of laser-radiation energy in thruster sections and propulsion–energy characteristics of the laser space thruster were examined experimentally on a test bench developed for the LUCH complex [7]. This test bench involves an evacuated ($p_0 \sim 10^{-2}$ Pa, $V_{ch} \sim 1.7$ m^3) thermostabilized chamber with differential pumping and a system of gas–vacuum collectors for preventing the interference of accelerated gas–plasma flows ahead of the section of the laser space thruster. This chamber is electro-optically matched to the module of optical diagnostics and the propulsion measurement module. The laser space thruster unit was mounted in the vacuum chamber on a propulsion measurement platform of high amplitude–frequency sensitivity, which was first developed to determine the pulse and periodic actions ($\Delta\tau_p \sim 10^{-6}$–$10^{-1}$ s, $f_m \sim 2 \times 10^{-2}$ Hz) and to detect microdisplacements [8] (quantitative characteristics of thrust J, propulsion F_{pr}, and specific mechanical recoil momentum $C \sim \frac{m\Delta v}{E_p}$ [N s/J) and involved a torsion balance suspended in vacuum, pendulum trap–calorimeter of gas flows, ballistic pendulum, and piezoelectric sensors of pressure. The module of laser sources of the bench makes it possible to carry radiation ($\lambda_1 = 10.6$, 1.06, and 0.693 μm) pulses ($\tau_p \sim 10^{-7}$–10^{-3} s) to the active chamber of the laser thruster with power density $I_0 = 10^4$–10^9 W/cm^2 and energy density $\frac{E_p}{S_0} \sim 10^{-1}$–$10^2$ J/cm^2. The module of optical diagnostics is designed to determine the space–time fields of densities, temperatures, and velocities of charged and neutral particles in the chamber and outside the laser space thruster. This module involves the complex of pulse holographic interferometry with field visualization, schlieren photodetection of the macrostructure of gas–plasma flows in the laser space thruster chamber prototypes with quartz walls, spectral chronography, and emission and absorption spectroscopy with photoelectric detection of high space–time resolution [9].

A $(CH_2O)_n$ target of various shapes (plane, conic, hemispherical) with a developed surface ($S_0 \sim 0.17$–3.1 cm^2) was situated at the end of a cylindrical molybdenum target chamber connected to the profiled acceleration chamber and two optical entrance units for laser radiation. The characteristic parameters of laser radiation in the tandem are $\lambda_I \sim 1.06$ μm, $I_{01} \sim 10^5$–10^8 W/cm^2, and $\tau_{p_1} \sim 4 \times 10^{-4}$–$3 \times 10^{-5}$ s for the first laser pulse introduced into the target chamber and $\lambda_{II} \sim 1.06$ μm, $I_{02} \sim 10^7$–10^9 W/cm^2, and $\tau_{p_2} \sim 0.7$–1.2×10^{-6} s for the second laser pulse generated with the controlled time delay $\Delta t_2 \sim 10^{-5}$–5×10^{-5} s in the detonation (acceleration) chamber.

Analyzing experimental data obtained for the dynamics of radiative-gas dynamic and thermal processes, stages of solid–gas–plasma phase transitions, heating and shock-wave acceleration of the working medium at optical breakdown of the medium, and the formation of a laser detonation wave in the two-stage laser space thruster, we arrive at the following conclusions.

(i) The optimal mode of the generation of the working medium in the gaseous phase with controlled mass expense [$\dot{m}(t) \sim 10^{-4}$–10^{-6} g/s] and high efficiency of laser ablation $\eta_{la} \sim \frac{\Delta m \tilde{v}}{E_p} \geq 0.8\eta_{le}$ (without condensed phase) is the mode of the maintenance of the laser-induced wave of developed evaporation in the target chamber of the laser space thruster. Since the thermal-ionization wave (i.e., plasma shielding of laser radiation on the radiated target with low thermal conductivity) is absent at this stage (Δt_2), it is possible to deter-

[2] Mass loss m_2 is approximately equal to mass m_1 effectively participating in the acceleration process, and flow monochromaticity for $v_2 \ll v_1$ is $\varepsilon \sim \frac{m_1}{m_1 + m_2}$ and has the physical meaning of the utilization factor of the working medium in the laser space thruster.

mine the optical–thermal and criterion parameters of the action, which are related to controlling parameters $\left(I_{01}, \tau_{p_1}, \frac{E_{p_1}}{S_0}, \ldots \right)$ for realizing time-controlled laser-light erosion and the controlled expense of the working medium of ablated targets, whose chemical composition is complex and whose initial gas density distribution is isotropic until the onset of the optical breakdown (generation of a laser detonation wave). Direct calorimetric measurements of the power and energy of laser radiation absorbed by a $(CH_2O)_n$ target with the developed surface were carried out with a metallic bolometer, which had bismuth thermal resistance and was located in the target. The mechanical recoil momentum $\left(C \sim \frac{m\Delta v}{E_{p_1}} \right)$ was measured by a ballistic pendulum in vacuum. These measurements make it possible to determine the effective heat-transfer coefficient $K_{ht} \sim 0.8$ and to achieve, by multiparametric optimization of the conditions of irradiation of targets, the laser-ablation efficiency $\eta_{la} \sim 0.75$–0.9 (Fig. 2) in the range $10^6 < I_{01} < 7 \times 10^7$ W/cm^2 of the power density of the first laser pulse.

(ii) The dynamics of the shock-wave acceleration stage for the gas–plasma flow in the laser space thruster are determined by the velocity characteristics ($\tilde{v} \sim 5 \times 10^4$ m/s), shape, and macrostructure of the laser detonation wave generated in low-threshold optical breakdown ($I_{02}^{**} \sim 10^8$ W/cm^2, $t_{br} \sim 3 \times 10^{-7}$ s) at the leading edge of the second laser pulse ($t_2 \sim 3 \times 10^{-6}$ s). The acceleration efficiency, which is determined by the condition of optimal space–time matching of the waves of developed evaporation and laser detonation, depends substantially on the dimension relations and profiles of the target and laser-space-thruster chambers and the spectral energy and dynamic parameters of the laser pulses in tandem. By varying the duration τ_{p_1} and shape (slopes of the leading and trailing edges) of the first laser pulse and time delay (Δt_2) of the initiation of the optical breakdown and spatial localization of the generation area of the laser detonation wave in the ranges limited by the conditions for achieving the maximum expense $\dot{m}(\Delta t_2)$, more than 90% of all the gaseous medium falling into the target chamber can be involved into the acceleration cycle. Even under nonoptimal space–time conditions of the development of the laser detonation wave and size ratios of the active chambers of the laser space thruster (dynamics and macrostructure of the interaction area), the measured values of the mass-averaged flow velocities at the section of the laser space thruster and monochromaticity ε (Fig. 2) exceed the respective values achieved at laser space thrusters based on single-stage schemes with evaporation or detonation mechanisms of creating thrust by ~25 and ~30%, respectively.

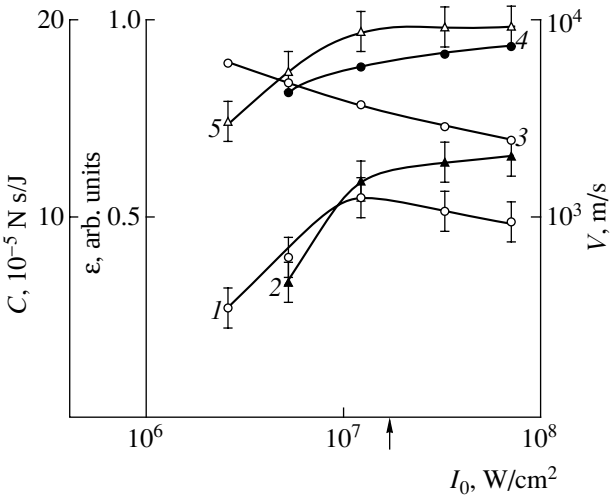

Fig. 2. Experimental data for specific mechanical impulse C in the (*1*) single-stage (evaporation) laser space thruster and (*2*) two-stage laser space thruster (parameters of the second, detonation, laser pulse were $I_{02} \sim 2 \times 10^7$ W/cm^2 and $\tau_p \sim 1.2 \times 10^{-6}$ s), flow monochromaticity ε in the section for (*3*) single-stage and (*4*) two-stage laser space thrusters, and (*5*) mass-averaged velocity v of the flow in the section of the two-stage laser space thruster. All the quantities are given as functions of the power density of laser radiation with $\lambda_{rad} = 1.06$ μm.

(iii) The comparative analysis of the monochromaticity of the flow and specific impulse, propulsion efficiency, and minimum thrust in single-stage and two-stage schemes of erosion laser space thrusters, which have close values of the action parameters ($\Pi_a \sim I_0 \lambda_p^{1/2}$), energy contour, and energy of laser pulses $\frac{E_p}{S_0}$, indicates that, in contrast to laser space thrusters based on the evaporation acceleration mechanism, fine control of the dynamic parameters of thrust is possible within the range of four to five orders of magnitude with minimum ($J_t < 0.05J$) tail thrust in two-stage laser space thrusters.

(iv) In the range of the controlling parameters of the laboratory laser-space-thruster models under investigation, the values experimentally determined for the specific mechanical impulse and mass-averaged velocities are highest for microthrusters of this class of laser space thrusters based on erosion and gas working media. These experimental results are not extreme and can be improved with multiparametric optimization of the dynamics and macrostructure of the laser detonation wave and the geometry of the laser space thruster chambers.

Thus, successive stages of generation (laser ablation), radiative gas dynamic heating, and shock-wave acceleration of the working medium were realized by two matched (in spectral, energy, and dynamic characteristics) laser pulses. This makes it possible to achieve both high thrust efficiency of the transformation of

laser-radiation energy into the kinetic energy of the accelerated gas–plasma flow with minimum thrust and high monochromaticity of the flow and to overcome the fundamental limits of laser space thrusters based on the evaporation mechanism of acceleration in the undeveloped micronewton thrust range of microsatellites.

REFERENCES

1. F. S. Gulczinxki III and M. J. Dulligan, in *Proceedings of the XXXVIII Joint Propulsion Conference on Micropropulsion Research at AFRI*, AIAA Pap. No. 2000-3255.
2. C. R. Phipps, Jr., T. P. Turner, R. F. Harrison, *et al.*, J. Appl. Phys. **64** (3), 1083 (1988).
3. C. R. Phipps and R. F. Harrison, Laser and Particle Beams **8** (2), 281 (1990).
4. C. Rossei, *Design, Fabrication, and Thrust Prediction of Solid Propellant Microthrusters for Space Application: Design, Test, and Microfabrication of MEMS and MOEMS* (IAF, Paris, 1999).
5. R. Lang, S. O. Brien, and S. Demars, *High Power, High Brightness Diode Laser Technology Review* (Albuguergue, N. M., 1998).
6. Yu. S. Protasov and Yu. Yu. Protasov, in *Proceedings of the LII International Astronautic Congress, Toulouse, 2001*, Pap. No. IAF-01.5.6.08.
7. Yu. Yu. Protasov, Vestn. Mosk. Gos. Tekh. Univ., Ser. Mashinostroenie, No. 4, 58 (1997).
8. Yu. S. Protasov and Yu. Yu. Protasov, Izv. Vyssh. Uchebn. Zaved., Mashinostroenie, No. 2, 98 (2002).
9. Yu. S. Protasov, Yu. Yu. Protasov, and V. D. Telekh, *Laser Propulsion: Radiative Gasdynamic and Thermophysical Interchamber Processes of Two-stage Laser Rocket Thruster*, AIAA Pap. No. 2000-3485.
10. Yu. Yu. Protasov, *The Physics of Heat Transfer in Boiling and Condensation* (Nauka, Moscow, 1997), pp. 504–511.
11. *Optical Properties of Ionized Gases at Temperature Up to 100 eV*, Ed. by Yu. S. Protasov (Hemisphere, New York, 1997).

Translated by R. Tyapaev

Doklady Physics, Vol. 47, No. 12, 2002, pp. 863–866. Translated from Doklady Akademii Nauk, Vol. 387, No. 4, 2002, pp. 478–481.

MECHANICS

Gripping a Mobile Object with a Manipulating Robot Controlled via the Internet

I. R. Belousov, V. V. Sazonov, and S. Yu. Chebukov

Presented by Academician D.E. Okhotsimskiĭ June 27, 2002

Received June 28, 2002

Remote control of robots over the Internet is a promising new direction of scientific research. Among its possible applications are remote training, remote control of automated production, control of robots residing in extreme conditions (e.g., the Internet was used for controlling the Sojourner mobile robot for navigation on the Martian surface [1]).

In the Keldysh Institute of Applied Mathematics, Russian Academy of Sciences, methods for controlling robots via the Internet network are being developed. These methods employ mathematical models of a robot and of its working space in the online regime [2–5]. Such an approach made it possible to use a convenient control medium and, to a certain extent, to overcome the existence of indeterminate time delays in a communication channel. The time delays are especially crucial in the case of interaction of a robot with a mobile object. Based on a dynamic model of an object, which is capable of predicting its motion, and on a technical-vision system that supplies the robot with data required for predicting measurements and gives an operator a view of the robot's workspace, we have managed to realize the control of such an interaction.

In the experiments being described, a rod vibrating on a bifilar suspension (similar to a gymnastic trapeze) having three degree of freedom was used as a mobile object. Vibrations of the rod were recorded by two TV cameras. One of them was attached to an immobile beam to which the upper ends of the suspension threads were fixed, while the other was situated to the side of the rod. Previously, an algorithm of rapid automatic gripping of a rod by a manipulating robot supplied with only one TV camera was developed and successfully tested in the experiments described in [6, 7]. Below, we deal with an analogous experiment not automated but being controlled by a remote operator via the Internet. In this new experiment, the quantities to be measured, mathematical models, and algorithms are strongly redundant and universal. This makes the system stable with respect to time delays and reduces requirements for its preliminary adjustment.

1. The following scenario of the experiment is proposed. At the moment of initiation of the control code, the rod is immovably suspended, and the manipulating robot is in the initial position outside the region in which the rod must move. A remote operator choosing a point on the image of the rod, which is generated by the computer model, sets the initial motion of the rod. Then, the robot excites vibrations of the rod by grabbing the chosen point with a random velocity. The control code (at the server side) determinates the motion of the rod, calculates the moment of time for gripping and the rod position at this moment, controls the robot, and identifies whether the grip does occur or the attempt for gripping should be repeated.

The listed problems are solved in the same manner as in [6, 7]. The only difference consists in employing more perfect cameras, algorithms for the primary treatment of visual information, and algorithms for the determination and prediction of the movement.

The cameras are digital, and they are connected to a computer by an IEEE 1394 bus (Fire Wire). Each camera yields an RGB24 color picture at a resolution of 640×480 pixels and at a frequency of 15 frames per second. The rod ends are supplied with red markers, whose images in the camera's pictures can be recognized with minimal calculation expenditures. The coordinates of these images are transmitted to the client side in real-time mode with the help of software packages, yielding network traffic of 0.1 kb s^{-1}. Results illustrating the potentialities of the code that determines the marker positions in the camera's picture planes are shown in Fig. 1 (for the camera located on a side of the workspace).

The cameras were calibrated such that the coordinates (measured in the robot's reference system and expressed in millimeters) of a point (e.g., of the rod end) in the robot's workspace could be calculated according to the coordinate (expressed in a number of pixels) of the image in simultaneous frames of both cameras. Unfortunately, the coordinates of the ends of

Keldysh Institute of Applied Mathematics, Russian Academy of Sciences, Miusskaya pl. 4, Moscow, 125047 Russia
e-mail: belousov@keldysh.ru; sazonov@keldysh.ru; chebukov@gh60keldysh.ru

1028-3358/02/4712-0863$22.00

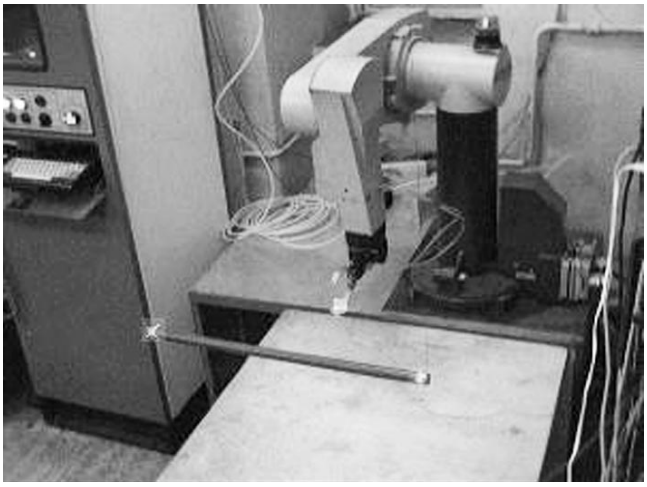

Fig. 1. Rod image in the lateral TV camera.

the rod image in the frames of two cameras relate to different moments of time. In order to find these coordinates at the same moments, interpolation must be applied. It is constructed by the least-square technique according to data segments covering a time interval of 5 s or longer. The functions 1, t and $\sin\frac{\pi k t}{T}$ $(k = 1, 2, \ldots)$ were used as basis functions. Here, t is time reckoned from the onset of the interpolation segment and T is the length of this segment [8]. Using the interpolation constructed on the uniform mesh with a step of 0.1, the coordinates of the rod ends in the robot's reference system are calculated. These coordinate sequences are used for estimating parameters of the rod as a linear vibration system and serve for predicting its motion.

2. Estimation of the parameters is performed under the assumption that the z axis in the manipulating robot's reference system is directed vertically, the rod in its equilibrium position is horizontal and, together with its suspension threads, forms an equilateral trapezoid. The normal coordinates in such a coordinate system are related to the coordinates of the rod end (x_1, y_1, z_1) and (x_2, y_2, z_2) by the relationships

$$\theta = \arctan\frac{x_1 - x_2}{y_1 - y_2},$$

$$\xi = \frac{(x_1 + x_2)\cos\alpha - (y_1 + y_2)\sin\alpha}{2}, \qquad (1)$$

$$\eta = \frac{(x_1 + x_2)\sin\alpha + (y_1 + y_2)\cos\alpha}{2}.$$

Here, α is the angle between the y axis and the rod in its quiescent position. The counting-off direction for this angle is adjusted to the z-axis direction. Prior to the experiment, the value of the angle α is unknown. The normal coordinates introduced above have the following sense. The θ coordinate describes torsional vibrations of the rod, in which its middle point belongs to an invariant vertical straight line. The ξ coordinate describes rod vibrations as a swing. Finally, the η coordinate describes the rod vibrations in which the rod and the threads are situated in an invariant vertical plane. It is assumed that in the case of small rod vibrations, the time dependence of the normal coordinates is given by the formulas

$$\theta = \alpha + e^{-\mu_1 t}(c_1\cos\nu_1 t + c_2\sin\nu_1 t),$$

$$\xi = \xi_0 + e^{-\mu_2 t}(c_3\cos\nu_2 t + c_4\sin\nu_2 t), \qquad (2)$$

$$\eta = \eta_0 + e^{-\mu_3 t}(c_5\cos\nu_3 t + c_6\sin\nu_3 t).$$

Here, α, ξ_0, η_0 c_i, μ_j, and ν_j are constant parameters, α being the same angle as in formulas (1). The values of the parameters are found step by step using the least-square technique. Initially, the values of the function θ are calculated on the basis of the first expression of formula (1) and of the coordinates of the rod ends on the uniform mesh with the step of 0.1 (see above). Then, constants α, ν_1, μ_1, c_1, and c_2 are determined from the condition of the best approximation of these values by the first expression of formula (2) (cf. [6, 7]). The knowledge of the angle α allows the values of the functions ξ and η to be calculated. Further, in accordance with these values, the other parameters entering into formula (2) are found. In particular, for the rod being used, $\nu_1 = 3.28\ \text{s}^{-1}$, $\nu_2 \approx \nu_3 \approx 2.07\ \text{s}^{-1}$, $0 < \mu_j < 0.1\ \text{s}^{-1}$.

The knowledge of the parameters in formulas (2) make it possible to use them for predicting the values of the normal coordinates at $t > T$. Since the normal coordinates are Lagrangian coordinates for the rod, the problem of predicting its movement is solved. This is an approach that was accepted in [6, 7], although it requires knowledge of a number of geometric characteristics of the suspension. In order to avoid the necessity of this knowledge, we used another approach. The representation of normal coordinates by formulas (2) implies that the time variation of the rod end coordinates may be approximately described by relationships of the form (only the relationship for the x_1 coordinate is presented)

$$x_1 = a_0 + \sum_{j=1}^{7} e^{-\mu_j t}(a_j\cos\nu_j t + b_j\sin\nu_j t), \qquad (3)$$

$$\mu_4 = 2\mu_1, \quad \nu_4 = 2\nu_1, \quad \mu_5 = \mu_2 + \mu_3,$$

$$\nu_5 = \nu_2 + \nu_3, \quad \mu_6 = \mu_7 = \mu_1 + \frac{\mu_2 + \mu_3}{2},$$

$$\nu_6 = \nu_1 + \frac{\nu_2 + \nu_3}{2}, \quad \nu_7 = \nu_1 - \frac{\nu_2 + \nu_3}{2}.$$

Here, the parameters μ_j and ν_j are considered to be unknown. The coefficients a_0, a_j, and b_j are found by the

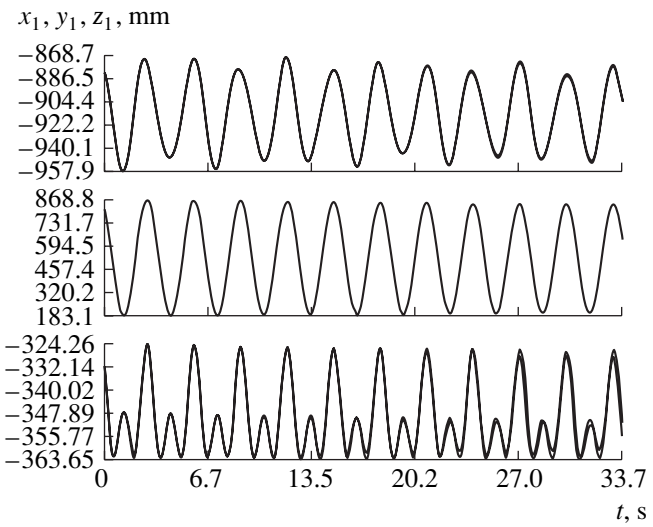

Fig. 2. Determination and prediction of the motion for one of the rod ends.

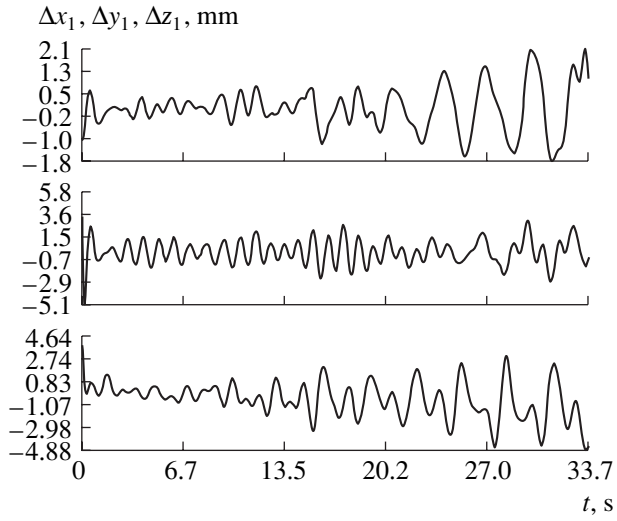

Fig. 3. Errors in the determination and prediction of the motion for one of the rod ends.

least-square technique under the condition of the best approximation of the rod end coordinates in the segment $0 \le t \le T$ by expressions of type (3). When deriving expressions (3), in the expansions of these coordinates in a series over normal coordinates, only terms with a degree not higher than two are preserved. In addition, we allowed for the relationship $\nu_1 \approx \nu_2$. If the amplitude of torsional vibrations of the rod does not exceed 20°, then the above method makes it possible to predict the rod-end coordinates in the segment $T \le t \le 2T$ with an error smaller than 5 mm. This error is quite acceptable for performing the successful gripping.

Examples of the operation of the block determining the motion are presented in Figs. 2 and 3. Figure 2 demonstrates plots for six functions that are virtually pairwise coincident. The plots for differences of the functions forming pairs are shown in Fig. 3. One of the functions of each pair describes the virtual time variation for the corresponding coordinate of one of the rod ends. This function is constructed by the above method in accordance with the measurement data obtained by the TV cameras. The other function of the pair corresponds to expression (3) that approximates the first function. The approximation is carried out according to the data contained in the segment $0 \le t \le 10$ s. For $t >$ 10 s, the second function should be considered as a prediction for the variation of the corresponding coordinate with time. Within the scope of this interpretation, Fig. 3 illustrates the accuracy of the prediction.

3. The operator interface is shown in Fig. 4. The graphic window presented on the right-hand side of the figure demonstrates the three-dimensional position of the robot and the rod. In order to map all objects of the work scene at the server side, it is necessary to transmit only several numbers (angles in robot hinges and rod-end coordinates). Therefore, the scene is drawn in real time even for slow communication channels. Elements of the control interface are situated on the left-hand side of the figure. On pushing the "Start" key (on the left, below), the server control code is initiated, and the robot strikes the rod in order to excite its vibrations. After the observation of the rod's motion by an operator, he chooses a desired grip point. To do this, he pushes the keys "+" and "–" displacing the goal point on the rod image. The command for performing the gripping is given by pushing the "Grasp" key. The grip signal is transmitted to the server, after which the server control code grips in the automated mode. The algorithms of the robot control for the case of gripping are described in [6, 7]. The operator observes the gripping process in the graphic window. He is able to stop the process and to vary its scenario.

The algorithms described were verified at a test table including the PM-01 manipulating robot with a Sfera-36 control stand. The server control code was operated with a computer equipped with the Windows 2000 operating system. The robot received commands via an RS 232 interface. The data exchange with the client side (i.e., the operator interface) was realized with TCP/IP sockets. When developing the client side, Java and Java3D open technologies were employed, which provided operations via standard Web browsers for an arbitrary computer base. During the experiments, an operator residing at a long distance from the robot successfully gripped a vibrating rod.

4. The method described of remote control for the case of gripping a mobile object makes it possible to use the operator's skill in planning at the upper level of an operation with the possibility to automatically perform its final stage. This approach turns out to be rather useful in solving other problems of the control of robots interacting with mobile objects. The methods developed can turn out to be especially efficient for the remote control of robots in the case of delays in com-

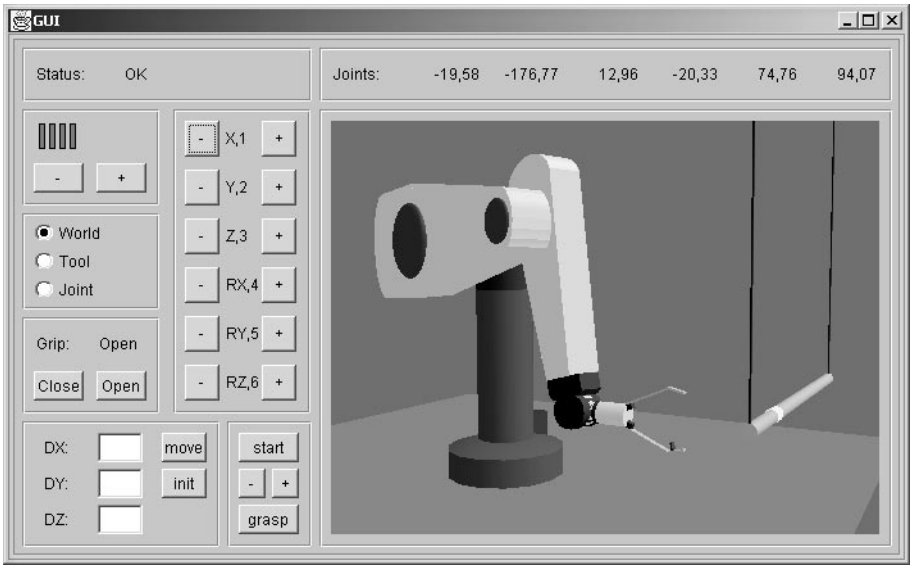

Fig. 4. Interface of a remote operator.

munication channels. In particular, such a situation takes place in modeling, testing in laboratory conditions, and directly gripping objects in extraterrestrial space, which is realized with the help of remotely controlled robotics systems.

ACKNOWLEDGMENTS

This work was supported by the Russian Federal Purposeful Program "Integration of Higher Education and Fundamental Science," by the complex program of scientific research of the Presidium of the Russian Academy of Sciences (RAS), by the RAS–CNRS agreement, and by the Russian Foundation for Basic Research, project no. 02-07-90223.

REFERENCES

1. P. Backes, K. Tso, J. Norris, *et al.*, in *Proceedings of the IEEE International Conference on Robotics and Automation, San Francisco, April 2000*, pp. 2025–2032.
2. I. R. Belousov, in *Proceedings of the VIII All-Russia Conference on Theoretical and Applied Mechanics, 23–29 August, Perm, 2001*, pp. 91–92.
3. I. Belousov, R. Chellali, and G. Clapworthy, in *Proceedings of the IEEE International Conference on Robotics and Automation, 21–26 May, Seoul, 2001*, pp. 1878–1883.
4. R. Alami, I. Belousov, S. Fleury, *et al.*, in *Proceedings of the IEEE/RSJ International Conference on Intelligent Robots and Systems, 30 October–5 November, Takamatsu, 2000.*
5. I. R. Belousov, Dokl. Akad. Nauk **383** (2), 198 (2002) [Dokl. Phys. **47**, 241 (2002)].
6. I. R. Belousov, A. A. Boguslavskiĭ, S. N. Emel'yanov, *et al.*, Izv. Ross. Akad. Nauk, Mekh. Tverd. Tela, No. 4, 102 (1998).
7. D. Okhotsimsky, A. Platonov, I. Belousov, *et al.*, in *Proceedings of the IEEE International Conference on Robotics and Automation, Leuven, May 1998*, pp. 1683–1688.
8. C. Lanczos, *Applied Analyses* (Prentice-Hall, Englewood Cliffs, New York, 1957; Fizmatgiz, Moscow, 1961).

Translated by G. Merzon

Doklady Physics, Vol. 47, No. 12, 2002, pp. 867–871. Translated from Doklady Akademii Nauk, Vol. 387, No. 4, 2002, pp. 482–486.

MECHANICS

A Fluctuation-Dissipation Model for the Motion of the Pole of the Deformable Earth

Yu. G. Markov* and I. N. Sinitsyn**

Presented by Academician V.V. Kozlov June 19, 2002

Received June 17, 2002

1. Trajectories of the motion of the instantaneous position of Earth's pole represent the complex evolution of a dynamic system. Monitoring data of the International Earth-Rotation Service for the last 15–20 years indicates that the following components are separated in the complex motion of the Earth's pole: the principal component (free nutation or Chandler wobble) with an amplitude of 0.20″–0.25″ and a period of (433 ± 2) sidereal days [1]; the regular annual component with an amplitude of about 0.07″–0.08″; and relatively slow irregular drift (trend) of the axis of the Earth's figure. According to [2, 3], the annual wobbles of the Earth's axis are induced by the solar gravitational moment, by the orbital motion of the rotating Earth, and by the diurnal tides of the Earth's mantle. The causes and mechanism responsible for the excitation of annual wobbles are usually attributed to seasonal geophysical phenomena [4, 5].

There are a large number of articles devoted to the linear statistical analysis of measurements of the motion of the Earth's pole (see, e.g., review [6]). An analytical stochastic model of the motion of the Earth's pole with allowance for tidal deformations in the form of humps and protrusions was developed in [7] on the basis of celestial mechanics. In this study, we further develop this model and take into account the moments of gravitational forces of the Moon, the moments of dissipative forces, and fluctuation moments of forces associated with the higher harmonics of the deformable-Earth figure.

2. The motion of the deformable-Earth pole can be described by the following phenomenological three-dimensional nonlinear stochastic differential system of equations:

$$\dot{p} + N_* q = 3V_1 b\omega_*^2 \cos\omega_* t - V_4 r^2 + P(t, p, q, r, \mathbf{V}, \mathbf{\Phi}), \quad (1)$$

$$p(t_0) = p_0;$$

$$\dot{q} - N_* p = -3V_2 b\omega_*^2 \cos\omega_* t + V_5 r^2 + Q(t, p, q, r, \mathbf{V}, \mathbf{\Phi}), \quad q(t_0) = q_0; \quad (2)$$

$$\dot{r} = -3V_3\omega_*^2(b' + b''\cos 2\omega_* t) + R(t, p, q, r, \mathbf{V}, \mathbf{\Phi}), \quad r(t_0) = r_0, \quad (3)$$

where

$$P = P(t, p, q, r, \mathbf{V}, \mathbf{\Phi}) = -3V_2V_6d_1(b\omega_*^2\cos\omega_* t + b_1\omega_{1*}^2\cos\omega_{1*}t) - 3V_3V_5d_1[\omega_*^2(b' + b''\cos 2\omega_* t) + \omega_{1*}^2(b_1' + b_1''\cos 2\omega_{1*}t)] - 3V_1b_1\omega_{1*}^2\cos\omega_{1*}t - D_1p + \Phi_1(t),$$

$$Q = Q(t, p, q, r, \mathbf{V}, \mathbf{\Phi}) = -3V_1V_6d_2(b\omega_*^2\cos\omega_* t + b_1\omega_{1*}^2\cos\omega_{1*}t) - 3V_3V_4d_2[\omega_*^2(b' + b''\cos 2\omega_* t) + \omega_{1*}^2(b_1' + b_1''\cos 2\omega_{1*}t)] - 3V_2b_1\omega_{1*}^2\cos\omega_{1*}t - D_2q + \Phi_2(t), \quad (4)$$

$$R = R(t, p, q, r, \mathbf{V}, \mathbf{\Phi}) = -3V_1V_2d_3(b\omega_*^2\cos\omega_* t + b_1\omega_{1*}^2\cos\omega_{1*}t) + 3V_1V_5d_3(b\omega_*^2\cos\omega_* t + b_1\omega_{1*}^2\cos\omega_{1*}t) - 3V_3\omega_{1*}^2(b_1' + b_1''\cos 2\omega_{1*}t) - D_3r + \Phi_3(t).$$

* *Moscow State Institute of Aviation, Volokolamskoe sh. 4, Moscow, 125080 Russia*

** *Institute of Informatics Problems, Russian Academy of Sciences, ul. Vavilova 30/6, Moscow, 117900 Russia*

1028-3358/02/4712-0867$22.00

Here, $p = p_t$, $q = q_t$, and $r = r_t$ are the projection of the terrestrial angular velocity on the Earth's axes [3, 5]; V_1, V_2, and V_3 are random parameters obtained by averaging the axial moments of inertia of the deformable Earth over the diurnal interval $T_* = 2\pi r_*^{-1}$:

$$V_1 = \frac{1}{T_*}\int_t^{t+T_*}\frac{\tilde{C}(\tau)-\tilde{B}(\tau)}{A^*}\cos r_*\tau d\tau,$$

$$V_2 = \frac{1}{T_*}\int_t^{t+T_*}\frac{\tilde{C}(\tau)-\tilde{A}(\tau)}{B^*}\sin r_*\tau d\tau, \qquad (5)$$

$$V_3 = \frac{1}{T_*}\int_t^{t+T_*}\frac{\tilde{B}(\tau)-\tilde{A}(\tau)}{C^*}\sin 2r_*\tau d\tau,$$

which characterize the effective diurnal tidal humps from the Sun and the Moon; and V_4, V_5, and V_6 are the random parameters associated with the centrifugal moments of inertia of the deformable Earth:

$$V_4 = \frac{J^*_{qr}}{A^*} + \frac{1}{T_*}\int_t^{t+T_*}\frac{\tilde{J}_{qr}(\tau)}{A^*}d\tau,$$

$$V_5 = \frac{J^*_{pr}}{B^*} + \frac{1}{T_*}\int_t^{t+T_*}\frac{\tilde{J}_{pr}(\tau)}{B^*}d\tau, \qquad (6)$$

$$V_6 = \frac{J^*_{pq}}{C^*} + \frac{1}{T_*}\int_t^{t+T_*}\frac{\tilde{J}_{pq}(\tau)}{C^*}d\tau,$$

determining the effective tidal protrusions; $A^* + \tilde{A}(t)$, $B^* + \tilde{B}(t)$, $C^* + \tilde{C}(t)$ and $J^*_{pq} + \tilde{J}_{pq}(t)$, $J^*_{qr} + \tilde{J}_{qr}(t)$, $J^*_{rp} + \tilde{J}_{rp}(t)$ are the axial and centrifugal moments of inertia of the Earth, respectively, where the constant components of the inertia tensor are marked by the asterisk, and the variable components induced by the solar and lunar diurnal tides, by the tilde; $D_{1,2,3}$ are the specific coefficients of the moments of dissipative forces; and $\Phi_1(t) = \Phi_{1t}$, $\Phi_2(t) = \Phi_{2t}$, and $\Phi_3(t) = \Phi_{3t}$ are the specific fluctuation moments of forces and $\mathbf{\Phi}_t = [\Phi_{1t}\Phi_{2t}\Phi_{3t}]^T$. The magnitude of the fluctuation-dissipation moments of forces is assumed to be much smaller than that of the moments of forces from the tidal deformations. We denote the random initial conditions as

$$V_7 = p_0, \quad V_8 = q_0, \quad V_9 = r_0. \qquad (7)$$

In addition, we introduce the notation

$$N_* = (C^* - B^*)A^{*-1}\omega_*, \quad r_* = 365\omega_*,$$

$$2b' = \left(1 - \frac{b^2}{2}\right), \quad 2b'' = -b^2,$$

$$2b_1' = \left(1 - \frac{b_1^2}{2}\right), \quad 2b_1'' = b_1^2, \quad d_1 = \frac{B^*C^*}{A^*}, \qquad (8)$$

$$d_2 = \frac{A^*C^*}{B^*}, \quad d_3 = \frac{A^*B^*}{C^*},$$

where ω_* and ω_{1*} are constants determined by the gravitational and focal parameters of the Sun and Moon and $b_1 \approx \frac{b}{20}$, where b is a known parameter [3].

When setting up the system of Eqs. (1)–(3), we took into account that the terms involving r, r^2, ω_*, ω_*^2, ω_{1*}, and ω_{1*}^2 considerably exceed the corresponding terms involving the squares and products of p, q, $\frac{\dot{\tilde{C}}}{C^*}$, $\frac{\dot{\tilde{J}}_{pr}}{A^*}$, $\frac{\dot{\tilde{J}}_{rq}}{B^*}$, etc.

3. Let us introduce the following notation for the mathematical expectations, variances, covariance functions, and covariances:

$$m_t^p = Mp_t, \quad m_t^q = Mq_t, \quad m_t^r = Mr_t,$$

$$D_t^p = Mp_t^{02}, \quad D_t^q = Mq_t^{02}, \quad D_t^r = Mr_t^{02},$$

$$K^p_{t,t'} = Mp_t^0 p_{t'}^0, \quad K^q_{t,t'} = Mq_t^0 q_{t'}^0, \quad K^r_{t,t'} = Mr_t^0 r_{t'}^0, \qquad (9)$$

$$K^{pq}_{t,t'} = Mp_t^0 q_{t'}^0, \quad K^{qr}_{t,t'} = Mq_t^0 r_{t'}^0, \quad K^{rp}_{t,t'} = Mr_t^0 p_t^0,$$

where M is the symbol of the mathematical expectation (statistical averaging) and the zero in the superscripts denotes centered random components of the real random functions p_t, q_t, and r_t.

We will use Eqs. (1)–(3) under the condition that parameters V_i are real Gaussian random variables with mathematical expectations m_i^V, variances D_i^V, and covariances K_{ij}^V ($i, j = 1, 2, \ldots, 9$) and the fluctuation moments of forces Φ_{it} are real Gauss–Markov processes with known one-dimensional densities. As the initial conditions for p_t^0, q_t^0, and r_t^0, we take the mathematical expectations $m_{t_0}^{p,q,r}$, variances $D_{t_0}^{p,q,r}$, and covariances $K_{t_0}^{pq}$, $K_{t_0}^{qr}$, and $K_{t_0}^{rp}$.

Applying the theory of nonlinear stochastic differential systems [8, 9] to Eqs. (1)–(3), we arrive at the fol-

lowing final expressions for mathematical expectations, variances, covariances, and covariance functions for the times t and $t' > t$:

$$m_t^{p,q,r} = \sum_{i=1}^{9} \psi_{i,t}^{p,q,r} m_i^V + \Delta m_t^{p,q,r},$$

$$D_t^{p,q,r} = \sum_{i=1}^{9}\sum_{j=1}^{9} \psi_{i,t}^{p,q,r}\psi_{j,t}^{p,q,r} K_{ij}^V + \Delta D_t^{p,q,r}, \quad (10)$$

$$K_{t,t'}^{p,q,r} = \sum_{i=1}^{9}\sum_{j=1}^{9} \psi_{i,t}^{p,q,r}\psi_{j,t'}^{p,q,r} K_{ij}^V + \Delta K_{t,t'}^{p,q,r}, \quad (11)$$

$$K_{t,t'}^{pq} = \sum_{i=1}^{9}\sum_{j=1}^{9} \psi_{i,t}^{p}\psi_{j,t'}^{q} K_{ij}^V + \Delta K_{t,t'}^{pq},$$

$$K_{t,t'}^{qr} = \sum_{i=1}^{9}\sum_{j=1}^{9} \psi_{i,t}^{q}\psi_{j,t'}^{r} K_{ij}^V + \Delta K_{t,t'}^{qr}, \quad (12)$$

$$K_{t,t'}^{rp} = \sum_{i=1}^{9}\sum_{j=1}^{9} \psi_{i,t}^{r}\psi_{j,t'}^{p} K_{ij}^V + \Delta K_{t,t'}^{rp}.$$

Here, the Green's functions $\psi_{i,t}^{p,q,r}$ of the parameters V_i are obtained by solving Eqs. (1)–(3) at $P = Q = R = 0$ and replacing p_t, q_t, and r_t with $\psi_{i,t}^{p,q,r}$ and are equal to

$$\psi_{1,t}^{p} = -\psi_{2,t}^{q} = b_0\omega_* \sin\omega_* t,$$

$$\psi_{2,t}^{p} = \psi_{1,t}^{q} = -N_* b_0 \cos\omega_* t,$$

$$\psi_{3,t}^{r} = -3b'\omega_*^2(t - t_0)$$

$$-\frac{3}{2}b''\omega_*(\sin 2\omega_* t - \sin 2\omega_* t_0),$$

$$\psi_{4,t}^{q} = \psi_{5,t}^{p} = -r_0^2 N_*^{-1}, \quad (13)$$

$$\psi_{7,t}^{p} = \psi_{8,t}^{p} = \cos N_*(t - t_0),$$

$$\psi_{8,t}^{p} = -\sin N_*(t - t_0) = -\psi_{7,t}^{q}, \quad \psi_{9,t}^{r} = 1,$$

$$\psi_{9,t}^{p,q} = \psi_{7,t}^{r} = \psi_{8,t}^{r} = 0,$$

$$b_0 = 3b\omega_*^2(\omega_*^2 - N_*^2)^{-1}.$$

The $\Delta m_t^{p,q,r}$, $\Delta D_t^{p,q,r}$, $\Delta K_{t,t}^{p,q,r}$, $\Delta K_{t,t'}^{pq}$, $\Delta K_{t,t'}^{qr}$, and $\Delta K_{t,t'}^{pr}$ are the components of the mathematical expectations, variances, and covariances that take into account the nonlinear functions P, Q, and R.

In the framework of the correlation theory of nonlinear stochastic systems [8, 9], Eqs. (1)–(4) are equivalent to the Gaussian stochastic differential system of equations, where the nonlinear functions $V_{4,5}r^2$, P, Q, and R are replaced by the linearly normalized ones with respect to p_t^0, q_t^0, and r_t^0 according to the formulas

$$V_i V_j \approx m_i^V m_j^V + K_{ij}^V + m_i^V V_j^0 + m_j^V V_i^0,$$

$$i, j = 1, 2, 3, 4, 5,$$

$$V_i r^2 \approx m_i^V (m_t^r)^2 + m_i^V D_t^r + 2m_t^r K_{it}^{Vr} \quad (14)$$

$$+ [(m_t^r)^2 + D_t^r]V_i^0 + 2(m_i^V m_t^r + K_{it}^{Vr})r_t^0,$$

$$i = 4, 5.$$

As a result, we arrive at the equivalent Gaussian system

$$\dot{m}_t^p = -N_* m_t^q - D_1 m_t^p + m_1^V F_{1t} - m_4^V F_{2t} + F_{4t},$$

$$m_{t_0}^p = m_0^p = Mp_0,$$

$$\dot{m}_t^q = N_* m_t^p - D_2 m_t^q - m_2^V F_{1t} + m_5^V F_{2t} + F_{5t}, \quad (15)$$

$$m_{t_0}^q = m_0^q = Mq_0,$$

$$\dot{m}_t^r = -D_3 m_t^r - m_3^V F_{3t} + F_{6t}, \quad m_{t_0}^r = m_0^r = Mr_0,$$

which is nonlinear for the mathematical expectations $m_t^{p,q,r}$ and linear for the centered components p_t^0, q_t^0, and r_t^0,

$$\dot{p}_t^0 = -N_* q_t^0 - D_1 p_t^0 - F_{7t} r_t^0 + F_{1t} V_1^0 - F_{9t} V_2^0$$

$$- F_{11t} V_3^0 - F_{8t} V_4^0 - F_{12t} V_5^0 - F_{10t} V_6^0 + \Phi_{1t},$$

$$p_{t_0}^0 = p_0^0,$$

$$\dot{q}_t^0 = N_* p_t^0 - D_2 q_t^0 + F_{13t} r_t^0 - F_{14t} V_1^0 - F_{1t} V_2^0$$

$$- F_{16t} V_3^0 - F_{17t} V_4^0 + F_{8t} V_5^0 + F_{15t} V_6^0 + \Phi_{2t}, \quad (16)$$

$$q_{t_0}^0 = q_0^0,$$

$$\dot{r}_t^0 = -D_3 r_t^0 - F_{18t} V_1^0 - F_{19t} V_2^0$$

$$- F_{3t} V_3^0 + F_{20t} V_5^0 + \Phi_{3t},$$

$$r_{t_0}^0 = r_0^0.$$

Here,

$$\chi_{1t} = b\omega_*^2 \cos\omega_* t + b_1\omega_{1*}^2 \cos\omega_{1*} t,$$

$$\chi_{2t} = \omega_*^2(b' + b''\cos 2\omega_* t) + \omega_{1*}^2(b_1' + b_1''\cos 2\omega_{1*} t),$$

$$F_{1t} = 3\chi_{1t}, \quad F_{2t} = r_0^2, \quad F_{3t} = 3\chi_{2t},$$

$$F_{4t} = -\{m_4^V[(m_t^r)^2 - r_0^2] + m_4^V D_t^r + 2m_t^r K_{4t}^{Vr}$$
$$+ 3(m_2^V m_6^V + K_{26}^V)d_1\chi_{1t} + 3(m_3^V m_5^V + K_{35}^V)d_1\chi_{2t}\},$$
$$F_{5t} = m_5^V[(m_t^r)^2 - r_0^2] + m_5^V D_t^r + 2m_t^r K_{5t}^{Vr}$$
$$- 3(m_1^V m_6^V + K_{16}^V)d_2\chi_{1t} - 3(m_3^V m_4^V + K_{34}^V)d_2\chi_{2t},$$
$$F_{6t} = -3(m_1^V m_2^V + K_{12}^V)d_3\chi_{1t}$$
$$+ 3(m_1^V m_5^V + K_{15}^V)d_3\chi_{1t},$$
$$F_{7t} = 2(m_4^V m_t^r + K_{4t}^{Vr}), \quad F_{8t} = (m_t^r)^2 + D_t^r,$$
$$F_{9t} = 3m_6^V d_1\chi_{1t}, \quad F_{10t} = 3m_2^V d_1\chi_{1t},$$
$$F_{11t} = 3m_5^V d_1\chi_{2t}, \quad F_{12t} = 3m_3^V d_1\chi_{2t},$$
$$F_{13t} = 2(m_5^V m_t^r + K_{5t}^{Vr}), \quad F_{14t} = 3m_6^V d_2\chi_{1t},$$
$$F_{15t} = 3m_1^V d_2\chi_{1t}, \quad F_{16t} = 3m_4^V d_2\chi_{2t},$$
$$F_{17t} = 3m_3^V d_2\chi_{2t}, \quad F_{18t} = 3(m_2^V - m_5^V)d_3\chi_{1t},$$
$$F_{19t} = 3m_1^V d_3\chi_{1t}, \quad F_{20t} = 3m_1^V d_3\chi_{1t}.$$

4. For the random fluctuation moments of forces $\mathbf{\Phi}_t$ in the form of Gaussian white noise, applying the formulas of the theory of linear stochastic differential systems [8, 9] to Eqs. (16) and the equations for the parameters $\dot{V} = 0$, we obtain the following system of ordinary differential equations determining the fluctuation-dissipation correlation model of motion

$$\dot{m}_t = c(\bar{m}_t, \bar{K}_t), \quad m_0 = M\Omega_{t_0}, \tag{17}$$

$$\dot{\bar{K}}_t = a_t(\bar{m}_t, \bar{K}_t)K_t + \bar{K}_t a_t^T(\bar{m}_t, \bar{K}_t) + b_t\nu_t b_t^T, \quad \bar{K}_0 = \bar{K}_{t_0}; \tag{18}$$

$$\frac{\partial \bar{K}_{t,t'}}{\partial t'} = \bar{K}_{t,t'}a_{t'}^T(\bar{m}_{t'}, \bar{K}_{t'}), \quad \bar{K}_{t,t} = \bar{K}_t. \tag{19}$$

Here, $m_t = M\Omega_t$, where $\Omega_t = [\omega_t^T V^T]^T$ is the joint vector; T is the transposition symbol; $\boldsymbol{\omega}_t = [p_t q_t r_t]^T$ is the mathematical expectation of the angular velocity ω_t; $K_t = M\Omega_t^0\Omega_t^{0T}$ ($\Omega_t^0 = \Omega_t - m_t$) is the covariance matrix Ω_t, $\nu_t = [\nu_{ijt}]$ is the matrix of the white-noise intensities Φ_t; $\mathbf{c}(\bar{m}_t, \bar{\mathbf{K}}_t)$ is the vector consisting of the right-hand sides of Eqs. (15) and equations for the parameters V: $\dot{V} = 0$; and a_t and b_t are the matrices of the coefficients of Ω_t^0 and Φ_t in Eqs. (16) and $\dot{V} = 0$.

Hence, we immediately obtain the formulas (averaged over $2\pi\omega_*^{-1}$) for the mathematical expectations $\langle m_t^{p,q,r}\rangle$, variances $\langle D_t^{p,q,r}\rangle$, and covariances $\langle K_t^{pq,qr,rp}\rangle$, as well as, in the case of stationary white noise, the formulas for the covariance functions $k_\tau^{p,q,r} = K_{t,t+\tau}^{p,q,r}$ and the spectral densities $\langle s^{p,q,r}(\lambda)\rangle$ as the corresponding Fourier transforms.

In the case of non-Gaussian parameters $\mathbf{V}$ and fluctuations $\mathbf{\Phi}$ [10], the model given by Eqs. (17)–(19) can be used as an approximation.

5. The analysis of Eqs. (17)–(19) provides the following qualitative conclusions.

(i) In the absence of fluctuation-dissipation moments ($D_i = 0$, and $\Phi_{it} = 0$, $i = 1, 2, 3$) and the Moon's attraction ($b_1 = b_1' = b_1'' = 0$), the nonlinear differential correlation model given by Eqs. (15) and (16) coincides with the model proposed in [7].

(ii) In the linear approximation (in the absence of protrusions and humps of V_2, V_3, V_4, and V_5), the fluctuation-dissipation moments in the presence of stationary white noise Φ_t lead to random forced fluctuations with finite constant variances and covariances determined from Eqs. (18) and (19) for spectral-correlation characteristics:

$$a_1 K + K a_1^T + \nu = 0, \tag{20}$$

$$k_\tau' = a_1 k_\tau, \quad s(\lambda) = \Psi(i\lambda)\nu\Psi(i\lambda)^*, \tag{21}$$

where $K = K_t = M\omega_t^0\omega_t^{0T}$ is the matrix of variances and covariances of the angular velocity; $k_\tau = M\omega_t^0\omega_{t+\tau}^{0T}$ is the covariance matrix; a_1 is the matrix of the coefficients of p_t^0, q_t^0, and r_t^0 in Eqs. (16); $\Psi(i\lambda)$ is the transfer function over the variables p_t^0, q_t^0, and r_t^0 that corresponds to the matrix a_1; and the asterisk denotes complex conjugation. A particular case where $r = r_0$, $D_1 = D_2$, and $\Phi_1 = \Phi_2$ and the case of stationary white noise were considered in [6].

(iii) The presence of humps and protrusions $V_i = 1, 2, \ldots, 6$ results in, first, additional stochastic fluctuations at higher frequencies $n\omega_*$ and $n_1\omega_{1*}$ ($n \geq 2$); second, time-dependent trends t^h ($h > 2$); and third, cross-correlation constraint in variables p_t, q_t, and r_t due to the nonlinearity of Eqs. (1) and (2) with respect to r^2. In particular, the average statistical trend in the variables p_t and q_t is determined by Eqs. (15) and (16) available in [7] with the additional terms

$$\langle \Delta m_t^{p,q}\rangle = \{m_{5,4}^V[(m_t^r)^2 - r_0^2] + m_{5,4}^V D_t^r + 2m_t^r K_{5,4t}^{Vr}\}N_*^{-1}, \tag{22}$$

where $m_t^r = Mr_t$, D_t^r is the variance of r_t^0, and $K_{5,4t}^{Vr}$ is the covariances of $V_{4,5}$ and r_t^0.

ACKNOWLEDGMENTS

This work was supported by the Russian Foundation for Basic Research, project nos. 01-02-17250 and 01-01-00758.

REFERENCES

1. *IERS Annu. Rep. 1990, July 1991–1999, July 2000* (Central Burea IERS Observ., Paris, 2000).
2. L. D. Akulenko, S. A. Kumakshev, and Yu. G. Markov, Dokl. Akad. Nauk **379** (2), 191 (2001) [Dokl. Phys. **46**, 508 (2001)].
3. L. D. Akulenko, S. A. Kumakshev, and Yu. G. Markov, Dokl. Akad. Nauk **382** (2), 199 (2002) [Dokl. Phys. **47**, 78 (2002)].
4. W. Munk and G. McDonald, *The Rotation of the Earth* (Cambridge Univ. Press, Cambridge, 1960; Mir, Moscow, 1964).
5. H. Moritz and I. I. Mueller, *Earth Rotation: Theory and Observation* (Ungar, New York, 1987; Naukova Dumka, Kiev, 1992).
6. M. Arato, *Linear Stochastic Systems with Constant Coefficients. A Statistic Approach* (Springer, Berlin, 1982; Nauka, Moscow, 1989).
7. Yu. G. Markov and I. N. Sinitsyn, Dokl. Akad. Nauk **385** (2), 189 (2002).
8. V. S. Pugachev and I. N. Sinitsyn, *Theory of Stochastic Systems* (Logos, Moscow, 2000).
9. V. S. Pugachev and I. N. Sinitsyn, *Stochastic Differential Systems: Analysis and Filtering* (Nauka, Moscow, 1990; Wiley, New York, 1987).
10. I. N. Sinitsyn, Dokl. Akad. Nauk **348** (3), 327 (1996) [Phys. Dokl. **41**, 218 (1996)].

Translated by Yu. Vishnyakov

Doklady Physics, Vol. 47, No. 12, 2002, pp. 872–875. Translated from Doklady Akademii Nauk, Vol. 387, No. 4, 2002, pp. 487–490.

MECHANICS

Solution of the Wang-Chang–Uhlenbeck Master Equation

F. G. Cheremisin

Presented by Academician V.V. Rumyantsev July 15, 2002

Received July 16, 2002

Nonequilibrium processes in a gas with internal degrees of freedom of molecules can be studied by using the generalized Boltzmann equation, the Wang-Chang–Uhlenbeck equation, where the internal and translational degrees of freedom are considered in the framework of quantum and classical mechanics, respectively. For small deviations from local thermodynamic equilibrium, an asymptotic method developed for this equation yields hydrodynamic equations including the effect of the internal degrees of freedom on the viscosity and thermal conduction of the gas [1].

The aim of this study is to develop a numerical method of solving the Wang-Chang–Uhlenbeck equation for an arbitrary degree of gas nonequilibrium.

The Wang-Chang–Uhlenbeck equation can be written in the form

$$\frac{\partial f_i}{\partial t} + \xi_i \frac{\partial f_i}{\partial \mathbf{x}} = \sum_{j,k,l} \int_{-\infty}^{\infty} \int_{\Omega} (f_k f_l - f_i f_j) g \sigma_{ij}^{kl} d\Omega d\xi_j. \quad (1)$$

Here, $d\Omega = \sin\theta d\theta d\varphi$, $f_i \equiv f(i, \xi, \mathbf{x}, t)$ is the distribution function, where i is the set of quantum numbers determining the internal state of the molecule; ξ_i is the velocity of the molecule in the ith state; $g = |\xi_i - \xi_j|$; indices i, j and k, l correspond to the molecular states before and after the collision, respectively; and σ_{ij}^{kl} is the cross section for the collision responsible for this change of the internal states. There is no summation with respect to the repeated index i.

The cross sections for direct and inverse collisions are related as

$$g\sigma_{ij}^{kl}(g, \theta, \varphi) d\xi_i d\xi_j = g^* \sigma_{kl}^{ij}(g^*, \theta, \varphi) d\xi_k d\xi_l. \quad (2)$$

The magnitude $g^* = |\xi_k - \xi_l|$ of the velocity after the collision and velocities ξ_k and ξ_l are determined from the laws of conservation

$$g^* = g\sqrt{1 - \frac{4\Delta e}{mg^2}}, \quad \xi_k = \xi_0 - 0.5\mathbf{g}^*, \quad \xi_l = \xi_0 + 0.5\mathbf{g}^*. \quad (3)$$

Here, m is the molecular mass; $\Delta e = e_l + e_k - e_i - e_j$, where e_i is the energy of the ith internal state; and $\xi_0 = 0.5(\xi_i + \xi_j)$.

The condition $mg^2 \geq 4\Delta e$ determines the admissibility of the transition $(i, j) \longrightarrow (k, l)$. We set $\sigma_{ij}^{kl} = 0$ for forbidden transitions. The probability of the transition $(i, j) \longrightarrow (k, l)$ is defined as

$$p_{ij}^{kl} = \frac{\sigma_{ij}^{kl}}{\sigma_{ij}}, \quad \sigma_{ij} = \sum_{k,l} \sigma_{ij}^{kl}$$

and satisfies the condition $0 \leq p_{ij}^{kl} \leq 1$ and the normalization condition

$$\sum_{k,l} p_{ij}^{kl} = 1. \quad (4)$$

We assume that σ_{ij} is independent of the internal molecular state and is equal to the elastic scattering cross section $\sigma_{ij} = \sigma_0(g, \theta)$. The introduction of quantities σ_0 and p_{ij}^{kl} obviously transforms Eq. (1).

The problem of numerically solving the Wang-Chang–Uhlenbeck equation reduces to the construction of a method of calculating its right-hand side, the generalized collision operator, which can be represented as $I_i = -L_i + G_i$, where

$$L_i = \sigma_0 \sum_{j,k,l} \int_V \int_\Omega f_i f_j p_{ij}^{kl} g d\Omega d\xi_j, \quad (5)$$

$$G_i = \sigma_0 \sum_{j,k,l} \int_V \int_\Omega f_k f_l p_{ij}^{kl} g d\Omega d\xi_j. \quad (6)$$

As in the case of the classical Boltzmann equation [2, 3], an effective numerical method must ensure that

Computer Center, Russian Academy of Sciences, ul. Vavilova 40, GSP-1, Moscow, 117967 Russia
e-mail: tcherem@ccas.ru

1028-3358/02/4712-0872$22.00

the collision operator be (i) conservative and (ii) equal to zero on the equilibrium distribution function.

Operators L_i and G_i are calculated on the $j_m \times S_0$ lattice, where S_0 is the uniform lattice in volume V of velocity space and j_m is the number of quantum levels. Similar to the case of a one-atom gas [2], we consider the functional

$$Q(\Phi, f_i) = \sigma_0 \sum_{i,j,k,l} \int_{-\infty}^{\infty}\int_{-\infty}^{\infty}\int_{\Omega} \Phi f_i f_j p_{ij}^{kl} d\Omega d\xi_i d\xi_j. \quad (7)$$

Taking functions $\Phi(\xi)$ in the form

$$\Phi' = 0.5[\delta_{ni}\delta(\xi^* - \xi_i) + \delta_{nj}\delta(\xi^* - \xi_j)], \quad (8)$$

$$\Phi^* = 0.5[\delta_{nk}\delta(\xi^* - \xi_k) + \delta_{nl}\delta(\xi^* - \xi_l)], \quad (9)$$

where δ_{nq} is the Kronecker delta and $\delta(\xi^* - \xi)$ is the three-dimensional δ function, we obtain

$$L_n(\xi^*) = Q(\Phi', f_i), \quad (10)$$

$$G_n(\xi^*) = Q(\Phi^*, f_i). \quad (11)$$

Functions (10) and (11) are calculated on the uniform cubic lattice consisting of N_ν sites $S_\nu = \{i, j, k, l, \xi_i, \xi_j, \theta, \varphi\}_\nu$ such that $(\xi_i)_\nu, (\xi_j)_\nu \in S_0$. Let $(\xi_i)_\nu \equiv \xi_{\alpha_\nu}$ and $(\xi_j)_\nu \equiv \xi_{\beta_\nu}$. Values $(\xi_k)_\nu$ and $(\xi_l)_\nu$ for each site of this lattice are calculated by Eq. (3). The arrangement of vectors ξ_i, ξ_j, ξ_k, and ξ_l for the νth site of cubic lattice S_0 is schematically shown in Fig. 1, where the three-dimensional velocity lattice is given as a plane lattice and subscript ν is omitted. Value $L'_{n,\gamma} \equiv L'_n(\xi_\gamma)$ calculated in site $\xi^* = \xi_\gamma \in S_0$ by Eq. (10) is determined by the part of the cubic sum for $i_\nu = n$, $\alpha_\nu = \gamma$ and $j_\nu = n$, $\beta_\nu = \gamma$ as

$$L'_{n,\gamma} = B\sum_\nu (\delta_{ni_\nu}\delta_{\gamma\alpha_\nu} + \delta_{nj_\nu}\delta_{\gamma\beta_\nu})\Delta_\nu, \quad (12)$$

where $B = \dfrac{2\pi\sigma_0 j_m^2 V}{N_\nu}$, $\Delta_\nu = f_{i_\nu, a_\nu} f_{j_\nu, \beta_\nu} (p_{ij}^{kl})_\nu g_\nu \sin\theta_\nu$, and $f_{i,\alpha} \equiv f(i, \xi_\alpha, \mathbf{x}, t)$. In what follows, the subscript ν will be omitted where possible. Since velocities ξ_k and ξ_l are not in the sites of lattice S_0, $G'_{n,\gamma}$ is calculated with the replacement of Eq. (9) by projector Φ^{**} into pairs of sites ξ_λ, $\xi_{\lambda+s}$ and ξ_μ, $\xi_{\mu-s}$, which are nearest to ξ_k and ξ_l and are shown in Fig. 1:

$$\Phi^{**}(\xi_\gamma) = (1-r)[\delta_{n\lambda}\delta(\xi_\gamma - \xi_\lambda) + \delta_{n\mu}\delta(\xi_\gamma - \xi_\mu)] + r[\delta_{n,\lambda+s}\delta(\xi_\gamma - \xi_{\lambda+s}) + \delta_{n,\mu-s}\delta(\xi_\gamma - \xi_{\mu-s})],$$

where $s = (s_1, s_2, s_3)$ is the vector whose components take values 0, –1, and 1 and that determines the site that is nearest to ξ_k and shown in Fig. 1. As a result,

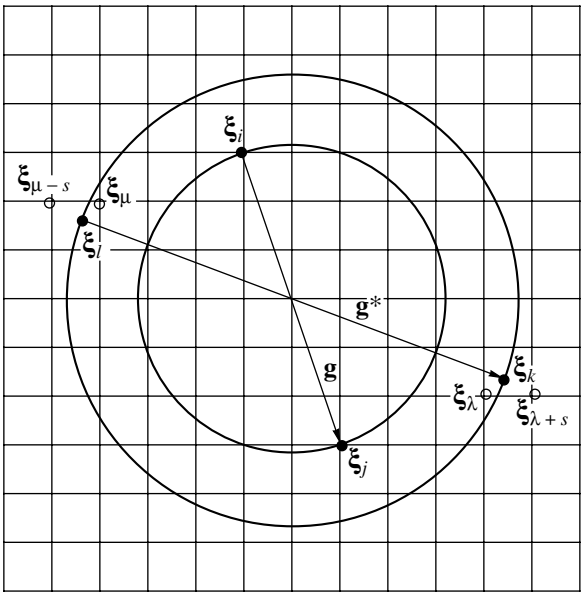

Fig. 1. Scheme of an inelastic collision.

$$G'_{n,\gamma} = B\sum_\nu \{[(1-r)(\delta_{nk}\delta_{\gamma\lambda} + \delta_{nl}\delta_{\gamma\mu}) + r(\delta_{nk}\delta_{\gamma,\lambda+s} + \delta_{nl}\delta_{\gamma,\mu-s})]\Delta\}_\nu. \quad (13)$$

Coefficient r_ν is determined from the laws of conservation for each site of the cubic formula, i.e., for each contribution Δ_ν to operators $L'_{n,\gamma}$ and $G'_{n,\gamma}$. The conservation of mass follows from the form of Φ^{**}, and the conservation of momentum follows from the symmetric arrangement of lattice sites ξ_λ, $\xi_{\lambda+s}$ and ξ_μ, $\xi_{\mu-s}$ with respect to vectors ξ_k and ξ_l. In terms of the notation

$$E_0 = \frac{m\xi_k^2}{2} + \frac{m\xi_l^2}{2}, \quad E_1 = \frac{m\xi_\lambda^2}{2} + \frac{m\xi_\mu^2}{2},$$

$$E_2 = \frac{m\xi_{\lambda+s}^2}{2} + \frac{m\xi_{\mu-s}^2}{2},$$

the law of energy conservation, when contribution Δ_ν is split, has the form $E_0 = (1-r)E_1 + rE_2$. Therefore, $r = \dfrac{E_0 - E_1}{E_2 - E_1}$, which satisfies the condition $0 \le r \le 1$, because either $E_1 \le E_0 \le E_2$ or $E_2 \le E_0 \le E_1$. It is important that r_ν is independent of Δ_ν. For this reason, additional lattice sites ξ_{λ_ν}, ξ_{μ_ν}, $\xi_{\lambda_\nu + s_\nu}$, and $\xi_{\mu_\nu - s_\nu}$ and coefficient r_ν can be preliminarily determined for each site of cubic lattice S_ν, and then extended lattice S_ν^* can be used repeatedly, e.g., in various sites of physical space.

Each contribution Δ_ν can be treated as the result of a "collision" transferring molecules from sites i, j to sites λ, μ and $\lambda + s$, $\mu - s$. In order to ensure that condition (ii) above is satisfied, we consider a pair of inverse collisions to sites i, j from sites λ, μ and $\lambda + s$, $\mu - s$ with weights $(1 - r^*)$ and r^*, respectively. The probability p_{kl}^{ij} is determined from Eq. (2), and coefficient r^*, from the condition

$$E_1\Delta^{(1)}(1-r^*) + E_2\Delta^{(2)}r^* = E_0[\Delta^{(1)}(1-r^*) + \Delta^{(2)}r^*],$$

where

$$\Delta^{(1)} = f_{k,\lambda}f_{l,\mu}p_{ij}^{kl}g\sin(\theta),$$
$$\Delta^{(2)} = f_{k,\lambda+s}f_{l,\mu-s}p_{ij}^{kl}g\sin(\theta).$$

As a result, $r^* = \dfrac{\Delta^{(1)}r}{\Delta^{(1)}r + \Delta^{(2)}(1-r)}$.

An analysis similar to the above gives the contribution of inverse collisions in the form

$$L_{n,\gamma}^* = B\sum_\nu\{(1-r^*)(\delta_{nk}\delta_{\gamma\lambda} + \delta_{nl}\delta_{\gamma\mu})\Delta^{(1)} + r(\delta_{nk}\delta_{\gamma,\lambda+s} + \delta_{nl}\delta_{\gamma,\mu-s})\Delta^{(2)}\}_\nu, \quad (14)$$

$$G_{n\gamma}^* = B\sum_\nu\{(\delta_{ni}\delta_{\gamma\alpha} + \delta_{nj}\delta_{\gamma\beta})[(1-r^*)\Delta^{(1)} + r^*\Delta^{(2)}]\}_\nu. \quad (15)$$

Finally, the collision operators are determined as

$$L_{n,\gamma} = \frac{1}{2}(L'_{n,\gamma} + L^*_{n,\gamma}), \quad G_{n,\gamma} = \frac{1}{2}(G'_{n,\gamma} + G^*_{n,\gamma}).$$

For any (arbitrarily rough) lattice of integration sites S_ν, condition (ii) is satisfied to within an accuracy no worse than $O(h)$, where h is the step of lattice S_0. For degenerate levels of internal energy, Eq. (1) must be modified so as to reduce the number of substantial levels.

Let j_m levels be separated into J_M groups of degenerate levels, $J = 0, 1, \ldots, J_M$, with degeneration degree q_J. We determine the distribution function as $F_J = \sum_q f_q = q_J f_q$, where $q \in J$. Substituting $\sigma_{ij}^{kl} = \sigma_0 p_{ij}^{kl}$ into Eq. (1), summing this equation over the groups of levels i, j, k, and l forming degenerate levels I, J, K, and L, and returning to the old notation, we arrive at the equation

$$\frac{\partial f_i}{\partial t} + \xi_i\frac{\partial f_i}{\partial \mathbf{x}} = \sigma_0\sum_{j,k,l}\int_{-\infty}^{\infty}\int_\Omega(q_iq_jf_kf_l - q_kq_lf_if_j)gp_{ij}^{kl}d\Omega d\boldsymbol{\xi}_j, \quad (16)$$

for which Eqs. (12)–(15) are valid with the change $\Delta \longrightarrow q_kq_l\Delta$, $\Delta^{(1)} \longrightarrow q_iq_j\Delta^{(1)}$, and $\Delta^{(2)} \longrightarrow q_iq_j\Delta^{(2)}$.

The method was tested by solving two spatially uniform $\left(\dfrac{\partial}{\partial \mathbf{x}} = 0\right)$ problems, where the model of constant cross section σ_0 = const was accepted, and the number of the spectral levels was taken to be $j_m = 21$. The physical characteristics of the spectra were taken for a nitrogen molecule from [4]. The characteristic dimensional parameters were the gas density n, the initial translational temperature T_0, and the mean-free-path time τ at this temperature. The Maxwellian initial distribution function in translational velocities was taken. Lattices S_0 and S_ν consisted of 3582 and about 0.5×10^6 sites, respectively, and the time step was $\Delta t = 0.005\tau$. Time integration was performed according to the scheme in [2, 3].

In the first example, the relaxation of vibrational levels is calculated and Eq. (1) is solved. The jth level has energy $e_j^\nu = \hbar\omega\left(j + \dfrac{1}{2}\right)$, and the equilibrium distribution for temperature T_ν is

$$n_j^\nu = nZ_\nu^{-1}\exp\left[-\frac{\hbar\omega(j+1/2)}{T_\nu}\right], \quad (17)$$

where Z_ν is the vibrational partition function. For nitrogen, $\dfrac{\hbar\omega}{k}$ = 3340 K, where k is Boltzmann's constant. Temperature T_0 is taken to be equal to 6680, and the initial vibrational temperature is $T_\nu^{(0)} = 2T_0$. Probabilities p_{ij}^{kl} are arbitrarily taken to be equal to 1 and 0.2 for elastic and inelastic collisions and are then normalized according to (4).

Figure 2 shows the vibrational spectrum for t = (solid line) 0, (diamonds) 1, and (crosses) 6. The latter spectrum coincides with (dashed line) distribution (17) for equilibrium temperature $T_\nu = 1.4T_0$.

The second example concerns the relaxation of rotational levels. The level with the rotational quantum number j has the degeneracy degree $q_j = 2j + 1$ and

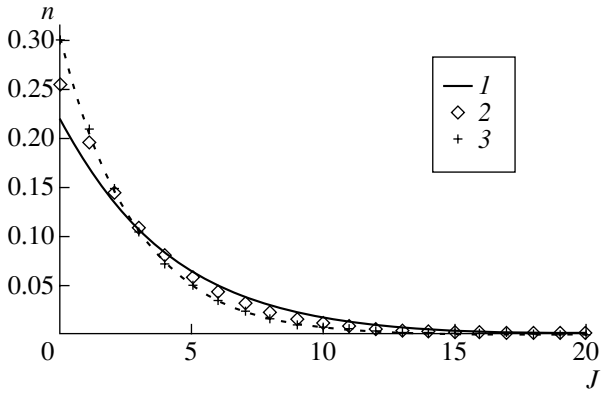

Fig. 2. Evolution of the vibrational spectrum.

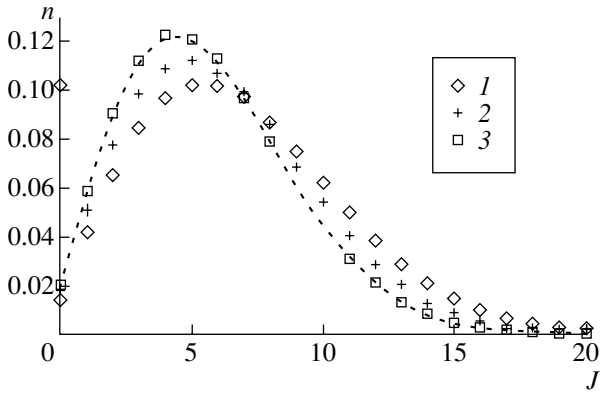

Fig. 3. Evolution of the rotational spectrum.

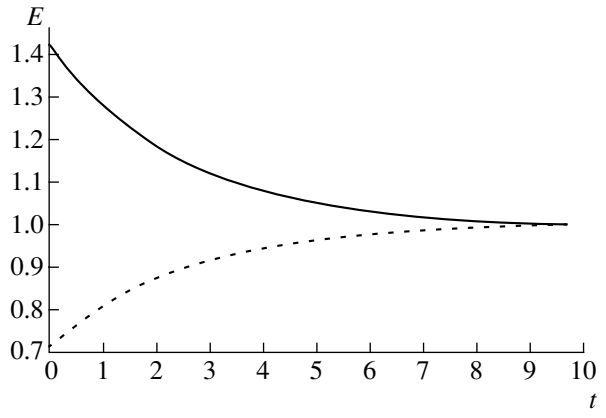

Fig. 4. Variation in the level energies.

energy $e_j^{\mathrm{r}} = \dfrac{\hbar^2 j(j+1)}{2I_{\mathrm{r}}}$, where I_{r} is the moment of inertia of the molecule. The equilibrium distribution of the gas density n over levels for temperature T_{r} is given by the expression

$$n_j^{\mathrm{r}} = nZ_{\mathrm{r}}^{-1}(2j+1)\exp\left[-\frac{\hbar^2 j(j+1)}{2I_{\mathrm{r}}T_{\mathrm{r}}}\right]. \qquad (18)$$

Transition probabilities p_{ij}^{kl} are taken from [5, 6], where the molecular nitrogen was simulated. The problem is solved for $T_0 = 100$, initial rotation temperature $T_{\mathrm{r}}^{(0)} = 2T_0$, and $\dfrac{\hbar^2}{2I_{\mathrm{r}}k} = 2.9$ K.

Figure 3 shows the rotational spectrum for t = (diamonds) 0, (crosses) 3, and (squares) 10. The latter spectrum coincides with (dashed line) the equilibrium spectrum for $T_{\mathrm{r}} = 1.4T_0$.

Figure 4 shows the time dependence of energy per degree of freedom: (solid line) $E_{\mathrm{r}}^* = \dfrac{5E_{\mathrm{r}}}{2(E_{\mathrm{r}}^{(0)} + E_{\mathrm{k}}^{(0)})}$, where $E_{\mathrm{r}} = \sum_j e_j^r n_j^r$ is the rotational energy, E_{k} is the kinetic energy, and superscript (0) means values for t = 0; and (dashed line) $E_{\mathrm{k}}^* = \dfrac{5E_{\mathrm{k}}}{3(E_{\mathrm{r}}^{(0)} + E_{\mathrm{k}}^{(0)})}$.

Each variant was calculated on a PIII 800 MHz computer for about one hour.

The above examples demonstrate that the Wang-Chang–Uhlenbeck master equation for a gas with nondegenerate and degenerate internal degrees of freedom can be solved numerically by the method proposed above.

ACKNOWLEDGMENTS

This work was supported by the Russian Foundation for Basic Research, project no. 01-01-00078.

REFERENCES

1. J. H. Ferziger and H. J. Kaper, *Mathematical Theory of Transport Processes in Gases* (North-Holland Publ. Company, Amsterdam, 1972; Mir, Moscow, 1976).
2. F. G. Cheremisin, Dokl. Akad. Nauk **357** (1), 53 (1997) [Phys. Dokl. **42**, 607 (1997)].
3. F. G. Tcheremissine, Int. Ser. Numer. Math. **141**, 883 (2001).
4. L. D. Landau and E. M. Lifshitz, *Course of Theoretical Physics*, Vol. 5: *Statistical Physics* (Pergamon Press, Oxford, 1977; Nauka, Moscow, 1995).
5. C. Bartels and A. E. Beylich, in *Proceedings of the XX International Symposium on Rarefied Gas Dynamics* (Peking Univ. Press, Beijing, 1997), pp. 749–754.
6. A. E. Beylich, *An Interplaced System for Nitrogen Gas* (Technische Hochschule, Aachen, 2000), p. 14.

Translated by R. Tyapaev

Doklady Physics, Vol. 47, No. 12, 2002, pp. 876–879. Translated from Doklady Akademii Nauk, Vol. 387, No. 5, 2002, pp. 624–626.

MECHANICS

The Penetration of Cylindrical Strikes through Obstacles Made of Concrete and Sandy Ground

S. A. Afanas'eva, N. N. Belov, and N. T. Yugov

Presented by Academician S.S. Grigoryan July 4, 2002

Presented July 10, 2002

When developing protective constructions for underground structures, it is necessary to evaluate their capability to withstand intense dynamic loads. One of the effective methods of solving this problem is mathematical modeling of the deformation and failure of such constructions under shock or blast.

The problem of impact interaction between cylindrical strikes and concrete obstacles was solved in [1], where the failure of concrete was calculated in a phenomenological approach with the strength criteria expressed in terms of invariant relations between the critical macroscopic parameters, stresses and strains, of the process. Comparison of mathematical modeling with the results of an *ad hoc* developed experiment indicated that this approach to the static failure problem can also be applied to calculate failures in concrete under dynamic loading.

In this study, we propose a mathematical model based on the mechanics of continua in order to calculate the behavior of sandy ground under dynamic loading.

Soft sandy ground is considered as a three-component medium characterized by the initial density $\rho_0 = \nu_1\rho_{01} + \nu_2\rho_{02} + \nu_3\rho_{03}$ and moisture content w_0 [2], where ρ_{0i} (i = 1, 2, 3) are the initial densities of air, water, and quartz, respectively; and

$$\nu_1 = 1 - \nu_2 - \nu_3,\ \nu_2 = \frac{w_0\rho_0}{(1 + w_0)\rho_{03}},\ \text{and}\ \nu_3 = \frac{\rho_0}{(1 + w_0)\rho_{03}}$$

are the bulk concentrations of the respective components. Since $\nu_1\rho_{01}$ is less than the initial density ρ_0 by several orders of magnitude, the effect of air in pores can be neglected, and the sandy ground can be considered as a porous material consisting of a matrix, which is a simple water–quartz mixture, and voids (pores).

The specific volume of the porous medium υ is represented as the sum of the specific volume of the matrix υ_m and the specific volume of pores υ_p. The porosity of the material is characterized by the relative volume of voids $\xi = \nu_1$ or by the parameter $\alpha = \dfrac{\upsilon}{\upsilon_m}$, which are related as $\alpha = \dfrac{1}{1-\xi}$.

The system of equations describing the motion of a porous elastoplastic medium has the form

$$\frac{d}{dt}\int_V \rho dV = 0, \quad \frac{d}{dt}\int_V \rho\mathbf{u}dV = \int_S \mathbf{n}\cdot\sigma dS,$$
$$\frac{d}{dt}\int_V \rho E dV = \int_S \mathbf{n}\cdot\sigma\cdot\mathbf{u}dS, \tag{1}$$
$$\mathbf{e} = \frac{\mathbf{s}^J}{2\mu} + \lambda\mathbf{s}, \quad \mathbf{s}:\mathbf{s} = \frac{2}{3}\sigma_T^2,$$

where t is the time; V is the integration volume; S is its surface; $\mathbf{n}$ is the unit outer-normal vector; ρ is the density; $\sigma = -p\mathbf{g} + \mathbf{s}$ is the stress tensor; $\mathbf{s}$ is its deviator; p is the pressure; $\mathbf{g}$ is the metric tensor; $\mathbf{u}$ is the velocity; $E = \varepsilon + \dfrac{\mathbf{u}\cdot\mathbf{u}}{2}$ is the specific total energy; ε is the specific internal energy; $\mathbf{e} = \mathbf{d} - \dfrac{(\mathbf{d}:\mathbf{g})\mathbf{g}}{3}$ is the deviator of the strain rate tensor $\mathbf{d} = \dfrac{1}{2}(\nabla\mathbf{u} + \nabla\mathbf{u}^T)$; $\mathbf{s}^J = \dot{\mathbf{s}} + \mathbf{s}\omega - \omega\mathbf{s}$ is the derivative of the stress-tensor deviator in the sense of Jaumann–Noll; $\omega = \dfrac{1}{2}(\nabla\mathbf{u}^T - \nabla\mathbf{u})$ is the tensor of the vortex;

$$\mu = \mu_{m0}(1-\xi)\left[1 - \frac{(6\rho_{m0}c_{m0}^2 + 12\mu_{m0})\xi}{9\rho_{m0}c_{m0}^2 + 8\mu_{m0}}\right]$$

and σ_T are the effective shear modulus and the yield point, respectively; and ρ_{m0}, c_{m0}, and μ_{m0} are the initial

Tomsk State Architecture and Building University, Tomsk, Russia
e-mail: svetl@niipmm.tsu.ru

1028-3358/02/4712-0876$22.00

values of the density, bulk velocity of sound, and shear modulus of the matrix material, respectively. The parameter λ is eliminated by using the Mises plasticity condition. The yield point of sandy ground is defined as in [3]:

$$\sigma_T = Y_1 + \frac{k_1 p}{1 + \frac{k_1 p}{Y_p - Y_0}},$$

where Y_1 is the cohesion, k_1 is the internal-friction coefficient, and Y_p is the limiting value of the shear strength.

The system of equations (1) is closed by the equation of state and the relationships describing the kinetics of the growth and coalescence of pores.

If the linear dependence of the shock-wave velocity D on the mass velocity u for the matrix material is known, the equation of state for a porous material has the form

$$p = \frac{\rho_{m0}}{\alpha}\left[\gamma_{m0}\varepsilon + \frac{c_{m0}^2(1-\gamma_{m0}\eta/2)\eta}{(1-S_{m0}\eta)^2}\right], \qquad (2)$$

where $\eta = 1 - \frac{\rho_{m0}v}{\alpha}$ and γ_{m0} is the Gruneisen coefficient of the matrix material. The coefficients c_{m0} and S_{m0} are determined in terms of the shock adiabatic of the mixture components $D_i = c_{0i} + S_{0i}u$ ($i = 2, 3$) by using the following relationships on the shock wave:

$$D = v_{m0}\sqrt{\frac{p_m}{v_{m0} - v_m(p_m)}}, \quad u = \sqrt{p_m(v_{m0} - v_m(p_m))},$$

$$v_m(p_m) = \sum_{i=2}^{3} m_i\left\{v_{0i} - \frac{1}{p_m}\left[\frac{c_{0i}}{S_{0i}}\left(\sqrt{\frac{p_m}{\rho_{0i}c_{0i}^2} + \frac{1}{4}} - \frac{1}{2}\right)\right]^2\right\},$$

where $m_2 = \frac{w_0}{1+w_0} = \frac{v_2\rho_{02}}{\rho_0}$ is the water mass concentration in the sandy ground (mass moisture) and $m_3 = \frac{1}{1+w_0} = \frac{v_3\rho_{03}}{\rho_0}$ is the quartz mass concentration in the ground ($m_2 + m_3 = 1$). The Gruneisen coefficient γ_{m0} is expressed in terms of the coefficients of the mixture components:

$$\gamma_{m0} = \frac{v_{m0}}{\frac{m_2}{\rho_{02}\gamma_{02}} + \frac{m_3}{\rho_{03}\gamma_{03}}}.$$

The equation that describes a change in porosity in the process of deforming sandy ground is derived by using model representations implying that the behavior of a medium with the initial porosity α_0 under dynamic loading is similar to the behavior of an individual spherical pore with the radius a_0 that is surrounded by a spherical shell of sandy ground, whose plastic properties satisfy the Mohr–Coulomb condition. The outer radius of the hollow sphere is taken so that the ratio of the entire volume of the sphere to the total volume of the matrix material is equal to the initial porosity α_0. Then, the solution to the problem of deforming a single pore under the action of isotropic stress provides the kinetic equation for calculating ground compaction [1]:

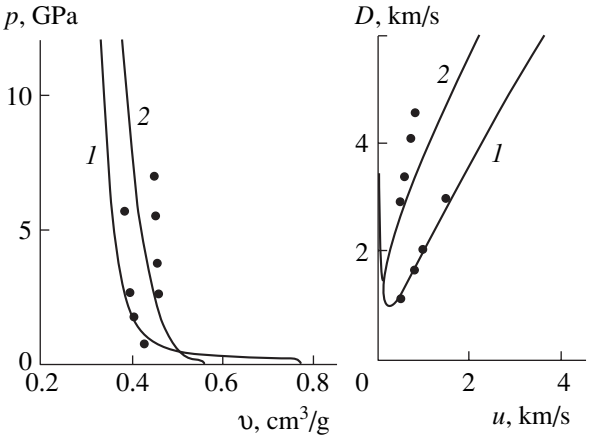

Fig. 1.

$$Y_0\tau^2 Q(\alpha, \dot\alpha, \ddot\alpha) = \alpha p + \frac{Y_0}{k}\left[1 - \left(\frac{\alpha}{\alpha - 1}\right)^{\frac{2k}{3-2k}}\right], \qquad (3)$$

where

$$\tau^2 = \frac{\rho_0 a_0^2}{3(\alpha_0 - 1)^{2/3} Y_0};$$

$$Q(\alpha, \dot\alpha, \ddot\alpha) = \frac{3-2k}{3+4k}\frac{\ddot\alpha}{\alpha^{1/3}}\left[1 - \left(\frac{\alpha}{\alpha-1}\right)^{\frac{3+4k}{3(3-2k)}}\right]$$

$$- \frac{3-2k}{3(6-k)}\frac{\dot\alpha^2}{\alpha^{4/3}}\left[1 - \left(\frac{\alpha}{\alpha-1}\right)^{\frac{2(6-k)}{3(3-2k)}}\right];$$

and Y_0 and k are the coefficients of the Mohr–Coulomb condition.

In the case of tension, sandy ground is described as a stress-free medium. Then, the relative content of pores is obtained from the equation of state for the

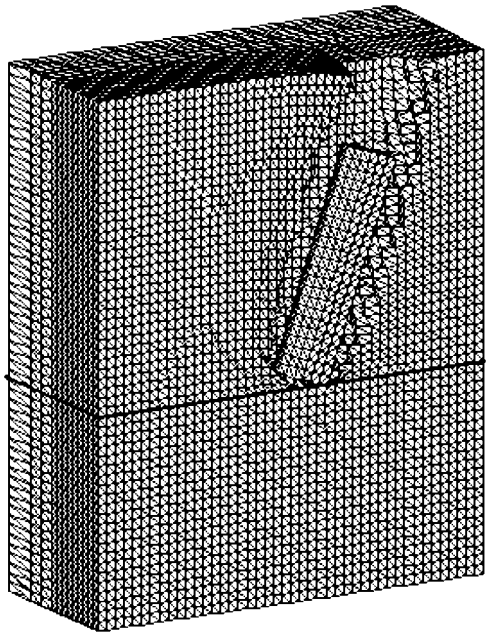

Fig. 2.

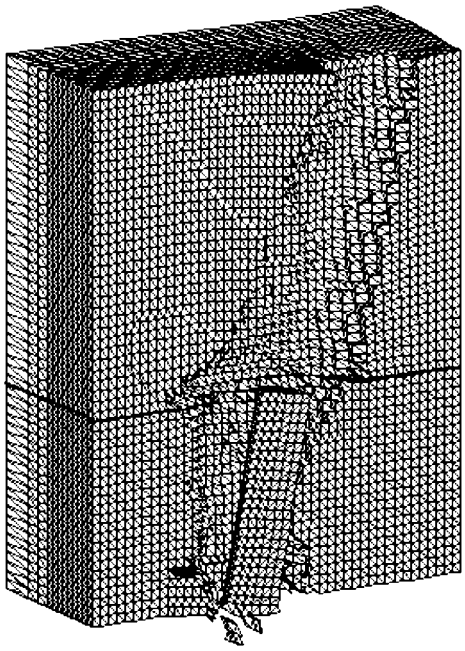

Fig. 3.

porous material with zero pressure between its particles.

Under the corresponding initial and boundary conditions, Eqs. (1)–(3) form a complete system of equations that describe the behavior of sandy ground under shock-wave loading.

The numerical values of Y_0 and k are determined by comparing the experimental and calculated shock adiabatics for sandy ground. Figure 1 shows the calculated shock adiabatic in variables (υ, p) and (u, D) for (curve *1*) dry and moist (curve *2*) sand. The experimental data [4] are shown by circles.

The parameters of the model of sandy ground composed of particles 0.07 mm in diameter are listed in the table.

Let us consider a problem formulated as follows. A cylindrical steel striker (diameter d_0 = 7.6 mm and length $l = 4d_0$) penetrates into a protective double-layer construction consisting of the upper $5.26d_0$-thick layer made of dry sandy ground and the lower concrete layer with a thickness of $3.68d_0$. The impact velocity is 420 m/s and the incidence angle is 20°. This problem was solved numerically by the modified finite-element method [5].

Figures 2 and 3 show the isometric projections of the striker and construction at 120 and 492 μs. When the striker passes through the sandy-ground layer, an inclined cylindrical cavity is formed in this layer. When the striker attains the sand–concrete interface (solid straight line), the decrease in its velocity is 26%. Next, the striker having a velocity of 310 m/s begins to penetrate into the concrete layer. During first 221 μs, the striker decelerates sharply. At this time, the concrete begins to fail. The crack reaches the rear side by the time of 300 μs. Then, the fragmentation of concrete occurs near the rear side, and pieces scatter and break down. The motion of the striker through the failed concrete is accompanied by a smaller decrease in its velocity and by a decrease in its angle to the normal of the obstacle. The total time of the penetration of the striker through the obstacle is equal to 492 μs, the residual velocity is equal to 29 m/s, and the output angle is equal to 12°. The head part of the striker is slightly deformed.

Table

ρ_0, g/cm^3	w_0, %	v_1, %	ρ_{m0}, g/cm^3	c_{m0}, cm/μs	S_{m0}	γ_{m0}	μ_{m0}, GPa	Y_0, GPa	k
1.29	0	51.5	1.95	0.368	2.12	1.0	0.073	0.1	0.75
1.8	28	7.75	1.95	0.245	1.86	1.28	0.073	0.025	0.5

ACKNOWLEDGMENTS

This work was supported by the Russian Foundation for Basic Research, project no. 01-01-00813.

REFERENCES

1. N. N. Belov, N. T. Yugov, S. A. Afanas'eva, *et al.*, Mekh. Kompoz. Mater. Konstr. **7** (2), 131 (2002).
2. F. F. Baum, L. P. Orlenko, K. P. Stanyukovich, *et al.*, *Physics of Explosion* (Nauka, Moscow, 1973).
3. B. V. Zamyshlyaev and L. S. Efterev, *Models of the Dynamic Deformation and Destruction of Ground Media* (Nauka, Moscow, 1990).
4. A. M. Bragov, N. N. Gerdyukov, A. G. Iolev, *et al.*, *Advanced Methods of Designing and Developing Rocket–Artillery Equipment* (VNIIÉF, Sarov, 2000), pp. 415–462.
5. N. T. Yugov, Izv. Akad. Nauk SSSR, Mekh. Tverd. Tela, No. 1, 112 (1990).

Translated by Yu. Vishnyakov

Doklady Physics, Vol. 47, No. 12, 2002, pp. 880–882. Translated from Doklady Akademii Nauk, Vol. 387, No. 5, 2002, pp. 627–629.

MECHANICS

Vibrations of a Cylinder in a Flow with a Free Surface

V. I. Bukreev

Presented by Academician V.M. Titov July 9, 2002

Received July 29, 2002

Flows around a cylinder in an unbounded fluid have been analyzed in numerous scientific studies. In particular, the effect of rotational vibrations of a cylinder on the hydrodynamic wake was experimentally investigated in a wind tunnel (see [1, 2]). Among several tens of papers devoted to the more complicated problem of flows around a cylinder placed near a free surface, it is worth noting the experimental studies described in [3–5], in which flows around an immobile cylinder were considered. In the present paper, certain experimental data related to the even more complicated problem on the interrelated motion of a free surface and a cylinder are given.

In an open channel of width $B = 6$ cm, a steady-state subcritical flow with a depth h_- and discharge Q was formed. Below, we use the quantity $U = \frac{q}{h_-}$ as a characteristic velocity scale, where $q = \frac{Q}{B}$ is the specific discharge. A horizontal circular cylinder made of organic glass with the external radius $R = 10$ mm was placed perpendicularly to the flow at a reasonably large distance from the channel entry, where the velocity profile was typical of the turbulent regime of motion. The cylinder had a hole with radius $R_1 = 2.5$ mm at its symmetry axis. This hole was penetrated by an immobile shaft with radius $r = 1.5$ mm. The shaft axis was situated at the height h above the channel bed. Owing to the difference between the radii of the hole and of the shaft, the cylinder had three degrees of freedom bounded in space. Experiments with an immobile cylinder were also performed.

In the fixed rectilinear coordinate system (x, y) whose origin is situated in the shaft center, the (x, y) axes are directed downstream and vertically upward, respectively, the shaft hole center having the coordinates (x_*, y_*).

Lavrent'ev Institute of Hydrodynamics,
Siberian Division, Russian Academy of Sciences,
pr. Akademika Lavrent'eva 15, Novosibirsk, 630090 Russia
e-mail:bukreev@hydro.nsk.ru

The character of the cylinder motion was recorded by video filming. It was found that, under the action of the flow, there was rolling motion of the surface of the cylinder hole over the immobile shaft. In this case, various cylinder points performed angular, longitudinal, and vertical vibrations. In particular, the point (x_*, y_*) vibrated along the segment of the trajectory whose equation can be written in parametric form as

$$x_* = (R_1 - r)\cos\varphi, \quad y_* = (R_1 - r)\sin\varphi,$$

where φ is the inclination angle to the x axis of the radius passing to the common tangent point of the hole surface and the shaft.

Below, we use independent dimensionless external parameters, namely, the quantities $\mathrm{Fr} = \frac{U}{\sqrt{2gR}}$, $\mathrm{Re} = \frac{2UR}{\nu}$, $h^0 = \frac{h}{R}$, $h_-^0 = \frac{h_-}{R}$, $R_1^0 = \frac{R_1}{R}$, and $\varepsilon = \frac{(R_1 - r)}{R}$ (q and ν are the acceleration of gravity and viscosity of the fluid, respectively). Below, the set of these parameters is denoted as Π_i. The basic desired function is the free-surface profile $\eta^0(x^0, \Pi_i)$. Here, η is the distance from the channel bed to the free surface and the subscript indicates the fact that the given quantity is normalized to R. Small particles of aluminum powder with a characteristic size of 10 μm were introduced into the flow. Trajectories of their motion yield information on the flow's internal structure. These trajectories were obtained by photography in a dark room with illumination by a narrow light knife of only the flow region of interest.

In the experiments under discussion, the parameter ε was small, while the angle φ varied with time t following the harmonic law $\varphi = \varphi_m \sin\omega t$, where $\varphi_m(\Pi_i)$ and $\omega(\Pi_i)$ are the amplitude and frequency of the vibrations. The amplitude varied within the limits $0 \le \varphi_m \le 1$ radian. Computer calculations and experimental results have shown that, for these values of φ_m for x_* and y_*, it is possible to accept

$$x_*^0 \approx \alpha\cos(2\omega t) + b, \quad y_*^0 \approx c\sin\omega t,$$

where $a(\Pi_i)$, $b(\Pi_i)$, and $c(\Pi_i)$ are oscillation parameters. These formulas show that horizontal vibrations of

1028-3358/02/4712-0880$22.00

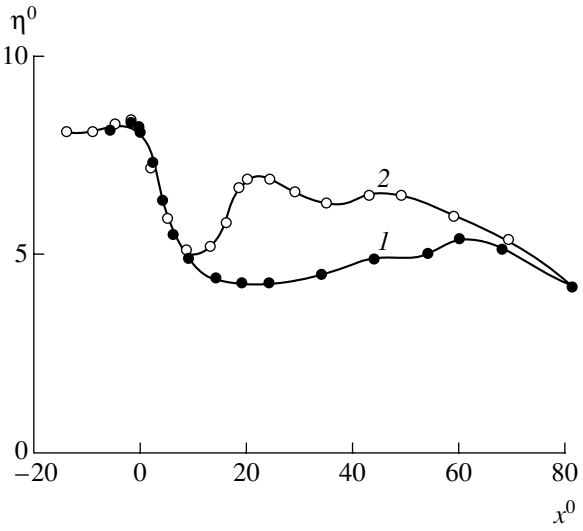

Fig. 1. Profile of the free surface (*1*) in the absence of vibrations and (*2*) in the presence of vibrations. R = 1 cm; U = 45.3 cm s^{-1}; Fr = 1.022; Re = 9060; h_-^0 = 8.3; h^0 = 4.2; R_1^0 = 0.25; ε = 0.1; St = 2.16; c = 0.055.

the cylinder occur with doubled frequency and with a constant frequency shift with respect to the vertical vibrations. For $\varphi_m < 1$, the vibration parameters are related to each other by the relationships

$$\varphi_m = \frac{c}{\varepsilon}, \quad a = \varepsilon - \frac{c^2}{4\varepsilon}, \quad b = \frac{c^2}{4\varepsilon}.$$

In our experiments, the inequality $c < \varepsilon$ was valid; therefore, the amplitude of vertical vibrations of the cylinder considerably exceeded that of horizontal vibrations.

The most interesting experimental result is that the small vibrations of the cylinder, which were caused by the fluid flow, are capable of strongly changing both the wave pattern beyond the cylinder and the flow in the hydrodynamic wake. Examples illustrating this effect are presented in Figs. 1 and 2.

In Fig. 1, profiles of the free surface beyond the immobile and vibrating cylinders are compared. Beyond the immobile cylinder, the profile has the shape of a long and smooth wave. In this case, small vibrations of the cylinder led to the production of an undular

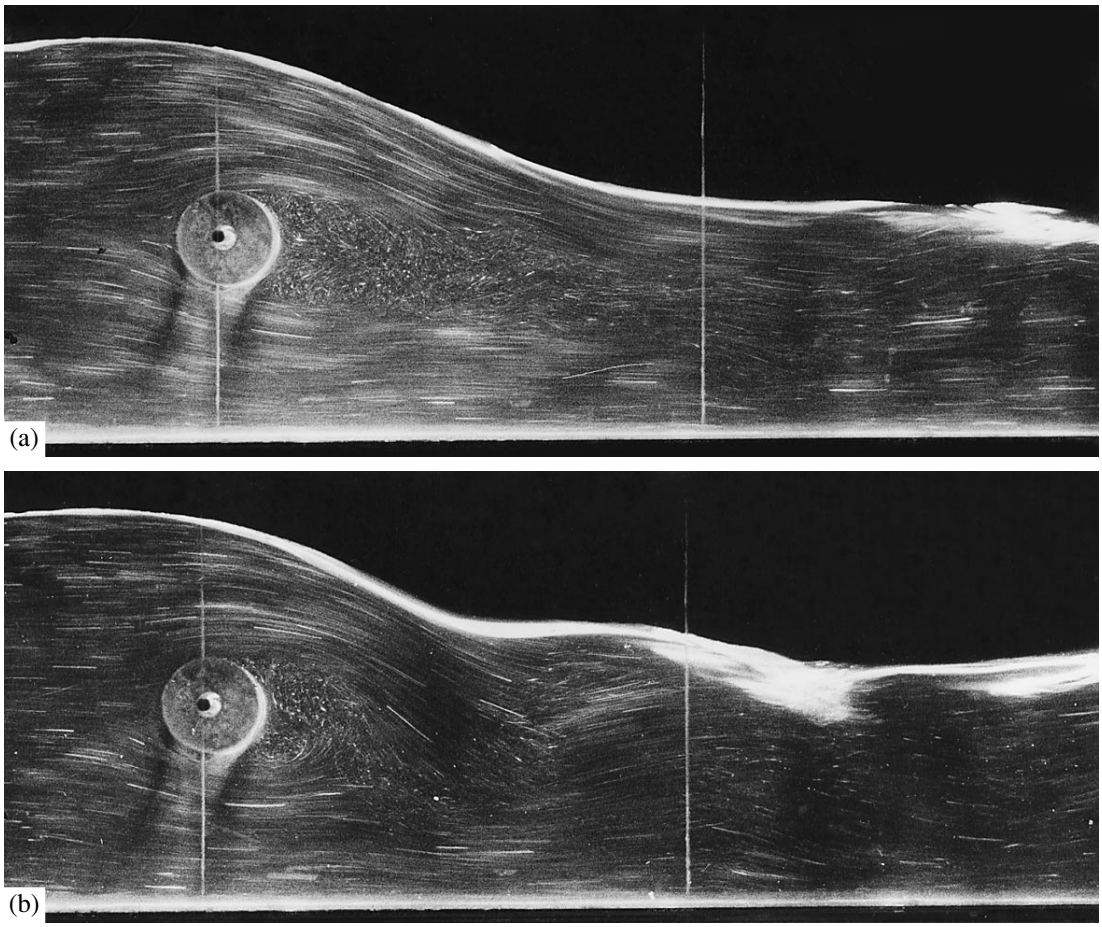

Fig. 2. Pattern of a flow around the cylinder (a) in the absence of vibrations and (b) in the presence of vibrations. Values of the parameters are the same as in Fig. 1. The distances between vertical white reference lines are 10 cm.

hydraulic jump with a breaking leading part. In the cross section $x^0 = 23$, the flow depth beyond the vibrating cylinder exceeded that beyond the immobile cylinder by a factor of 1.6. The vibrations of the cylinder were accompanied by an increase in the energy loss of the fluid.

Figure 2 illustrates an effect of vibrations of the cylinder on the flow's internal structure. Beyond the immobile cylinder (Fig. 2a), a separation region being transformed into a narrow twisting hydrodynamic wake appeared. This pattern is analogous to that observed in an unbounded flow with the corresponding values of the Reynolds number Re. When vibrations of the cylinder (Fig. 2b) did exist, the separation region beyond it was considerably reduced, and the hydrodynamic wake turned out to be strongly distorted by a concentrated jet that penetrated the wake from either above or below synchronously with vertical vibrations of the cylinder.

The vibrations of the cylinder were accompanied in its vicinity by oscillations of the free surface at the same frequency ω. The phase difference of these oscillations depended on values of the parameters Π_i. In the examples given in Figs. 1 and 2, the cylinder and the free surface oscillated in antiphase. For larger values of q, the oscillations occur with equal phase.

From the quantitative information obtained as a result of the described experiments, it follows that there exists a subregion of the phase space for the parameters Π_i in which the dimensionless parameter $\mathrm{St} = \omega\sqrt{\frac{2R}{g}}$ has a constant value equal to 2.16.

ACKNOWLEDGMENTS

The author is grateful to V.A. Kostomakha and A.V. Gusev for their help in performing the experiments.

This work was supported by the Russian Foundation for Basic Research, project no. 01-01-00846, in the framework of the Program "Leading Scientific Schools" of the Russian Federation, project no. 00-05-98542, and of the Integration Program, project 2000-1 of the Siberian Division, Russian Academy of Sciences.

REFERENCES

1. N. Fujisava, K. Ikemoto, and K. Nagaya, J. Fluids and Struct. **12** (8), 1041 (1998).
2. T. Lee, AIAA J. **37** (3), 328 (1999).
3. I. S. Dolina, S. A. Ermakov, and E. N. Pelinovskiĭ, Prikl. Matem. Teoret. Fiz. **29** (4), 48 (1988).
4. J. Sheridan, C. C. Lin, and D. Rockwell, J. Fluid Mech. **330**, 1 (1997).
5. J. W. Hoyt and R. H. J. Sellin, Exp. Fluids **28** (3), 261 (2000).

Translated by G. Merzon

Doklady Physics, Vol. 47, No. 12, 2002, pp. 883–887. Translated from Doklady Akademii Nauk, Vol. 387, No. 5, 2002, pp. 630–634.

MECHANICS

On Analytical Theory of Turbulent Channel Flows: Determination of Turbulence Constants

A. S. Pleshanov

Presented by Academician G.S. Golitsyn August 12, 2002

Received August 14, 2002

We consider the problem of the determination of turbulence constants for a steady-state stabilized axisymmetric turbulent channel flow of incompressible fluid in an isothermal regime. In order to allow for a difference in the pulsation damping of the longitudinal and transverse velocity components of such a flow near the channel walls, we introduce two mixing lengths. These lengths are approximated by power expansions of the second and third orders in the radial coordinate. On imposing boundary conditions, the number of unknown coefficients is reduced to only two, namely, to the conventional Karmán constant and a certain new constant. Therefore, with allowance for the integration constant in the mean-velocity profile, there are three independent turbulence constants. It is shown that in the case of the given Karmán constant (its theoretical estimations are well known), the remaining parameters can also be calculated. The solution to the problem is based on a power expansion (divergent almost everywhere) of the velocity, which is of the ninth order in the coordinate. The expansion is reduced to a convergent form by a logarithmic transformation.

The semiempirical character of present-day theories describing turbulent channel flows is determined by the use of experimental values of constants entering into these theories. There exists a standpoint (see, e.g., [1]) that these constants cannot be evaluated theoretically. However, the appearance of papers devoted to the theoretical determination of one of these constants (the so-called Karmán universal constant $\kappa = 0.4$) casts doubt on this opinion. We now mention seemingly the most fundamental publication [2], in which the value $\kappa = 0.372$ was found. This result was obtained within the framework of the renormalization approach borrowed from quantum field theory. In the present paper, using a purely hydrodynamic approach, we evaluate the remaining constants, in particular, a new constant allowing for a difference in the pulsation damping of the longitudinal and transverse velocity components.

Krzhizhanovskiĭ Power Engineering Institute, Leninskiĭ pr. 19, Moscow, 117927 Russia

1. Steady-state stabilized axisymmetric flows of an incompressible fluid in an isothermal regime are described by the well-known set of averaged hydrodynamical equations involving the continuity equation and two equations of motion:

$$(r^n\bar{u})_z = 0, \tag{1}$$

$$\frac{r^n\bar{p}_z}{\rho} = [r^n(\bar{\tau}_l + \bar{\tau}_t)]_r, \tag{2}$$

$$\bar{p}_r = 0. \tag{3}$$

Here, $\bar{\tau}_l = \nu\bar{u}_r < 0$ and $\bar{\tau}_t = -\overline{u'v'} < 0$ are the laminar and turbulent shear stresses, respectively (their signs correspond to the case of a centrally symmetric flow); the subscripts z and r stand for the derivatives with respect to the coordinates; the linear and cylindrical cases correspond to $n = 0$ and 1, respectively; and the remaining denotations are conventional. The stabilization condition (with respect to z coordinates) implies that the quantities $\bar{u}$, $\bar{\tau}_l$, and $\bar{\tau}_t$ depend only on r with $\bar{v} = 0$. With regard to Eq. (2), the condition $\bar{p} = \bar{p}(z)$ issuing from (3) yields $\bar{p}_z = \text{const}$. As a result, we arrive at one-dimensional equation (2) and the integral of Eq. (1), which is the constant-flow-rate condition

$$G = \int_0^a \bar{u}r^n dr = \text{const}, \tag{4}$$

where a is the channel radius.

The boundary conditions are formed by the conditions at the channel wall

$$\bar{u}(a) = 0, \tag{5}$$

$$u'(a) = v'(a) = 0 \tag{6}$$

and by the symmetry condition

$$\bar{u}_r(a) = 0. \tag{7}$$

From the continuity equation

$$(r^n u')_z + (r^n v')_r = 0,$$

1028-3358/02/4712-0883$22.00

it follows by virtue of (6) for pulsations at the wall (see, e.g., [3]) that

$$v_r'(a) = 0. \quad (8)$$

Hence, in addition to the equality

$$\bar{\tau}_t(a) = (\bar{\tau}_t)_r(a) = 0, \quad (9)$$

we arrive at

$$(\bar{\tau}_t)_{rr}(a) = 0. \quad (10)$$

In the simplest case, the relation of $\bar{\tau}_t$ to averaged flow characteristics can be found on the basis of the Prandtl kinetic analogy (see, e.g., [4]):

$$|u'| \sim |v'| \sim l|\bar{u}_y|. \quad (11)$$

Here, $l(y)$ is the mixing path length (an analogue of the mean free path). Hence,

$$\bar{\tau}_t = -\overline{u'v'} = l^2|\bar{u}_y|\bar{u}_y = \operatorname{sgn}\bar{u}_y(l\bar{u}_y)^2, \quad (12)$$

where $y = a - r$ is the distance to the channel wall. In fact, in view of both Eq. (8) and the condition $u_r'(a) \neq 0$, the mixing path lengths for u' and v' differ slightly. Namely,

$$|u'| \sim l_1|\bar{u}_y|, \quad |v'| \sim l_2|\bar{u}_y|, \quad (13)$$

where $l_1 \sim y$ and $l_2 \sim y^2$, or, more exactly,

$$l_1 = yf_1(\zeta) \text{ and } l_2 = \frac{y^2}{a}f_2(\zeta).$$

Here, $\zeta = \frac{y}{a}$ and the unknown functions $f_{1,2}$ are approximated by the expansions into a power series

$$f_1 = \sum_{i=0}^{k} a_{1i}\zeta^i, \quad f_2 = \sum_{j=0}^{k} a_{2j}\zeta^j.$$

Hence,

$$\bar{\tau}_t = \operatorname{sgn}\bar{u}_y\frac{y^3}{a}f_1f_2\bar{u}_y^2. \quad (14)$$

The similar representation in the case of (11) takes the form

$$\bar{\tau}_t = \operatorname{sgn}\bar{u}_y(yf_1\bar{u}_y)^2. \quad (15)$$

With regard to (7), the integral in Eq. (2) has the form

$$l_1l_2\bar{u}_r^2 - \nu\bar{u}_r + \frac{\bar{p}_z}{\rho}\frac{r}{n+1} = 0.$$

Introducing the dynamic velocity

$$v_* = \left(-\frac{1}{n+1}\frac{\bar{p}_z}{\rho}a\right)^{1/2} = \left(\frac{1}{n+1}\frac{\Delta p}{L}\frac{a}{\rho}\right)^{1/2}$$

and the dimensionless quantities $\psi = \frac{\bar{u}}{v_*}$ and $\xi = \frac{r}{a}$, we arrive at the equation

$$\Lambda_1\Lambda_2\psi_\xi^2 - \Delta\psi_\xi - \xi = 0, \quad (16)$$

where $\Lambda_{1,2} = \frac{l_{1,2}}{a}$, $\Delta = \frac{\nu}{v_*a} \equiv \frac{1}{R}$. Relation (16) expressed in terms of the variable ζ takes the form

$$R\Lambda_1\Lambda_2\psi_\zeta^2 + \psi_\zeta - R(1-\zeta) = 0. \quad (17)$$

Hence,

$$\psi_\zeta = -\psi_\xi = \frac{2\xi}{\Delta + \sqrt{\Delta^2 + 4\Lambda_1\Lambda_2\xi}} = \frac{2R\xi}{1 + \sqrt{1 + 4R^2\Lambda_1\Lambda_2\xi}}. \quad (18)$$

In the case

$$[4R^2(\Lambda_1\Lambda_2)_0]^{-1} \ll \xi \ll 1,$$

we obtain from Eq. (18) the Darcy integral [4]

$$\psi(0) - \psi(\xi) = \frac{U - \bar{u}}{v_*} = \frac{2}{3}\frac{\xi^{3/2}}{\sqrt{(\Lambda_1\Lambda_2)_0}}.$$

In our further consideration, the quantities $\Lambda_{1,2}$ should be defined more concretely.

Considering only the simplest case, we set

$$\Lambda_1 = a_{10}\zeta + a_{11}\zeta^2 \text{ and } \Lambda_2 = a_{20}\zeta^2 + a_{21}\zeta^3.$$

Assuming that

$$\Lambda_{1\zeta}(1) = \Lambda_{2\zeta}(1) = 0,$$

we have

$$\Lambda_1 = a_{10}\zeta\left(1 - \frac{1}{2}\zeta\right), \quad \Lambda_2 = a_{20}\zeta^2\left(1 - \frac{2}{3}\zeta\right),$$

$$\Lambda_{1\zeta} = a_{10}(1-\zeta), \quad \Lambda_{2\zeta} = 2a_{20}\zeta(1-\zeta);$$

$$\Lambda_1\Lambda_2 = a_{10}a_{20}\zeta^3\left(1 - \frac{7}{6}\zeta + \frac{1}{3}\zeta^2\right).$$

The quantities $\bar{\Lambda}_1 = \frac{\Lambda_1}{\Lambda_1(1)}$ and $\bar{\Lambda}_2 = \frac{\Lambda_2}{\Lambda_2(1)}$, as well as their product, are shown in Fig. 1. It follows from the equalities $\Lambda_{2\zeta}(\zeta) = \Lambda_{2\zeta}(1-\zeta)$ that $\bar{\Lambda}_2 - \frac{1}{2}$ is an odd function of $\zeta - \frac{1}{2}$.

The constant $a_{10} \equiv \kappa$ is the Karmán constant mentioned above, while a_{20} is a new turbulence constant. In this approximation, the product $a_{10}a_{20} = \alpha_0$ is the only

indefinite constant entering into Eqs. (16) and (17). Furthermore, we determine the constant a_{20} and the second turbulence constant κ_0 entering into the expression

$$\psi(\zeta) = \frac{\bar{u}}{v_*} = \kappa_1 \ln(R\zeta) + \kappa_0 \qquad (19)$$

with only κ given and $\kappa_1 = \frac{1}{\kappa}$ [4].

2. The theory presented below is analytical in the literal sense of this definition, because we seek solutions to nonlinear equation (17) as power expansions. In this case, the general solution can be found by a regular method resulting in recurrence relations.

We assume that

$$\Lambda_1 = \zeta \sum_{i=0}^{\infty} a_{1i}\zeta^i, \quad \Lambda_2 = \zeta^2 \sum_{j=0}^{\infty} a_{2j}\zeta^j,$$

$$\psi_\zeta = \sum_{l=0}^{\infty} b_l \zeta^l.$$

The problem is reduced to expressing the coefficients b_l that enter into Eq. (17) in terms of a_{1i} and a_{2j}.

It is evident that

$$\Lambda_1\Lambda_2 = \zeta^3 \sum_{i,j} a_{1i}a_{2j}\zeta^{i+j} = \zeta^3 \sum_{k=0}^{\infty} \alpha_k \zeta^k,$$

$$\psi_\zeta^2 = \sum_{l,m} b_l b_m \zeta^{l+m} = \sum_{n=0}^{\infty} \beta_n \zeta^n,$$

where

$$\alpha_k = \sum_{i=0}^{k} a_{1i}a_{2,k-i} \text{ and } \beta_n = \sum_{l=0}^{n} b_l b_{n-l}.$$

Then,

$$\Lambda_1\Lambda_2\psi_\zeta^2 = \zeta^3 \sum_{k,n} \alpha_k\beta_n\zeta^{k+n} = \zeta^3 \sum_{p=0}^{\infty} c_p\zeta^p,$$

where

$$c_p = \sum_{k=0}^{p} \alpha_k \beta_{p-k}.$$

And lastly,

$$\psi_\zeta = (b_0 + b_1\zeta) + b_2\zeta^2 + \zeta^3 \sum_{p=0}^{\infty} b_{p+3}\zeta^p.$$

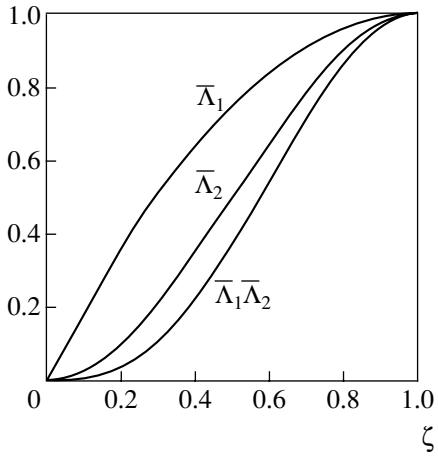

Fig. 1.

The substitution of these expansions into Eq. (17) yields

$$b_0 = R, \quad b_1 = -R, \quad b_2 = 0,$$
$$b_{p+3} = -Rc_p.$$

The equality $b_2 = 0$ is mentioned in [3]. As a result, substituting $d_1 > 0$ for b_1, we have

$$\psi_\zeta = (d_0 - d_1\zeta + d_2\zeta^2) + (-d_3\zeta^3 + d_4\zeta^4 - d_5\zeta^5)$$
$$+ (d_6\zeta^6 - d_7\zeta^7 + d_8\zeta^8) + \ldots \equiv (e_0 - e_1\zeta + e_2\zeta^2)R$$
$$+ (-e_3\zeta^3 + e_4\zeta^4 - e_5\zeta^5)\alpha_0 R^3$$
$$+ (e_6\zeta^6 - e_7\zeta^7 + e_8\zeta^8)\alpha_0^2 R^5 + \ldots, \qquad (20)$$

where

$$e_0 = 1, \quad e_3 = 1, \quad e_6 = 2,$$
$$e_1 = 1, \quad e_4 = \frac{19}{6}, \quad e_7 = \frac{32}{3}, \qquad (21)$$
$$e_2 = 0, \quad e_5 = \frac{11}{3}, \quad e_8 = \frac{443}{18}.$$

Finally, in view of condition (5), we obtain

$$\psi = \left(d_0\zeta - \frac{d_1\zeta^2}{2} + 0\right) + \left(-\frac{d_3\zeta^4}{4} + \frac{d_4\zeta^5}{5} - \frac{d_5\zeta^6}{6}\right)$$
$$+ \left(\frac{d_6\zeta^7}{7} - \frac{d_7\zeta^8}{8} + \frac{d_8\zeta^9}{9}\right) + \ldots. \qquad (22)$$

It is worth noting that, if we expand representation (18) in powers of the parameter $4R^2\Lambda_1\Lambda_2\xi$ (i.e., of $\alpha_0 R^2$) rather than initial equation (17) in powers of the argument ζ, the group of expansion terms in (20) with the common factor $\alpha_0 R^3$ will include additional terms $e_6'\zeta^6$ and $e_7'\zeta^7$. The expansion in ζ taken above yields these terms in the group of terms with the common factor

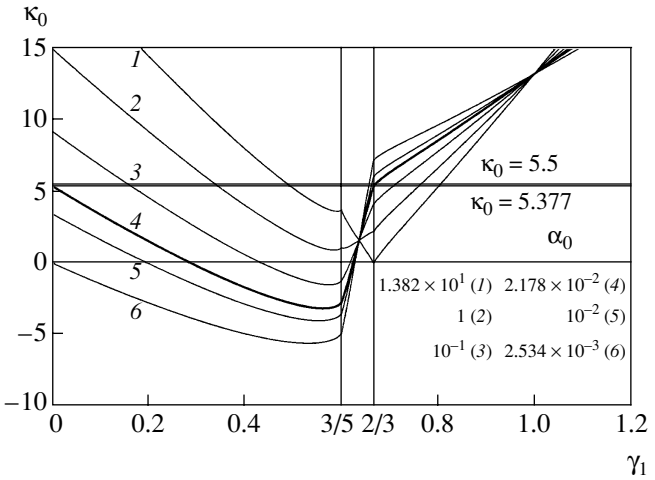

Fig. 2.

$\alpha_0^2 R^5$. Naturally, these terms can be omitted as the lowest in powers of R. A similar remark holds true for the group of terms with the factor $\alpha_0^2 R^5$, etc.

In what follows, we consider an asymptotic regime, i.e., the case of sufficiently large values of Reynolds number

$$\mathrm{Re} = \frac{\langle u\rangle d}{\nu} = R\frac{\langle u\rangle}{v_*}\frac{d}{a}.$$

Here, the parameter R is assumed to be sufficiently large, $\langle u\rangle$ and $d = \frac{4a}{n+1}$ being the mean velocity and the hydraulic diameter, respectively.

We can reduce strongly divergent expansion (22) to a convergent form in the following manner. According to Eq. (18), the function ψ_ζ tends to a finite limit as $R \longrightarrow \infty$ in the central region, whereas it turns out to be a weak (logarithmic) function of R in the intermediate domain between the central and near-wall regions. This is seen, in particular, from expression (19). Because of this, each term of expansion (22) can be approximately considered as the first term of an expansion of the corresponding logarithmic function with a certain correction factor that disappears in the expansion in the vicinity of the viscous sublayer. Namely, we make the replacements

$$d_{2k}\frac{\zeta^{2k+1}}{2k+1} \to |g_{2k}|\ln\left(1 + \frac{d_{2k}}{|g_{2k}|}\frac{\zeta^{2k+1}}{2k+1}\right),$$

$$-d_{2k-1}\frac{\zeta^{2k}}{2k} \to -|g_{2k-1}|\ln\left(1 + \frac{d_{2k-1}}{|g_{2k-1}|}\frac{\zeta^{2k}}{2k}\right).$$

Here, we introduce the moduli of the multipliers in order to provide for the arguments of the logarithmic functions to be positive. To diminish the number of the multipliers, it is natural to take them as identical for all terms of the same power in R, so that

$$\psi \longrightarrow \omega = g_1\left[\ln\left(1 + \frac{e_0}{g_1}R\zeta\right) - \ln\left(1 + \frac{e_1}{g_1}R\frac{\zeta^2}{2}\right) + 0\right]$$
$$+ |g_3|\left[-\ln\left(1 + \frac{e_3}{|g_3|}\alpha_0 R^3\frac{\zeta^4}{4}\right) + \ln\left(1 + \frac{e_4}{|g_3|}\alpha_0 R^3\frac{\zeta^5}{5}\right)\right.$$
$$\left. - \ln\left(1 + \frac{e_5}{|g_3|}\alpha_0 R^3\frac{\zeta^6}{6}\right)\right] + |g_5|\left[\ln\left(1 + \frac{e_6}{|g_5|}\alpha_0^2 R^5\frac{\zeta^7}{7}\right)\right.$$
$$\left. - \ln\left(1 + \frac{e_7}{|g_5|}\alpha_0^2 R^5\frac{\zeta^8}{8}\right) + \ln\left(1 + \frac{e_8}{|g_5|}\alpha_0^2 R^5\frac{\zeta^9}{9}\right)\right] + \ldots, \quad (23)$$

where $g_1 > 0$. For sufficiently small ζ, representation (23) tends to expansion (22) and is reduced to a convergent expression outside the viscous sublayer when the unity in the arguments of the logarithmic functions can be omitted.

Comparing the factors standing at $\ln\zeta$ and $\ln R$ in expressions (19) and (23) for sufficiently small g_1 when $g_{3,5} > 0$ (see below), we obtain the set of equations with respect to $\gamma_{2k-1} = \frac{g_{2k-1}}{\kappa_1}$

$$-5\gamma_3 + 8\gamma_5 = 1 + \gamma_1, \quad -3\gamma_3 + 5\gamma_5 = 1.$$

This set has the solution

$$\gamma_3 = 3 - 5\gamma_1, \quad \gamma_5 = 2 - 3\gamma_1.$$

For $\gamma_1 > \frac{3}{5}$ and $\gamma_1 > \frac{2}{3}$, we have $|\gamma_3| = |3 - 5\gamma_1|$ and $|\gamma_5| = |2 - 3\gamma_1|$, respectively. In addition, we obtain the following dependence of κ_0 on γ_1, with the parameters κ and α_0 given:

$$\kappa_0 = g_1\left[\ln e_0 - \ln\left(\frac{e_1}{2}\right) + 0\right]$$
$$+ |g_3|\left[-\ln\left(\frac{e_3}{4}\right) + \ln\left(\frac{e_4}{5}\right) - \ln\left(\frac{e_5\alpha_0}{6|g_3|}\right)\right]$$
$$+ |g_5|\left[\ln\left(\frac{e_6}{7}\right) - \ln\left(\frac{e_7}{8}\right) + \ln\left(\frac{e_8\alpha_0^2}{9|g_5|}\right)\right]. \quad (24)$$

For γ_1 satisfying the condition

$$|\gamma_3| = 2|\gamma_5|,$$

i.e., for $\gamma_1 = \frac{7}{11}$ or $\gamma_1 = 1$, the quantity κ_0 is independent of α_0. The dependence under consideration is shown in Fig. 2 for six values of α_0, with $\kappa = 0.4$. The discontinuities at $\gamma_1 = \frac{3}{5}$ and $\gamma_1 = \frac{2}{3}$ (when $\gamma_3 = 0$ and $\gamma_5 = 0$) are caused by the presence in the last expression of the

moduli of γ_3 and γ_5, respectively. By virtue of physically evident condition $\kappa_0 > 0$, the interval of admissible values of α_0 is bounded by the inequalities $2.534 \times 10^{-3} < \alpha_0 < 1.382 \times 10^{1}$ as is seen from Fig. 2. Within this interval of values of α_0 at $\gamma_1 = 0$, the inequalities $\kappa_0 > 0$ and $\frac{d\kappa_0}{d\gamma_1} < 0$ take place. At the same time for $\gamma_1 \geq \frac{2}{3}$, $\frac{d\kappa_0}{d\gamma_1} > 0$. As a result, for admissible α_0 within the interval $\gamma_1 \in (0, \gamma_{1*})$ such that

$$\kappa_{0*}(\gamma_1 = 0; \alpha_0) = \kappa_{0*}(\gamma_{1*}; \alpha_0) \qquad (25)$$

the value $\kappa_0 < \kappa_{0*}$ is realized doubly while for $\kappa_0 > \kappa_{0*}$—only once. In other words, from the domains 1, 2, and 3 in which, respectively, $\gamma_1 \in \left(0, \frac{3}{5}\right)$, $\left(\frac{3}{5}, \frac{2}{3}\right)$, and $\left(\frac{2}{3}, \infty\right)$, as follows from Eq. (25), only in the domain 3, the dependence $\kappa_0(\gamma_1, \alpha_0 = \text{const})$ for admissible α_0 is monotonically increasing. For $\kappa_0 < \kappa_{0*}$, this fact ensures the uniqueness of κ_0. In this domain, for admissible α_0 the minimum value of γ_{1*} is equal to 2/3, with $\alpha_{0*} = 0.02178$ and $\kappa_{0*} = 5.377$. The latter value differs from the experimental result $\kappa_0 = 5.5$ [4] only by about 2%, which is probably smaller than the experimental error. In any case, the calculated and experimental [4] reduced velocity profiles $\frac{\bar{u}(y)}{\bar{u}(a)}$ in the case of $\mathrm{Re} = 4.0 \times 10^3$, 1.1×10^5, and 3.0×10^6 are visually indistinguishable.

The new turbulence constant is

$$\alpha_{20} = \kappa_1 \alpha_{0*} = 0.05445. \qquad (26)$$

The turbulence constant κ'_{0*}, which is similar to κ_{0*} entering into the expression for the average velocity

$$\langle \psi \rangle \longrightarrow \langle \omega \rangle = \langle \bar{u} \rangle / v_* = \kappa_1 \ln R + \kappa'_{0*}, \qquad (27)$$

is given by the conventional formula

$$\kappa'_{0*} = \kappa_{0*} + (n+1)\kappa_1 \int_0^1 \ln \zeta \xi^n d\xi .$$

Hence, $\kappa'_{0*}(n = 1) = 1.627$ (instead of the experimental value $\kappa_{0*} = 1.75$) and $\kappa'_{0*}(n = 0) = 2.877$. Allowing for the channel-resistance coefficient λ, we can easily pass from Eq. (27) to the universal resistance law [4].

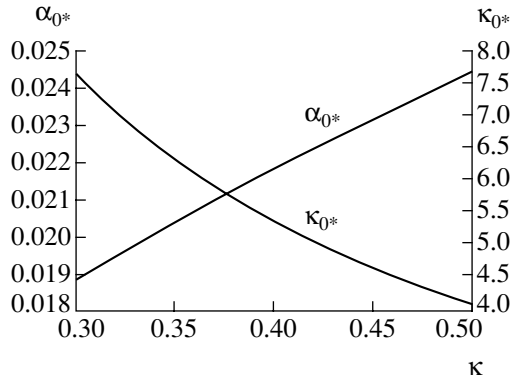

Fig. 3.

In view of a certain spread of values of the Karmán constant κ, we present in Fig. 3 the dependences $\alpha_{0*}(\kappa)$ and $\kappa_{0*}(\kappa)$, which are described analytically by the expressions

$$\ln \alpha_{0*} - \frac{1}{2}\ln \kappa = \ln a_{20} + \frac{1}{2}\ln \kappa = -3.368,$$
$$\kappa \kappa_{0*} + \frac{1}{2}\ln \kappa = 1.693. \qquad (28)$$

Thus, any of the four quantities $a_{10} = \kappa$, a_{20}, κ_{0*}, and κ'_{0*} can be determined provided that one of them is given.

ACKNOWLEDGMENTS

The author is grateful to I.M. Mazilin, who has performed numerous preliminary and final calculations (the results of the latter ones are presented here).

REFERENCES

1. L. D. Landau and E. M. Lifshitz, *Course of Theoretical Physics*, Vol. 6: *Fluid Mechanics* (Nauka, Moscow, 1986; Pergamon, New York, 1987).
2. V. Jakhot and S. A. Orszag, J. Sci. Comput. **1** (1), 3 (1986).
3. A. S. Monin and A. M. Yaglom, *Statistical Fluid Mechanics* (Nauka, Moscow, 1965; MIT Press, Cambridge, Mass., 1971), Vol. 1.
4. H. Schlichting, *Boundary Layer Theory* (McGraw-Hill, New York, 1968; Nauka, Moscow, 1969).

Translated by V. Chechin

Doklady Physics, Vol. 47, No. 12, 2002, pp. 888–891. Translated from Doklady Akademii Nauk, Vol. 387, No. 6, 2002, pp. 760–763.

MECHANICS

Invariant Properties of the Equations of Motion of Stratified Fluids

V. G. Baĭdulov* and Yu. D. Chashechkin**

Presented by Academician D.M. Klimov June 25, 2002

Received June 25, 2002

Along with the equations of motion of multicomponent stratified fluids [1], various model systems [2] are extensively used to describe physical processes in the environment. These models include derivative models based on simplifications of the original system [3] and constitutive models, among which turbulence theories are most extensively used [4, 5]. In order to construct adequate and efficient models and to estimate the consistency of various approaches, continuous group theory is extensively used [6], and invariant properties of compared sets of nonlinear equations are calculated and compared. The development of the technique of symbolic computer calculations makes it possible to apply Lee-group-theory methods [7] to complex sets of the general equations of motion [8, 9]. In this study, we compare the invariant properties of the basic sets of equations used to calculate flows of multicomponent stratified media, which simulate processes in the atmosphere and hydrosphere. Point-symmetry groups were sought by the software package developed in the Maple language [10].

The basic set of equations of motion of a multicomponent stratified fluid has the form [1, 2]

$$\rho(\mathbf{S})\left(\frac{\partial \mathbf{u}}{\partial t} + (\mathbf{u}\nabla)\mathbf{u}\right) = -\nabla P + \nabla(\mu(\mathbf{S})\nabla\mathbf{u}) + \rho(\mathbf{S})\mathbf{g},$$
$$\frac{\partial S_i}{\partial t} + (\mathbf{u}\nabla)S_i = \nabla(\kappa_i(\mathbf{S})\nabla S_i), \quad (1)$$
$$\mathrm{div}\mathbf{u} = 0.$$

Here, $\mathbf{u} = (u, v, w)$, P, and ρ are the velocity, pressure, and density of the fluid, respectively; g is the acceleration of gravity; $\nu = \frac{\mu}{\rho}$ is the kinematic viscosity, where μ is the dynamic viscosity; and κ_i are kinetic coefficients, which are the characteristics of the molecular transport and depend on all the parameters determining the density of the medium. The equation of motion relating the medium density $\rho = \rho(\mathbf{S})$ to the temperature and concentration of dissolved or suspended particles and gases involves an additional set of parameters. These parameters—the thermal expansion coefficient, salt compressibility factor, etc.—which are generally nonlinear, are not presented in explicit form. Practical problems are often solved in the Boussinesq approximation, where density variations are taken into account only in the term that presents the buoyancy forces and involves a large factor **g**.

The generators of the basic infinite-dimensional symmetry group of complete set (1) present the basic properties of classical mechanics and can be represented in the form (physical interpretation of the corresponding transformation group is given in parentheses)

$$X_1 = \partial_t, \quad X_{2\ldots4} = \partial_{x_i}$$

(spatial and time translations);

$$X_{5\ldots7} = t\partial_{x_i} + \partial_{u_i}$$

(Galilean relativity);

$$X_8 = y\partial_x - x\partial_y + v\partial_u - u\partial_v \quad (2)$$

(rotations in the horizontal plane);

$$X_{9,10} = \left(\frac{gt^2}{2} + z\right)\partial_{x_i} - x_i\partial_z + (gt + w)\partial_{u_i} - u_i\partial_w$$

(rotations in the vertical plane in a noninertial reference frame moving with the acceleration of gravity);

infinite-dimensional subalgebra

$$X_\pi = \pi(t)\partial_P \text{ (pressure translations),}$$

where $\pi(t)$ is an arbitrary function of time.

The Boussinesq approximation substantially changes the basic symmetry group, whose set of generators in this case involve both some operators common with algebra (2) and three new operators:

Institute for Problems in Mechanics,
Russian Academy of Sciences,
pr. Vernadskogo 101, Moscow, 117526 Russia
** e-mail: bayd@ipmnet.ru*
*** e-mail: chakin@ipmnet.ru*

1028-3358/02/4712-0888$22.00

$X_1 = \partial_t$ (time translations);

$$X_2 = y\partial_x - x\partial_y + v\partial_u - u\partial_v$$

(rotations in the horizontal plane);

and the infinite-dimensional subalgebras

$$X_\pi = \pi(t)\partial_P \text{ (pressure translations);}$$
$$X_{\chi_i} = \chi_i(t)\partial_{x_i} + \chi_i'(t)\partial_{u_i} - \chi_i''(t)x_i\partial_P, \quad i = \overline{1,3} \tag{3}$$

(transition to a reference frame moving with an arbitrary linear acceleration).

The extension of Galilean relativity without divergence [generators X_{χ_i} in Eqs. (3)] in the Boussinesq approximation is caused by the change of $\frac{\nabla P}{\rho(S)}$ to $\nabla\left(\frac{P}{\rho_0}\right)$, i.e., by giving the barotropy property to the fluid. This invariance was first found for the equations of an ideal incompressible fluid (Euler equations [7]). However, the physical interpretation of the cause of the extension follows only from an analysis of a more complete system. Moreover, in the Boussinesq approximation, the symmetries of rotation in the vertical plane ($X_{9,10}$) disappear due to the arising difference between the gravitational and inertial masses. The linearization of the equation of state and assumption that the kinetic coefficients are constant transform the set of generators (3) to the set obtained previously in [11].

In the boundary-layer approximation, where gradients in the direction of the mainstream flow are much lower than transverse gradients, the two-dimensional variant of set (1) takes the following form:

$$\frac{\partial u}{\partial t} + u\frac{\partial u}{\partial \xi} + v\frac{\partial u}{\partial \zeta} = -\frac{\partial P}{\partial \xi} + \nu\frac{\partial^2 u}{\partial \zeta^2} - gS\sin\alpha,$$
$$\frac{\partial S}{\partial t} + u\frac{\partial S}{\partial \xi} + v\frac{\partial S}{\partial \zeta} = \kappa_S\frac{\partial^2 S}{\partial \zeta^2} + \frac{u\sin\alpha + v\cos\alpha}{\Lambda}, \tag{4}$$
$$\frac{\partial u}{\partial \xi} + \frac{\partial v}{\partial \zeta} = 0,$$

which, in contrast to the standard form [3], involves the equation of the transfer of the stratifying component and the term presenting the buoyancy forces in the equation of motion. Here, ξ and ζ are the local tangential and normal coordinates; α is the horizontal slope of the flowed surface so that $z = \xi\sin\alpha + \zeta\cos\alpha$, $x = \xi\cos\alpha - \zeta\sin\alpha$, $\mathbf{u} = u\mathbf{e}_x + v\mathbf{e}_y$; and pressure P is determined from the Bernoulli equation for the incident flow. Set (4) was derived with the linearized equation of state $\rho = \rho_0\left(1 - \frac{z}{\Lambda} + S\right)$, where $\Lambda = \frac{d\ln\rho(z)}{dz}$ is the buoyancy scale, which, as well as the transfer coefficients, is assumed to be constant.

The reduction of the space dimension and disregard of transverse gradients in the boundary-layer model reduces the order of set (4) as compared to the original set. As a result, some boundary conditions for Eqs. (1) are surplus, and they cannot be satisfied entirely in the model specified by Eqs. (4). For this reason, some physically important elements of the flow near the boundary are lost, and characteristics where the solution is singular appear [12] as in an ideal fluid.

The symmetry group of set (4) depends on the local horizontal slope of the flowed surface. In the general case $\left(\alpha \neq 0 \text{ and } \alpha \neq \frac{\pi}{2}\right)$, the set of the corresponding generators are

$$X_1 = \partial_t \text{ (time translations);}$$
$$X_2 = \partial_S - g\xi\sin\alpha\partial_P$$
[salinity (density) translations and related pressure translations]; (5)
$$X_3 = 2t\partial_t + 5\xi\partial_\xi + \zeta\partial_\zeta + 3u\partial_u - v\partial_v$$
$$+\left(S + \frac{4\xi\sin\alpha}{\Lambda}\right)\partial_S + 2\left(3P - \frac{g}{\Lambda}\xi^2\sin^2\alpha\right)\partial_P$$

(extensions)

and infinite-dimensional subalgebras

$$X_\pi = \pi(t)\partial_P \text{ (pressure translations);}$$
$$X_\chi = \chi(t)\partial_\xi + \chi_t\partial_u + \frac{\sin\alpha}{\Lambda}\chi\partial_S$$
$$-\left(\chi_{tt}x + \chi\frac{g}{\Lambda}\xi\sin^2\alpha\right)\partial_P$$

(transition to a reference frame moving along the ξ axis);

$$X_\eta = \eta(t,\xi)\partial_\zeta + (\eta_t + \eta_\xi u)\partial_v$$
$$+\frac{\cos\alpha}{\Lambda}\eta\partial_S - \frac{g}{2\Lambda}\sin 2\alpha\int\eta(d\xi)\partial_P$$

(transition to a reference frame moving along the ζ axis).

Here, π, χ, and η are arbitrary functions of their arguments.

The symmetry group given by Eqs. (5) is very similar to the group specified by Eqs. (3) and does not involve rotation groups as in a homogeneous fluid [7]. This anisotropy is caused by the disparity between the ξ and ζ axes, which was *a priori* imposed by the construction of the model. The conditions of incompressibility and barotropy of the fluid are responsible for the equivalence of all reference frames moving translationally with an arbitrary acceleration as in Eqs. (3). Disregard of the transverse velocity component in one of the equations of motion extends the class of these systems.

Reference frames moving with rotation and deformation (generator X_η) are also equivalent in the transverse direction. In this case, the transformation of the transverse velocity component is determined by the substantial derivative of the law of motion $\eta(t, \xi)$ along the tangential velocity component. Direct calculations indicate that this property is inherent in the boundary-layer equations for a homogeneous fluid. For these equations, it is usually emphasized that the law of motion depends only on time [7], and generator X_η is given in the reduced form

$$X_\eta = \eta(t)\partial_\zeta + \eta_t\partial_v.$$

For turbulent flows with zero average velocity and nonzero vorticity, which are realized experimentally by means of oscillating grids [13], the closure condition is set in the form

$$\overline{(u^i\nabla_i)u^j} = \nabla_j\overline{(u^iu^j)} = -\nabla_j K\left(\frac{\partial u^i}{\partial x_j} + \frac{\partial u^j}{\partial x_i}\right), \quad (6)$$

where turbulent viscosity K is an empirical function of the coordinates. The corresponding set of equations for average quantities (hereafter, the averaging bar is omitted), as well as its two-dimensional analogue,

$$\frac{\partial u^i}{\partial t} - \left(\frac{\partial u^i}{\partial x_j} + \frac{\partial u^j}{\partial x_i}\right)\nabla_j K = -\nabla P + K\Delta u_i, \quad (7)$$
$$\mathrm{div}\mathbf{u} = 0,$$

admits the symmetry group whose generators are

$$X_{1\ldots3} = \partial_{x_i}$$

(spatial translations);

$$X_{4\ldots6} = x^i\partial_{x^j} - x^j\partial_{x^i} + u^i\partial_{u^j} - u^j\partial_{u^i}$$

(rotations);

$$X_7 = \mathbf{r}\partial_\mathbf{r} + P\partial_P + K\partial_K, \quad X_8 = \mathbf{u}\partial_\mathbf{u} + P\partial_P \quad (8)$$

(extensions);

$$X_{9\ldots11} = x^i\partial_{u^j} - x^j\partial_{u^i}$$

(inhomogeneous velocity translations);

and the infinite-dimensional subalgebras

$$X = \pi(t)\partial_P \quad \text{(pressure translations)};$$

$$X_{\varphi_i} = \varphi_i(t)\partial_{u_i} - x_i\dot{\varphi}_i(t)\partial_P,$$

$$X_\tau = \tau(t)\partial_t - \dot{\tau}(t)(P\partial_P + K\partial_K)$$

(generalized translations and extensions).

This model of the flow holds the basic symmetries of set (1) that present the properties of uniformity and isotropy of space and time and has groups of extensions and translations specific for this model. At the same time, set of operators (8) and their linear combinations do not involve the operator of the Galilean transformation providing the basis of classical mechanics. Comprehensive analysis of the resulting symmetry properties reveals other physically unjustified properties of the model [generators $X_{9\ldots11}$, X_{φ_i} in Eqs. (7)].

In order to improve the description of the process dynamics, more complex closure conditions are developed. In particular, a set of scale dissipative $k - \varepsilon$ models is extensively used. One of the basic nonstationary models of this set, the so-called $k - \varepsilon - \tau - \vartheta$ model, is used to describe flows of a temperature-stratified fluid and is specified by the set of equations [5]

$$\mathrm{div}\mathbf{u} = 0,$$

$$\frac{du_i}{dt} = -\frac{\partial P}{\partial x_i} + \frac{\partial}{\partial x_j}\left(\nu\frac{\partial u_i}{\partial x_j} - w_{ij}\right) + g_i\alpha T,$$

$$\frac{dT}{dt} = \frac{\partial}{\partial x_i}\left(\kappa_T\frac{\partial T}{\partial x_i} - q_i\right);$$

$$\frac{dw_{ij}}{dt} = \frac{\partial}{\partial x_m}\left(\frac{\nu_t}{\sigma_k}\frac{\partial w_{ij}}{\partial x_m}\right)$$

$$+ P_{ij} - \frac{2}{3}\delta_{ij}\varepsilon - c_1\frac{\varepsilon}{k}\left(w_{ij} - \frac{2}{3}\delta_{ij}k\right) - c_2\left(P_{ij} - \frac{2}{3}\delta_{ij}P\right), \quad (9)$$

$$\frac{dk}{dt} = \frac{\partial}{\partial x_i}\left[\frac{(\nu + \nu_t)}{\sigma_k}\frac{\partial k}{\partial x_i}\right] + \Pi - \varepsilon,$$

$$\frac{dq_i}{dt} = \frac{\partial}{\partial x_j}\left(\frac{\nu_t}{\sigma_\vartheta}\frac{\partial q_i}{\partial x_j}\right) + (1 - c_{2T})P_{iT} - w_{ij}\frac{\partial T}{\partial x_j} - c_{1T}\frac{\varepsilon}{k}q_i,$$

$$\frac{d\vartheta}{dt} = \frac{\partial}{\partial x_i}\left(\frac{\nu_t}{\sigma_T}\frac{\partial\vartheta}{\partial x_i}\right) - 2q_i\frac{\partial T}{\partial x_i} - c_T\frac{\varepsilon}{k}\vartheta,$$

$$\frac{d\varepsilon}{dt} = c_\varepsilon\frac{\partial}{\partial x_i}\left(\frac{\nu_t}{\sigma_\varepsilon}\frac{\partial\varepsilon}{\partial x_i}\right) + c_{\varepsilon1}\frac{\varepsilon}{k}\left(-w_{ij}\frac{\partial u_i}{\partial x_j} + \beta g_i q_i\right) - c_{\varepsilon2}\frac{\varepsilon^2}{k},$$

where $u_i = \bar{u}_i$, $T = \bar{T}$, and $P = \bar{P}$ are the average velocity, temperature, and pressure, respectively; $w_{ik} = \overline{u_i'u_k'}$, $q_i = \overline{T'u_i'}$, and $\vartheta = \overline{T'^2}$ are the second-order moments; α, κ_T, ν, and $\nu_t = \dfrac{c_\mu k^2}{\varepsilon}$ are the coefficients of thermal expansion, heat conduction, kinematic molecular viscosity, and kinematic turbulent viscosity, respectively; k is the kinetic energy of turbulent pulsations; ε is the dissipation rate for the turbulent kinetic energy; $\Pi = -\overline{u_i'u_k'}\dfrac{\partial U_i}{\partial x_k}$ is the outcome of turbulence,

$$P_{ij} = -w_{im}\frac{\partial u_j}{\partial x_m} - w_{jm}\frac{\partial u_i}{\partial x_m} + \alpha(g_i q_j + g_j q_i),$$

$$P_{iT} = -q_j\frac{\partial u_i}{\partial x_j} + \beta g_i \vartheta;$$

and c_1, c_2, c_{1T}, c_{2T}, c_ε, $c_{\varepsilon 1}$, $c_{\varepsilon 2}$, c_μ, σ_k, and σ_ϑ are empirical constants (fitting parameters) fitted from the condition of maximum agreement between calculations and experimental data.

Complex set (9) is characterized by a poor set of the symmetry groups whose generators are

$X_1 = \partial_t$, $X_2 = \partial_T$ (translations of time and temperature),

and infinite-dimensional subalgebras

$$X_\pi = \pi(t)\partial_P$$

(pressure translations),

$$X_{\chi_i} = \chi_i(t)\partial_{x_i} + \chi_i'(t)\partial_{u_i} - \chi_i''(t)x_i\partial_P, \quad i = 1, 2, 3 \quad (10)$$

(transition to a reference frame moving with an arbitrary linear acceleration).

Translation operators X_1, X_2, and X_π for set (9) coincide with the respective operators for set (1) with the linearized [as in set (9)] equation of state. Set (9) derived in the Boussinesq approximation conserves the generalized Galilean invariance given by Eq. (4) despite all the introduced complications. Symmetries given by Eqs. (10) do not involve the rotation group [such as X_8 from Eqs. (2)]. A simpler analogue of the model given by Eqs. (9) for a homogeneous fluid ($k - \varepsilon$ models) also does not obey rotation groups presenting the fundamental isotropy of space.

As a whole, to completely estimate the equivalence degree for the set of equations, it is necessary to determine, in addition to differential symmetries, their discrete symmetries [14] and integral invariants. However, even the knowledge of only point invariants substantially simplifies the construction of exact and approximate (asymptotic) solutions and makes it possible to classify boundary conditions allowing the total or partial separation of variables. The reduction of all intermediate calculations when constructing asymptotic solutions to operations from the corresponding algebra enables one to represent solutions in the invariant form independent of the choice of the initial variables, i.e., to determine the physical meaning of the equivalence condition for the sets and the scope of applicability of the derivative models in each particular case.

ACKNOWLEDGMENTS

This work was supported in part by the Russian Foundation for Basic Research (project no. 02-05-65383), the Ministry of Education of the Russian Federation (State Program "Integratsiya," project no. 02-Ya0058), and the Foundation for Support of Young Scientists, Presidium of the Russian Academy of Sciences (project "Investigation of the Formation and Evolution of Free Stratified Flows").

REFERENCES

1. L. D. Landau and E. M. Lifshitz, *Course of Theoretical Physics*, Vol. 6: *Fluid Mechanics* (Nauka, Moscow, 1986; Pergamon, New York, 1987).
2. V. M. Kamenkovich, *Foundations of the Ocean Dynamics* (Gidrometeoizdat, Leningrad, 1973).
3. H. Schlichting, *Boundary Layer Theory* (McGraw-Hill, New York, 1968; Inostrannaya Literatura, Moscow, 1956).
4. L. G. Loitsyanskiĭ, *Mechanics of Fluids and Gas* (Nauka, Moscow, 1987).
5. E. V. Bruyatskiĭ, *Turbulence Stratificated Jet Flow* (Naukova Dumka, Kiev, 1986).
6. G. Birkhoff, *Hydrodynamics: a Study in Logic, Fact, and Similitude* (Princeton University Press, Princeton, N.J., 1960; Inostrannaya Literatura, Moscow, 1954).
7. L. V. Ovsyannikov, *Group Analysis of Differential Equations* (Nauka, Moscow, 1978; Academic, New York, 1982).
8. L. V. Ovsyannikov, Prikl. Mat. Mekh. **58** (4), 30 (1994).
9. V. V. Bublik, Din. Sploshnoĭ Sredy, No. 113, 19 (1998).
10. B. W. Char, K. O. Geddes, G. N. Gonnet, *et al.*, *Maple V. Library Reference Manual* (Springer, New York, 1991).
11. V. G. Baidulov and Yu. D. Chashechkin, Dokl. Akad. Nauk **364**, 186 (1999) [Dokl. Phys. **44**, 22 (1999)].
12. Yu. V. Kistovich and Yu. D. Chashechkin, Prikl. Mat. Mekh. **63** (4), 611 (1999).
13. I. P. D. De Silva and H. J. S. Fernando, J. Fluid Mech. **240**, 355 (1992).
14. A. V. Kistovich and Yu. D. Chashechkin, Dokl. Akad. Nauk **380**, 747 (2001) [Dokl. Phys. **46**, 718 (2001)].

Translated by R. Tyapaev

Doklady Physics, Vol. 47, No. 12, 2002, pp. 892–894. Translated from Doklady Akademii Nauk, Vol. 387, No. 6, 2002, pp. 764–766.

MECHANICS

Obstacle to the Reduction of Nonholonomic Systems to the Hamiltonian Form

A. V. Borisov and I. S. Mamaev

Presented by Academician V.V. Kozlov July 3, 2002

Received July 30, 2002

1. EQUATIONS WITH AN INTEGRAL INVARIANT ON A TORUS

As is known, a system of differential equations that is defined on a two-dimensional torus $\mathbb{T}^2$ and has an invariant positive-density measure can be reduced to the form

$$\dot{x} = \frac{\lambda}{\Phi(x, y)}, \quad \dot{y} = \frac{\mu}{\Phi(x, y)} \tag{1}$$

in certain coordinates $x \bmod 2\pi$ and $y \bmod 2\pi$. Here, λ and μ are the constants ($\lambda^2 + \mu^2 \neq 0$) and $\Phi(x, y)$ is the smooth function 2π-periodic in the variables x and y.

Equations (1) have the invariant measure $\iint \Phi(x, y)dx dy$. Averaging the right-hand sides over this measure, we arrive at the differential equations

$$\dot{u} = \frac{\lambda}{\nu}, \quad \dot{v} = \frac{\mu}{\nu}, \quad \nu = \frac{1}{4\pi^2}\int_0^{2\pi}\int_0^{2\pi} \Phi(x, y)dx\, dy. \tag{2}$$

From the results obtained by Kolmogorov [1], it follows that if Φ: $\mathbb{T}^2 \longrightarrow \mathbb{R}$ is a smooth (analytic) function, the smooth (analytic) change of variables $x, y \longrightarrow u, v$ reduces the system given by Eqs. (1) to the form of Eqs. (2) for almost all rotation numbers $\omega = \frac{\lambda}{\mu}$ satisfying the condition of strong incommensurability. We recall that this condition is as follows: there are numbers $a > 0$ and $h > 0$ such that the inequality $|m - n\omega| \geq ah^n$ is valid for any integers $m > 0$ and $n > 0$.

For resonant (i.e., rational) number $\omega = \frac{p}{q}$, where p and $q \in \mathbb{Z}$, the torus $\mathbb{T}^2$ is stratified into the family of closed periodic orbits so that the condition responsible for reduction from form (1) to form (2) is equivalent to the equality of the periods for different closed trajectories. When the periods for different trajectories on the resonant torus are different, system (1) has the mixing property [6]. Let us apply the above speculations to investigate one nonholonomic problem.

2. NONHOLONOMIC CHAPLYGIN SYSTEMS

The integration of nonholonomic dynamic systems is based, as a rule, on the Euler–Jacobi theorem, which makes it possible to reduce the above system to system (2) on the torus by using known first integrals. Let us consider, for example, the following equations for rolling a nonholonomic Chaplygin ball:

$$\begin{gathered}\dot{\mathbf{M}} = \mathbf{M}\times\boldsymbol{\omega}, \quad \dot{\boldsymbol{\gamma}} = \boldsymbol{\gamma}\times\boldsymbol{\omega},\\ \mathbf{M} = \mathbf{I}\boldsymbol{\omega} + D\boldsymbol{\gamma}\times(\boldsymbol{\omega}\times\boldsymbol{\gamma}), \quad D = ma^2,\end{gathered} \tag{3}$$

where $\mathbf{I}$ is the inertia tensor of the ball about its center, m is the mass of the ball, and a is its radius. Equations (3) are written in the components of the kinetic momentum $\mathbf{M}$ with respect to the contact point, angular velocity $\boldsymbol{\omega}$, and the unit vector $\boldsymbol{\gamma}$ along the vertical direction and have the invariant measure with the density

$$\rho = (1 - D(\mathbf{A}\boldsymbol{\gamma}, \boldsymbol{\gamma}))^{-\frac{1}{2}}, \quad \mathbf{A} = (\mathbf{I} + D\mathbf{E})^{-1}, \quad \mathbf{E} = \left\|\delta_i^j\right\| \tag{4}$$

and four first integrals

$$\begin{gathered}F_1 = (\mathbf{M}, \boldsymbol{\omega}), \quad F_2 = (\mathbf{M}, \boldsymbol{\gamma}),\\ F_3 = (\boldsymbol{\gamma}, \boldsymbol{\gamma}) = 1, \quad F_4 = (\mathbf{M}, \mathbf{M}),\end{gathered} \tag{5}$$

which provide integrability of system (3) according to the Euler–Jacobi theorem and reduction to the form of Eqs. (1). In the explicit form, system (3) was reduced by Kozlov [2] (see also [7]). For this reduction, it is possible to use sphero-conical coordinates on the Poisson sphere

$$\gamma_i^2 = \frac{(a_i - q_1)(a_i - q_2)}{(a_i - a_j)(a_i - a_k)}, \quad i, j, k = 1, 2, 3$$

and, on the general level of integrals [for $(\mathbf{M}, \boldsymbol{\gamma}) = 0$],

Institute of Computer Research,
ul. Universitetskaya 1, Izhevsk, 426034 Russia

1028-3358/02/4712-0892$22.00

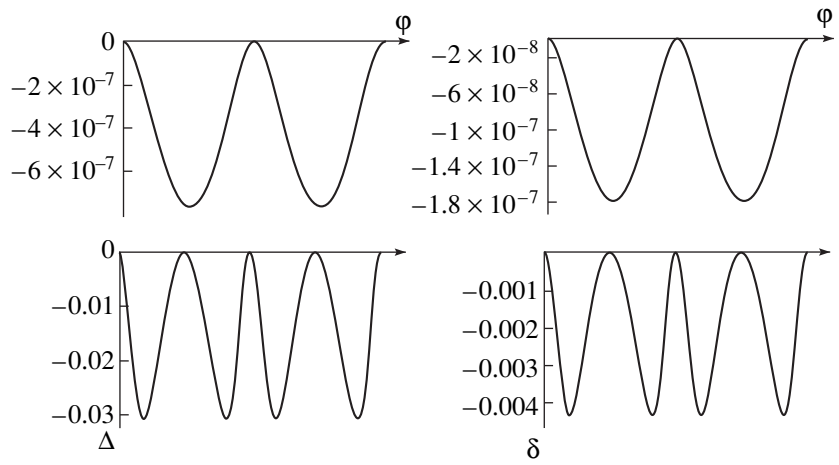

Absolute Δ and relative δ deviations of the periods on the resonant tori. It is seen that the periods on the torus are different for $D \neq 0$. The system parameters are $\mathbf{I}_1 = 1$, $\mathbf{I}_2 = 1.5$, $\mathbf{I}_3 = 3$, $D = mR^2 = 1$, $g_0 = 0$, $\mathbf{E} = 10.0$, and $(\mathbf{M}, \boldsymbol{\gamma}) = 3.0$.

the equations take the form of Eqs. (1), where the function $\Phi(x, y)$ has the form

$$\Phi = [\xi^{-1}(x) - \eta^{-1}(x)]\sqrt{(\alpha - \xi(x))(\alpha - \eta(y))}. \quad (6)$$

Here, the functions $\xi(x)$ and $\eta(y)$ are 2π-periodic in the variables x and y and are derived from the inversion of Abelian integrals. The reduction given in [2] can also be done by using the result obtained in [3], according to which system (3) is Hamiltonian on the level $(\mathbf{M}, \boldsymbol{\gamma}) = 0$ after time change $d\tau = \mu dt$, where μ is determined by Eq. (4). Indeed, after time change, the action–angle variables on the nonsingular invariant two-dimensional tori can be introduced so that the angular variables coincide with the required x and y variables from Eqs. (1) [7].

3. OBSTACLE TO REDUCTION TO THE HAMILTONIAN FORM

According to the above discussion and study [3], the four-dimensional phase space that is obtained from (3) by fixing the integrals $F_2 = (\mathbf{M}, \boldsymbol{\gamma})$ and $F_3 = (\boldsymbol{\gamma}, \boldsymbol{\gamma}) = 1$ is stratified into two-dimensional invariant tori, where motion reduces to the form specified by Eqs. (1) and (6). As follows from the Liouville theorem, an integrable Hamiltonian system near a nonsingular torus can always be reduced to the form of Eq. (2). Therefore, if such a reduction is impossible for the tori that are specified by Eqs. (1) and (6) and arise in the Chaplygin problem, Eqs. (3) cannot be written in the Hamiltonian form [on the level $(\mathbf{M}, \boldsymbol{\gamma}) = 0$ and $(\boldsymbol{\gamma}, \boldsymbol{\gamma}) = 1$].

Our particularly accurate numerical calculations indicate that periods for trajectories on different resonant invariant tori are different along the same torus. In addition, the impossibility of reduction is especially pronounced in the vicinity of separatrices dividing regions with different dynamic behaviors.[1]

The figure shows the numerical results for periods of motion in the Chaplygin system on the resonant tori for $D \neq 0$ and $D = 0$. The latter condition corresponds to the Hamiltonian case. In this system, the invariant torus is parameterized by integrals (5), which are fitted (numerically) so that the torus is resonant; i.e., all the trajectories on it become closed. We take a section of the torus by a certain plane transverse to these trajectories. Next, the points lying on the closed curve that is formed by the section are parameterized by a certain angular coordinate $\varphi \in (0, 2\pi)$. For each value of φ, we construct a trajectory starting from the corresponding initial point on the chosen section and calculate the period of motion along it $T(\varphi)$. The periods are different for different trajectories (dependences $\Delta(\varphi) = T(\varphi) - T(0)$ and $\delta(\varphi) = \dfrac{T(\varphi) - T(0)}{T(0)}$ are shown in the figure). The calculations and choice of the initial conditions are so accurate that the period is calculated with an accuracy of $\Delta T = 10^{-8}$. (Only six significant figures are given for G, although it was calculated with an accuracy of 10^{-10}.) Thus, the periods of motion on the torus are different in the nonholonomic system ($D \neq 0$) and are identical for the holonomic case ($D = 0$) (more exactly,

[1] According to the necessary condition for such a reduction [2], if $\Phi(x, y)$ can be expanded into the Fourier series

$$\Phi(x, y) = \sum \varphi_{m,n} \exp[i(mx + ny)],$$

$$\varphi_{m,n} = \bar{\varphi}_{-m,-n}$$

on a torus and reduction is possible, the series

$$\sum_{|m| + |n| \neq 0} \left| \frac{\varphi_{m,n}}{m\lambda + n\mu} \right|^2$$

is convergent.

the deviation in the latter case does not exceed the calculation error).

4. CONCLUSION

The problem of the reduction of Eqs. (3) to the Hamiltonian form was first formulated by Kozlov [4]. In [5], this problem was related to the problem of "weak" mixing (weak chaos) on invariant tori. The spectrum of a dynamic system on such tori can be continuous, although all the characteristics of chaos (Lyapunov exponent and entropy) are equal to zero. In this study, we showed numerically that reduction to the Hamiltonian form is impossible on nonresonant tori. The problem of reduction for nonresonant tori that do not satisfy Kolmogorov's condition of strong incommensurability is still open. The statistical aspects of the behavior of system (1) were considered in [6].

In conclusion, we note that the reduction of a dynamic system to the Hamiltonian form, which may be hidden [5], and the determination of obstacles to this reduction are much more complex problems than the problem of first integrals and invariant measure and are still little studied [4]. As is seen, these obstacles for integrable systems can nevertheless be analyzed numerically.

A "cruder" obstacle to reduction to the Hamiltonian form is typical for nonintegrable systems and is associated with the absence of an invariant measure with the analytic density for nonholonomic equations. This obstacle was mentioned in [2], where it was also established that there is no invariant measure for Celtic stones, which exhibit rather exotic dynamic behavior and whose phase space involves complex attractive manifolds.

ACKNOWLEDGMENTS

We are grateful to V.V. Kozlov for stimulating discussions and helpful remarks and to A.A. Kilin, who developed the software package for numerical experiments.

REFERENCES

1. A. N. Kolmogorov, Dokl. Akad. Nauk **93**, 763 (1953).
2. V. V. Kozlov, Usp. Mekh. **8** (3), 85 (1985).
3. A. V. Borisov and I. S. Mamaev, Mat. Zametki **70** (5), 793 (2001).
4. V. V. Kozlov, *Symmetries, Topology, and Resonances in Hamiltonian Mechanics* (Izd. Udmurtskogo Univ., Izhevsk, 1995).
5. A. V. Borisov and I. S. Mamaev, *Poisson Structures and Lee Algebras in Hamiltonian Mechanics* (Izd. RKhD, Izhevsk, 1999).
6. V. V. Kozlov, Dokl. Akad. Nauk **381** (5), 596 (2001).
7. A. A. Kilin, Regul. Chaot. Dyn. **6** (3), 291 (2001).

Translated by Yu. Vishnyakov

Doklady Physics, Vol. 47, No. 12, 2002, pp. 895–899. Translated from Doklady Akademii Nauk, Vol. 387, No. 6, 2002, pp. 767–771.

MECHANICS

Cavitation Flows in Viscous-Fluid Films

O. V. Voinov

Presented by Academician G.G. Chernyĭ September 2, 2002

Received September 2, 2002

The Prandtl–Taylor–Birkhoff problem, i.e., the mathematical description of flows with cavitation in thin films of a viscous fluid [1–3], is considered. A closed model of cavitation flows is proposed on the basis of the analysis of unsteady dynamics of cavitation bubbles and their hydrodynamic interaction in a thin film.

The dynamics of cavitation bubbles involve strongly nonlinear effects. When a bubble undergoes Rayleigh collapse [4] in a low-viscosity fluid, the spherical cumulation of energy is possible. Another practically important mechanism of unsteady energy cumulation accompanying bubble collapse is caused by bubble nonsphericity. Dynamic variation in the bubble shape, together either with stream inhomogeneity (the presence of a solid boundary and stream acceleration) or with the initial momentum, can induce anomalous non-Rayleigh energy cumulation responsible for the formation of a thin fluid "superjet," whose velocity is enormous and can even be infinite (in the framework of the mathematical model of an incompressible fluid) [5]. The infinite velocity of a fluid stream for anomalous cumulation, contrary to Rayleigh cumulation, corresponds to a nonzero bubble volume, i.e., to an incomplete collapse.

The dynamics of many cavitation bubbles are studied most comprehensively for a low-viscosity fluid. The Lagrange equations were proposed for the dynamics of a system of bubbles undergoing ultrasonic cavitation [6]. The dynamics of a system of interacting bubbles in arbitrary vortex-free streams are described by asymptotic models and equations [7–10].

Cavitation in thin fluid films, which is one of the most important mechanical problems [1–3], is of interest in connection with the lubrication and technologies of film deposition on solids. However, this problem is insufficiently studied. In the phenomenological theory of cavitation in films, formal schemes of flows were based on empirical information [11–13]. Here, in contrast to this theory, we consider cavitation flows in the asymptotic model of bubble cavitation in the film of a relatively high-viscosity fluid.

A fluid of density ρ flows steadily, forming a thin film between the surfaces of solids 1 and 2 for low Reynolds numbers. Pressure p in the neighborhood of the minimum film thickness $h = h_0 > 0$ is described by the following Reynolds equation [14] in the coordinates x and y on a tangential plane:

$$\operatorname{div}\left\{h^3\frac{\rho}{\mu}\nabla p - 6\rho h(\mathbf{u}_1 + \mathbf{u}_2)\right\} = 0. \qquad (1)$$

Here, μ is the viscosity, $\mathbf{u}_1$ and $\mathbf{u}_2$ are the velocities of the respective surfaces, $\frac{|\mathbf{u}|h_0}{\nu} \ll 1$, $\mathbf{u} = \mathbf{u}_1 + \mathbf{u}_2$, and $|\nabla h| \ll 1$. Let $\mathbf{u}_1$ and $\mathbf{u}_2$ be aligned with each other and $u_y = 0$. If one of the surfaces is a sphere of radius $R_S \gg h_0$ and the other surface is a plane, thickness is $h = h_0 + \frac{x^2 + y^2}{2R_S}$. For larger thicknesses $\frac{h}{h_0} \longrightarrow \infty$, we set pressure $p_\infty > 0$. For negative pressures in the region of low thicknesses, where h increases in the direction of motion of the surfaces, cavitation is possible. It is necessary to determine when the cavitation flow is described by Eq. (1) and to find the boundary conditions on the cavity contour.

PARAMETERS OF FILM BUBBLES

Let surface 1 have microscopic inhomogeneities coupled with small gas bubbles, which can be in equilibrium and are not dissolved because of their coupling with an inhomogeneity [15]. Identical bubbles form a network with the mean number of nodes n_S per unit area. We consider sufficiently small-mesh networks; i.e., the case $n_S \sim \frac{1}{h_0^2}$ is allowed, but the case $n_S \ll \frac{1}{h_0^2}$ is excluded. The diameter of a bubble is much smaller than the network mesh. Bubbles are only near surface 1; the case of bubbles in the fluid bulk can be considered similarly. Velocity u_1 is not low compared to u_2.

Tyumen Branch, Institute of Theoretical and Applied Mechanics, Siberian Division, Russian Academy of Sciences, Taimyrskaya ul. 74, Tyumen, 625026 Russia
e-mail: o.voinov@mtu-net.ru

1028-3358/02/4712-0895$22.00

Temperature T is constant. The pressure p_v of saturated vapors is low: $p_v \ll p_\infty$. The gas in the bubble is ideal; i.e., its pressure is $p_g = \rho_g R_g T$, where ρ_g is the density. The concentration or density ρ_{g1} of the gas in the fluid near the bubble follows the Henry law $\rho_{g1} = kp_g$, where k = const. The normal stress in the fluid on the bubble is related to the gas pressure by the Laplace expression $p_n = -p_g + 2H\sigma$, where σ is the surface tension, H is the average interface curvature, and $H = \frac{1}{R}$ for the sphere of radius R. There are also certain conditions on the bubble–solid contact line.

As the volume V of the bubble increases, the mass of the gas inside it depends on gas diffusion to the fluid. The role of this diffusion can be estimated from the Peclet number, which is convenient to define as $\mathrm{Pe} = \frac{(R\lambda)^2}{D\tau}$, where D is the diffusivity $\left(\frac{D}{\nu} \ll 1\right)$, R is the characteristic bubble radius (radius of the sphere of volume V), $\lambda = \left(\frac{\rho_g}{\rho_{g1}}\right)^{1/3}$ (ρ_g and ρ_{g1} are the equilibrium values for V = const), and τ is the characteristic time of variation of the volume V. At the entrance to a cavity, time τ can be very small (much smaller than 1 μs).

For fast growth of the bubble, the Peclet numbers are high, $\mathrm{Pe} \gg 1$, and the gas mass inside the bubble is almost constant. If the normal stress p_n is approximately constant along the surface, the stress p_n has a maximum $p_n^* = \max\{p_n(V)\}$ according to the capillary-equilibrium problem. If pressure p in the film is less than its critical value p_n^*, the bubble can spontaneously grow. A spherical bubble also has the maximum stress $p_n^* = \frac{4}{3}\frac{\sigma}{R_*}$, where R_* is the critical radius. We consider a spherical bubble with the same stress p_n^* as on a nonspherical bubble associated with a wall inhomogeneity.

The inertial effects are immaterial in bubble dynamics if viscosity is high, i.e., if $\frac{R^2}{\nu\tau} \ll 1$, where ν is kinematic viscosity. The equation of radius variation has the form

$$\gamma\mu\dot{R}R^{-1} + 2\sigma R^{-1} = p_g - p, \qquad (2)$$

where p is the mean pressure in the film, $\gamma = 4$, and the bubble is far from the wall. The bubble is spaced from the wall by a distance much smaller than h, so that the bubble moves with the wall velocity $\mathbf{u}_1$. Bubble–wall interaction can approximately be taken into account by considering $\gamma > 4$.

The asymptotic method described below is in principle not restricted to the approximate spherical-bubble model, and deformations of the bubble can be taken into account. We note that the bubble does not break in the shear stream due to the capillary forces if its radius is sufficiently small.

ASYMPTOTIC METHOD OF THE TRANSITION LAYER

A steady cavity in a film differs fundamentally from cavities in the case of developed cavitation at large Reynolds numbers. The boundary of this cavity is not a stream line, and the fluid flows through it [1–3, 11–13].

Let the critical stress be much smaller than the pressure minimum without cavitation: $p_n^* \ll \left|p_{\min}^0\right|$. In this case, the effect of bubbles on the flow in the film can manifest itself in the thin transition layer, when the fluid flows into the cavity.

The flow of the film with bubbles is described by Reynolds equation (1) with variable density $\rho = \rho_0(1 - c)$ $\left(\rho_0 = \text{const, and } c = \frac{n_S V}{h} \text{ is a low concentration of bubbles}\right)$. Such an approach is rigorous if the velocity magnitude $\mathbf{w} = -\frac{h^2}{12\mu}\nabla p$ is much smaller than $0.5|\mathbf{u}|$. This is the case near the cavity contour L, at which we take $p = 0$ for solving the Reynolds equation for an incompressible ($\rho = \rho_0$) fluid. We introduce the coordinate ξ along the external normal n at the point $\mathbf{x}_0 \in L$, where $\xi = 0$. Let the indicated solution p have a minimum in ξ, $p_{\min}$, for small $\xi = \xi_M$ (at the point $\mathbf{x}_M = \mathbf{x}_0 + \xi_M\mathbf{n}$). We consider a small neighborhood of the point $\mathbf{x}_M$: $|\mathbf{x} - \mathbf{x}_M| \ll l$ ($l = (R_S h_0)^{1/2}$ is the scale of variation in h). We approximate the quantity h by two terms of the Taylor expansion at the point $\mathbf{x}_M$. We consider that thickness increases in the direction of velocity, $u\nabla_x h > 0$. Taking into account that the derivatives of p and c along the normal are much greater than those along the layer, we simplify the equation of the flow:

$$\frac{h_M^3}{12\mu}\frac{\partial p}{\partial \xi} = \frac{u}{2}\{\varepsilon(\xi - \xi_M) - n_x h c\}, \quad \varepsilon = \frac{\partial h}{\partial x}(\mathbf{x}_M), \quad (3)$$

$h_M = h(\mathbf{x}_M)$, $un_x < 0$, $u \equiv u_x$, $u_1 \equiv u_{1x}$. The quantity ε is small: $|\varepsilon| \sim \frac{h_0}{l} \ll 1$. According to Eq. (3), the strong inequality $|\mathbf{w}| \ll 0.5|u|$ is valid for small ξ_M and ξ. Equation (3) is asymptotically exact for $c \ll 1$ and $\xi_M \ll l$, when the transition layer is thin.

In the transition layer, the concentration c decreases with an increase in ξ, and the pressure p approaches the

solution to the Reynolds equation for an incompressible fluid:

$$p = p_{\min} + \frac{a(\xi - \xi_M)^2}{2} + \ldots, \quad \frac{\xi - \xi_M}{\xi_M} \longrightarrow +\infty,$$
$$a = 6\mu u \varepsilon h_M^{-3}, \quad \xi_M = \left(-\frac{2p_{\min}}{a}\right)^{1/2}. \tag{4}$$

The quantity $p_{\min}$ is unknown. The compatibility with a cavity requires that

$$n_x hc - \varepsilon(\xi - \xi_M) \longrightarrow 0, \quad \frac{\xi - \xi_M}{\xi_M} \longrightarrow -\infty. \tag{5}$$

To complete the problem, it is necessary to have the model of the variation in the bubble volume V with varying pressure p. For this purpose, we use the dynamic equation for the spherical bubble at large Peclet numbers

$$p = \frac{p_n^*}{2}\left(\frac{R_*^3}{R^3} - 3\frac{R_*}{R}\right) - \frac{\gamma\mu u_1 n_x}{R}\frac{\partial R}{\partial \xi}. \tag{6}$$

Equations (3) and (6) describe the effect of interaction between bubbles that is caused by the influence of their concentration on the fluid flow. In the dimensionless notation

$$Y = \frac{R}{R_*}, \quad \bar{p} = p\frac{2}{p_n^*}, \quad \varsigma = -\frac{\xi - \xi_M}{l_*},$$
$$l_*^2 = \frac{p_n^*}{2a}, \quad \beta = \frac{\gamma u_1 n_x}{6u\varepsilon}\left(\frac{h_M}{l_*}\right)^3, \quad G = n_S\frac{4}{3}\pi R_*^3\frac{|n_x|}{|\varepsilon| l_*} \tag{7}$$

we obtain the boundary-value problem

$$\frac{d\bar{p}}{d\varsigma} = \varsigma - GY^3, \quad \bar{p} = \frac{1}{Y^3} - \frac{3}{Y} - \frac{\beta}{Y}\frac{dY}{d\varsigma},$$
$$\bar{p} = -\alpha + \frac{\varsigma^2}{2} + \ldots, \quad \varsigma \longrightarrow -\infty, \tag{8}$$
$$\varsigma - GY^3 \longrightarrow 0, \quad \varsigma \longrightarrow +\infty.$$

The dimensionless parameters β and G are independent, and the constant α is determined from Eq. (8): $\alpha = \alpha(\beta, G)$. The parameter G is proportional to the number n_S or to the initial (critical) gas volume per unit film area. The cavity equation $GY^3 = \zeta$ (for $\nabla p \approx 0$) is established for a low bubble concentration c, because

$$c \approx GY^3 n_x^{-1} E, \quad E = |\varepsilon|\frac{l_*}{h_M} \sim \frac{l_*}{l} \ll 1. \tag{9}$$

We note that this theory is suitable nonuniformly in n_x.

It is reasonable to consider the boundary-value problem given by Eqs. (8) only for $\beta > 0.3$. The solution has no real meaning for β close to zero, because it easily fails for small pressure fluctuations in the film.

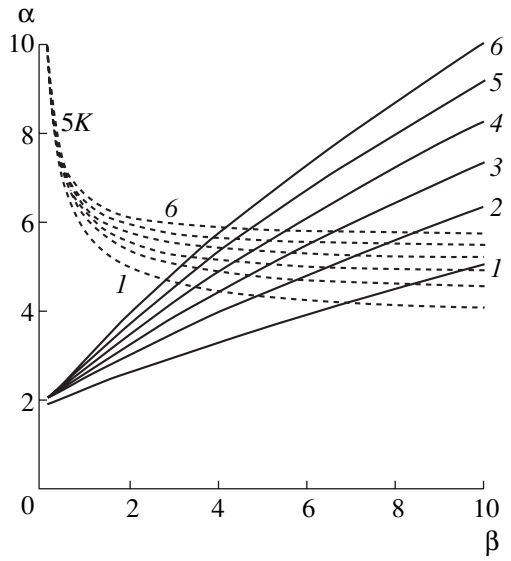

Fig. 1.

PROPERTIES OF THE FLOW MODEL

The dependence of the dimensionless-pressure minimum $-\alpha$ on the bubble dynamic parameter β is given in Fig. 1 (solid curves *1*, *2*, …, and *6* corresponds to $G = 10^{-1}, 10^{-2}, \ldots$, and 10^{-6}, respectively). The minimum $-\alpha$ can be markedly lower than the critical value -2. It depends weakly on the parameter G: the quantity α varies by a factor less than 2, when G varies by a factor of 10^5.

The boundary conditions for pressure p satisfying the Reynolds equation for an incompressible fluid at the entrance to a cavity ($u_n < 0$) have the form

$$p = 0; \quad \nabla_n p = -\xi_M a, \quad \xi_M = Kh\left|\frac{\gamma u_1 n_x}{u\varepsilon}\right|^{1/3} \tag{10}$$

($\nabla_n = \mathbf{n}\cdot\nabla$, $K = (2\alpha)^{1/2}(6\beta)^{-1/3}$). The dependence of K on β is given in Fig. 1 by the dashed lines.

For large β, dependences are simple. In the limit $\beta \gg 1$, the function $K(\beta, G)$ is independent of β and is close to unity: $K(\beta, G) \approx 0.77G^{-0.03}$. The effect of the number n_S of cavitation nuclei is absent, because $K \sim n_S^{-0.03}$. The pressure minimum is independent of the critical stress p_n^*, and $p_{\min} \sim u$. For $\beta > 2$, the transition-layer thickness ξ_M is independent of velocity $\left(\text{for } \frac{u_1}{u} = \text{const}\right)$ and is small: $\xi_M \ll l$. For $\beta < 2$, the latter condi-

tion coincides with $l_* \ll l$, which is equivalent to $p_n^* \ll |p_{\min}^0| \sim \mu|u|\frac{l}{h_0^2}$. The thickness $\xi_M \gg h_M$ (because $\varepsilon \ll 1$).

The solution reveals the flow pattern in the thin transition layer: the medium in the film undergoes a phase transition controlled by bubble dynamics. A low initial gas content in the film does not hinder this transition, although the dissolved gas is not noticeably released. At the beginning of the layer, the medium behaves as if it were incompressible, whereas at the end of the layer, the inhomogeneous medium is easily compressible due to the presence of bubbles, and the pressure gradient disappears. The end of the transition layer coincides asymptotically with a cavity—the region of constant pressure. In the cavity, the inhomogeneous medium in the film has a simple equation of state: pressure is equal to $p = 0$ independently of average density. The solution quantitatively explains the film failure—the existence of a visible cavity boundary fixed in many experiments [2, 11–13].

The second boundary condition in Eqs. (10) does not coincide with any known phenomenological boundary conditions (Swift–Stieber, Prandtl–Hopkins, Floberg, Coyne–Elrod [1–3, 11–13]).

Let all the conditions under which Eqs. (10) were obtained be satisfied and $p_n^* \ll p_\infty$. According to Eqs. (10), $\nabla_n p$ contributes term $|\mathbf{w}| = O(|\varepsilon|^{2/3})|u| = O\left(\left(\frac{h_0}{R_S}\right)^{1/3}\right)|u|$ to the average velocity in the film. Neglecting this term compared to $\frac{|u|}{2}$ and using Eqs. (10), we obtain the condition $\nabla_n p = 0$ at the entrance to the cavity. This is the Swift–Stieber boundary condition [12, 13].

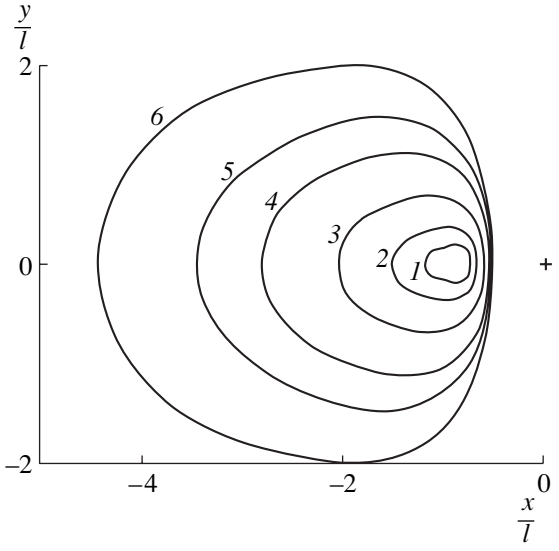

Fig. 2.

STRUCTURE OF THE SECOND DENSITY JUMP

At the exit from the cavity, the region of the easily compressible medium borders the region of incompressible fluid. The structure of the boundary region is qualitatively described by the one-dimensional problem of steady flow in a constant-thickness film. For $\xi \longrightarrow -\infty$, the bubble concentration is $c \longrightarrow c_0 \ll 1$. For $\xi \longrightarrow +\infty$, $c \longrightarrow 0$. According to the solution of the flow problem with these conditions, the front of density variation is thin: its thickness is $\delta \sim h(6c_0)^{-1/2}$. Consequently, at the exit from the cavity, density increases stepwise, whereas pressure varies continuously. This is the mixing of fluids with and without bubbles rather than simply a phase transition as in the transition layer.

CAVITY SHAPE

The flow was calculated for a sphere–plane system unusual for experiments in which the film surfaces are conventionally cylindrical [2, 11–13]. Introducing modified pressure $\tilde{p}$, we rewrite Eq. (1) in the form

$$\nabla \cdot h^3 \nabla \tilde{p} = 0, \quad \tilde{p} = p - p^0, \quad p^0 = -\frac{6}{5}\mu u x h^{-2}. \tag{11}$$

The conditions at the cavity contour L are written as

$$p = 0, \quad \nabla_n \tilde{p} = -\nabla_n p^0 + f, \quad f = 0, \quad u_n < 0,$$
$$f = 6\mu u_n \frac{h - h^*}{h^3}, \quad u_n > 0 \tag{12}$$

($u_n = \mathbf{n} \cdot \mathbf{u}$). If $\mathbf{x}_0 \in L$ for $u_n > 0$, $\mathbf{x}^* \in L$ for $u_n < 0$, $y^* = y_0$; $h^* = h(\mathbf{x}^*)$. For a given pressure p_∞ at infinity and the second condition from Eqs. (12) for the given contour L, the problem was solved (in the dimensionless notation) by the finite-difference method with the grid in the polar coordinate system r, θ. The condition $p = 0$ at L is equivalent to the condition that $\min\max\{p(\mathbf{x}_1) - p(\mathbf{x}_2)\}$, $\mathbf{x}_1, \mathbf{x}_2 \in L$ is reached. To solve the minimax problem, the radius $r(\theta)$ of the curve L was represented by a partial sum of the Fourier series at the interval $(0, \pi)$. The number N of the highest harmonics $\cos(N\theta)$ was taken so that accuracy was not worse than 0.01, for which $N \le 8$ is sufficient. The calculated cavity contours are shown in Fig. 2 for various $\Lambda = \frac{p_\infty}{p_m^0}$, where

$$p_m^0 = \frac{9\sqrt{6}}{40}\mu|u|\frac{l}{h_0^2}, \quad l = \sqrt{R_S h_0}. \tag{13}$$

Curves *1*, *2*, …, and *6* correspond to $\Lambda = 0.93$, 0.79, 0.54, 0.3, 0.2, 0.1, respectively, and to the velocity $u < 0$.

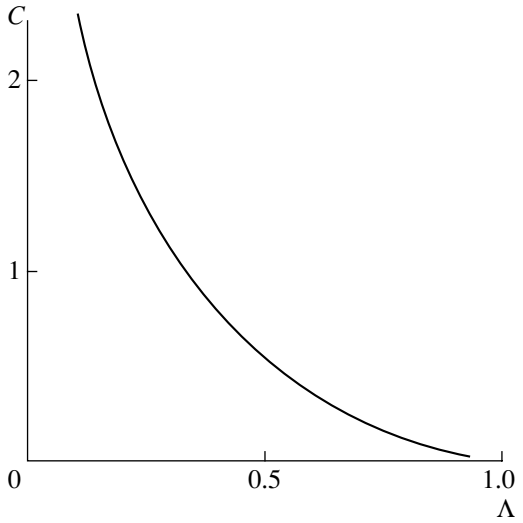

Fig. 3.

The repulsion force between the sphere and plane[1]

$$F = C(\Lambda)\mu|u|R_S\frac{l}{h_0}. \quad (14)$$

The force coefficient $C(\Lambda)$ gives the graph in Fig. 3.

REFERENCES

1. L. Prandtl, in *Proceedings of General Discussion on Lubrication and Lubricants* (Inst. Mech. Engrs., London, 1937), Vol. 1, pp. 241–248.
2. G. I. Taylor, in *Proceedings of Symposium on Cavitation in Real Liquids, Gen. Motors Res. Lab., Warren, Mich., 1962* (Elsevier, London, 1964), pp. 80–101.
3. G. Birkhoff, in *Proceedings of Symposium on Cavitation in Real Liquids, Gen. Motors Res. Lab., Warren, Mich., 1962* (Elsevier, London, 1964), pp. 102–121.
4. J. W. S. Rayleigh, Philos. Mag. **34**, 97 (1917).
5. O. V. Voinov, Prikl. Mekh. Tekh. Fiz., No. 3, 94 (1979).
6. O. V. Voinov and A. M. Golovin, Izv. Akad. Nauk SSSR, Ser. Mekh. Zhidk. Gaza, No. 3, 117 (1970).
7. O. V. Voinov, Prikl. Mekh. Tekh. Fiz., No. 4, 182 (1973).
8. O. V. Voinov and A. G. Petrov, Dokl. Akad. Nauk SSSR **210**, 1036 (1973) [Sov. Phys. Dokl. **18**, 372 (1973)].
9. O. V. Voinov and A. G. Petrov, Prikl. Mat. Mekh. **39** (5), 845 (1975).
10. O. V. Voinov, J. Fluid Mech. **438**, 247 (2001).
11. L. Floberg, in *Cavitation and Related Phenomena in Lubrication: Proceedings of the I Leeds-Lyon Symposium on Tribology* (Dep. Mech. Eng., Univ. Leeds, London, New York, 1974), p. 31.
12. H. W. Swift, in *Proceedings of the Institute of Civil Engineers, London, 1932,* Vol. 233, Part 1, pp. 267–288.
13. W. Stieber, *Das Schwimmlager* (V.D.I., Berlin, 1933).
14. O. Reynolds, Philos. Trans. R. Soc. London **177**, 157 (1886).
15. A. T. J. Hayward, Usp. Fiz. Nauk **108** (2), 303 (1973) [Am. Scientist **59**, 434 (1971)].
16. A. Prokunin, *Abst. XX Intern. Congr. Theor. and Appl. Mech*., p. 78.

[1] A similar formula was used by A.N. Prokunin and me to explain experimental data [16] on the motion of a particle along a wall in a fluid.

Translated by V. Bukhanov

Doklady Physics, Vol. 47, No. 12, 2002, pp. 900–904. From Doklady Akademii Nauk, Vol. 387, No. 6, 2002, pp. 772–776.

MECHANICS

Dynamics of Decaying Two-Dimensional Turbulence[1]

A. L. Tseskis

Presented by Academician G.S. Golitsyn April 4, 2002

Received April 8, 2002

In this paper, the qualitative shape of the function $T(k)$ (k is the wave number) that characterizes the energy transfer in two-dimensional decaying turbulence is found. (As usual, we imply turbulent motion beyond the grid [1]; such turbulence can be considered as the free motion of a fluid with an initial random velocity distribution.) The corresponding properties of correlation functions, namely, two-point third moments whose sign, in contrast to the three-dimensional case, turns out to be anomalous (positive) in a certain region, are also obtained. In addition, the sign of the third moment in self-similarity intervals and directions of the energy and enstrophy fluxes are unambiguously determined by the shape of the function $T(k)$. The shape of the correlation functions in the self-similarity intervals, which is consistent with experimental data [2], is determined from a two-dimensional analogue of the Karman–Howarth equation.

1. The usual methods for the description of two-dimensional turbulence, which were originated in [3], are based on the concept of turbulent motion as randomly forced turbulence. In such a situation, energy fluxes and enstrophy fluxes are determined not by the dynamics of motion as such but by intuitive reasoning that the fluxes are directed to the right and to the left from the hypothetical spectral region into which the energy is injected. (Note that in the presence of an external energy source, the Karman–Howarth equation becomes inapplicable.) On the other hand, in direct experimental investigations of two-dimensional turbulence in thin liquid films (this possibility was first proposed in [4]), the case of "classic" unforced decaying turbulence is realized. Note that such decaying turbulence is unsteady, in contrast to the forced turbulence, which can be considered as stationary, at least in theory. The shape of the functions for the second and third two-point moments of the velocity field was established in the experiments described in [2]. The anomalous behavior of the third moment is radically different from the case of three-dimensional turbulence (and from the corresponding results for two-dimensional forced turbulence). Below, the general description of the decay of isotropic two-dimensional turbulence is given (allowing the consistency of its correlative and spectral properties with conservation laws to be established), which explains, in particular, the experimental data mentioned above.

The basis for the description of the isotropic turbulence is the Karman–Howarth equation. This equation is the exact consequence of the Navier-Stokes equation or its spectral form

$$\frac{\partial E(k, t)}{\partial t} = T(k, t) - 2\nu k^2 E(k, t), \tag{1}$$

where E is the energy spectrum; $\int E(k, t)dk = \frac{1}{2}\langle \mathbf{v}^2 \rangle$ ($\mathbf{v}$ is the velocity; the density of the fluid is equal to unity; brackets denote statistical averaging); $T(k, t)$ is the function specifying the energy flux in $\mathbf{k}$ space and is linked with nonlinear terms in the equations of motion; and ν is viscosity. Equation (1) is valid for the case of both two and three dimensions. Thus, the difference between two-dimensional and three-dimensional situations is reduced to the fact that, in addition to the energy-conservation law expressed in the form

$$\int_0^\infty T(k, t)dk = 0, \tag{2}$$

the enstrophy-conservation law in the two-dimensional case (at zero viscosity)

$$\int_0^\infty k^2 T(k, t)dk = 0 \tag{3}$$

is also valid.

We can see from (2) that T as a function of k cannot have the same sign for all values of k. In the three-dimensional case, it is constructed in the following

[1] The article was submitted by the author in English.

Joint Institute for High Temperatures,
Russian Academy of Sciences,
ul. Izhorskaya 13/19, Moscow, 127412 Russia

1028-3358/02/4712-0900$22.00

manner. There exists a certain κ such that $T(k, t) \le 0$ at $k \le \kappa$ and $T(k) > 0$ at $k > \kappa$. In this case, it is evident that

$$\int_0^\infty k^2 T dk > 0. \quad (4)$$

The last inequality corresponds to the usual concepts regarding energy transfer from large-scale to small-scale components, although its proof or the rigorous definition of the conditions for its validity are still unknown. This task is as difficult as integrating the original hydrodynamic equations (relevant reasoning based on the effect of the vortex-tube dilation [5], of course, is not rigorous). This is the shape of $T(k)$, which is confirmed by all experimental data concerning laboratory turbulence (tube and channel flows, decaying turbulence beyond grids, etc.), as well as ocean and atmospheric turbulent motions.

Passing to the two-dimensional case, we can now easily see that condition (3) excludes such a shape of the spectrum. Indeed, assuming that $T(k)$ changes its sign at a certain point κ, by virtue of the mean-value theorem, we obtain from expressions (2) and (3)

$$\begin{aligned} \int_0^\kappa T dk + \int_\kappa^\infty T dk &= 0, \\ p^2 \int_0^\kappa T dk + q^2 \int_\kappa^\infty T dk &= 0, \end{aligned} \quad (5)$$

where $p < \kappa$ and $q > \kappa$. Since set (5) is inconsistent at non-zero values of the integrals and p and q, such a shape of the spectrum is impossible, which is why the function $T(k)$ changes its sign more than once. Therefore, in this case, the simplest choice corresponds to the double change in the sign of $T(k)$, which is schematically presented in Fig. 1. It is easy to see that the function $-T(k)$ symmetric (with respect to k axis) to the function $T(k)$ also satisfies conditions (2) and (3). As in the three-dimensional case, the theoretical choice between $T(k)$ and $-T(k)$ is not possible and can be made only by analysis of experimental data. In order to do this, we do the following. Since third-moment data were also obtained in [2] for the smallest values of r situated outside the inertial intervals, we can compare with them the function D_{LLL} (or, which is the same, the function $B_{LL,\,L}$, whose definitions are given below) linked at small r with $T(k)$ by a certain exact relation. Deriving this relation, we note beforehand that, by virtue of relationships (2) and (3), for the chosen sequence of signs in $T(k)$, the following inequality is valid:

$$\int_0^\infty k^4 T dk < 0,$$

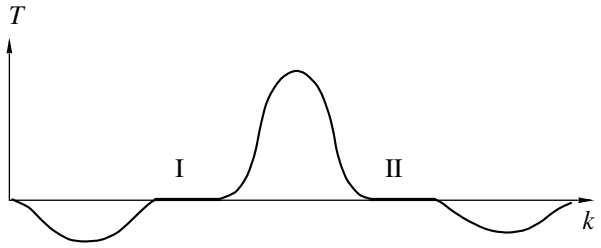

Schematic shape of the function $T(k)$.

which we will need below. In order to prove the validity of this inequality, we consider the function

$$S(z) = \int_0^z T dk.$$

For this function, the relations following from (2) and (3), as well as from its definition, are valid:

$$S(0) = S(\infty) = 0, \quad \int_0^\infty k S dk = 0,$$

$$\int_0^\infty k^4 T dk = -4 \int_0^\infty k^3 S dk.$$

As is easy to see, the quantity S changes its sign, namely, from negative to positive, only once. Thus, by virtue of the mean-value theorem, the last integral is positive, so that the statement to be proved follows from the last of these relations.

Furthermore, in order to derive the desired relationship, we should use the relation between the correlation tensor $B_{lm,\,n}(r)$ and its Fourier transform expressed in terms of the scalar function $F_3(k)$ [1]:

$$B_{lm,\,n} = i \int e^{i\mathbf{kr}} F_3 \left(\frac{\delta_{mn} k_l}{k} + \frac{\delta_{ln} k_m}{k} - \frac{2 k_l k_m k_n}{k^3} \right) d\mathbf{k}.$$

Using now the identity

$$\int e^{i\mathbf{kr}} k_l F(k) d\mathbf{k} = -\frac{i\partial}{\partial r_l} \int e^{i\mathbf{kr}} F(k) d\mathbf{k}$$

and expressing the tensor $B_{lm,\,n}$ in terms of $B_{LL,\,L}$ (the relation corresponding to the two-dimensional case can be found in [6]), we integrate over the angular variable with allowance for the known identity

$$\int_0^\pi e^{ikr\cos\theta} d\theta = \pi J_0(kr).$$

Thus, we obtain after relatively simple but cumbersome

calculations

$$B_{LL,L} = \frac{1}{2}\int_0^\infty \left[\frac{J_0''}{kr} - \frac{J_0'}{(kr)^2}\right]\frac{T(k)}{k}dk \qquad (6)$$

[in the two-dimensional case, $T(k) = 4\pi k^2 F_3$], where the prime corresponds to the derivative of the Bessel function J_0 over its argument. Expanding J_0 into the power series in kr, we finally obtain from (6)

$$B_{LL,L} = \frac{1}{2}\int_0^\infty \left[\frac{kr}{8} - \frac{(kr)^3}{96} + \frac{3(kr)^5}{16(4!)^2} - \ldots\right]\frac{T(k)}{kdk}.$$

Because of the presence of two (but not one as in three-dimensional hydrodynamics) conservation laws (2) and (3), the first nonvanishing term in the expansion of $B_{LL,L}$ (having here fifth order over r) takes the form

$$B_{LL,L} = \frac{r^5}{3\times 2^{11}}\int_0^\infty k^4 T dk. \qquad (7)$$

Since the integral on the right-hand side of expression (7) is negative, the function $B_{LL,L}(r)$ must also be negative at small r. The latter fact is actually verified in the experiments [2]. Therefore, the above results correspond to the known experimental data and allow us to establish a possible shape of $T(k)$ characterizing an important property of turbulent motion, namely, the energy transfer in wave-number space. Below, we use this result for the determination of the third-moment signs and directions of energy fluxes and enstrophy fluxes in self-similarity intervals.

2. In order to link the spectra and correlation functions with the function $T(k)$, we should use exact dynamic equations. Turning first to relationship (1), we show, as a by-product, how the known self-similar spectra can be obtained and, what is more important, how exactly their location along the k axes is associated with the shape of $T(k)$. Since the solutions to two-dimensional hydrodynamic equations as $\nu \longrightarrow 0$ convert to the solutions with $\nu = 0$, we can omit for simplicity the last term on the right-hand side of (1). The integrals

$$\varepsilon(z) = \int_0^z T dk, \quad \varepsilon_\omega(z) = \int_0^z k^2 T dk, \qquad (8)$$

apparently yield the change in the energy and enstrophy, respectively, per unit time within the interval $[0, z]$ in $\mathbf{k}$ space. In the regions I and II shown in figure, these integrals are independent of z, and thus the self-similarity hypothesis can be used for the corresponding intervals of the $E(k)$ spectrum (note that the presence of such regions with $T(k) = 0$ is, generally speaking, a necessary condition for Kolmogorov self-similarity [1]). According to this hypothesis, the quantity $E(k)$ is defined by the combination of one of the quantities in (8) and of the wave number k, i.e., the combination having the necessary dimensionality. In this case, the predominant quantity should be chosen from ε and ε_ω . In contrast to the usual approach [3], for which arbitrary assumptions concerning directions of fluxes in the inertial ranges are made, in this case, they are uniquely associated with the shape of the function $T(k)$.

Certainly, it is impossible to directly compare the values of ε and ε_ω, which have different dimensionalities. Therefore, we consider the dimensionless ratio

$$\varphi = \frac{|\varepsilon_\omega|\lambda^2}{|\varepsilon|}, \qquad (9)$$

where λ is the differential scale of turbulent motion [1], which remains invariable at zero viscosity. It is evident now from relationship (9) that the quantities ε and ε_ω predominantly affect the spectrum at $\varphi \ll 1$ and $\varphi \gg 1$, respectively. As follows from the shape of $T(k)$ (due to the presence of the factor k^2 in the integrand for ε_ω), it can be only

$$\varphi \ll 1 \text{ in region I,}$$

$$\varphi \gg 1 \text{ in region II.}$$

Composing, as usual, combinations of a proper dimensionality, which contain k and, correspondingly, ε and ε_ω, we arrive at

$$\begin{aligned} E(k) &\sim |\varepsilon|^{2/3} k^{-5/3} \quad \text{in region I,} \\ E(k) &\sim |\varepsilon_\omega|^{2/3} k^{-3} \quad \text{in region II.} \end{aligned} \qquad (10)$$

In this case, the energy fluxes and enstrophy fluxes have the same directions for the chosen shape of $T(k)$: they are positive in region I (the energy and enstrophy are transferred from large scales to small scales) and negative in region II. It is easy to see that this pattern corresponds to the turbulent-energy concentration in the interval located between the regions I and II. It is clear that a change in the sign of $T(k)$ would lead to the opposite result, namely, an increase in the energy to the left from the region I and to the right from the region II (which is usually considered to be realized when injecting the energy into certain narrow interval of the spectrum [3]).

It is worth noting that ignoring the viscous dissipation, in fact, should be expressed by the inequalities

$$2\nu\int k^2 E dk \ll |\varepsilon|, \quad 2\nu\int k^4 E dk \ll |\varepsilon_\omega|.$$

Based on the reasoning above, these relationships can be fulfilled in the two-dimensional case but can never

be fulfilled in the three-dimensional case because of the so-called enstrophy catastrophe:

$$\lim_{\nu \to 0} \nu \int_0^\infty k^2 E dk \neq 0.$$

This makes the energy dissipation a single quantity that determines the self-similarity of the inertial segment in the three-dimensional turbulence spectrum.

As is well known, further use of Kolmogorov's hypotheses on the local structure of the velocity field makes it possible to obtain in the three-dimensional case, in addition to the spectrum, both qualitative and quantitative characteristics of the second and third moments of the velocity field [1, 7]. These characteristics turn out to be in good agreement with available experimental data. This possibility follows from the existence of a quantity (averaged dissipation of turbulent energy) determining the dynamics of the decay as a whole. It manifests itself formally by the fact that, on the left-hand side of the equation describing the velocity-field correlator D_{LL} (the standard notation is used below: the correlation functions $B_{LL}(r) = \langle u_L(\mathbf{x}) u_L(\mathbf{x} + \mathbf{r}) \rangle$, $B_{LL,L}(r) = \langle u_L(\mathbf{x}) u_L(\mathbf{x}) u_L(\mathbf{x} + \mathbf{r}) \rangle$, u_L is the velocity component aligned in parallel to the straight line connecting points $\mathbf{x}$ and $\mathbf{x} + \mathbf{r}$; the structural functions are $D_{LL}(r) = 2[B_{LL}(0) - B_{LL}(r)]$, $D_{LLL}(r) = 6B_{LL,L}(r)$, there exists a difference between the quantities $\frac{\partial B_{LL}}{\partial t}$ and $\frac{1}{2}\frac{\partial D_{LL}}{\partial t}$. According to the Kolmogorov theory, the second of them becomes zero in the inertial interval. More accurately, we should state [7] that

$$\frac{1}{2}\left|\frac{\partial D_{LL}(r,t)}{\partial t}\right| \ll \left|\frac{\partial B_{LL}(0,t)}{\partial t}\right| = \frac{2}{3}|\varepsilon|. \qquad (11)$$

In the two-dimensional case, by virtue of the above reasons, the energy dissipation cannot determine the dynamics of the decaying turbulence. Hence, ignoring it (together with ignoring viscosity) leads to the situation when the time derivative D_{LL} remains in the corresponding equation. Consequently, in this situation, we can consider the equation for B_{LL}, which takes the form [6]

$$\frac{\partial B_{LL}}{\partial t} = \left(\frac{\partial}{\partial r} + \frac{3}{r}\right) B_{LL,L}. \qquad (12)$$

Each of the two inertial intervals (corresponding to the spectra $k^{-5/3}$ and k^{-3}) is characterized by the quantities ε and ε_ω, respectively. Combining them with r in order to obtain the same dimensionality as for $\frac{\partial B_{LL}}{\partial t}$, we pass from (12) to the following equations (C_1, C_2 are positive dimensionless constants):

$$\begin{aligned} C_1 \varepsilon &= \left(\frac{\partial}{\partial r} + \frac{3}{r}\right) B_{LL,L} \quad \text{in region I,} \\ C_2 \varepsilon_\omega r^2 &= \left(\frac{\partial}{\partial r} + \frac{3}{r}\right) B_{LL,L} \quad \text{in region II.} \end{aligned} \qquad (13)$$

Multiplying expression (13) by r^3 and integrating with allowance for the condition $B_{LL,L}(0, t) = 0$, we obtain

$$\begin{aligned} B_{LL,L} &= \frac{C_1}{4}\varepsilon r \quad \text{in region I,} \\ B_{LL,L} &= \frac{C_2}{6}\varepsilon_\omega r^3 \quad \text{in region II.} \end{aligned} \qquad (14)$$

Therefore, the dependence $B_{LL,L}$ on r (and also $D_{LLL}(r)$) within the inertial interval determined by the energy transfer is reduced to the linear one, since it takes place in the three-dimensional case as well. Within the range of the inverse enstrophy flux, the corresponding dependence appears to be cubic, as follows from the result obtained by a different method in [8]. However, in contrast to the three-dimensional case, it follows from (14) that the opposite signs of the third moment correspond to the intervals I and II [we note that ε and ε_ω have different signs, as follows from (2) and (3)]. In particular, relations (14) show that for the given shape of $T(k)$, we have $B_{LL,L} < 0$ within region I and $B_{LL,L} > 0$ within region II. Since lower values of r correspond to higher values of the wave vector, the function $B_{LL,L}$ must be positive in a certain interval and must become negative to the right of this interval. In this case, positive and negative values of $B_{LL,L}$ correspond to the k^{-3} and $k^{-5/3}$ spectrum, respectively. Such a pattern radically differs from the third-moment behavior in the three-dimensional case, when it is negative within the entire inertial range (and it is certainly different from that for the forced two-dimensional turbulence [3]) (see also [9], where energy-injection intervals different from those of [3] are considered).

The above anomaly was actually observed in the recent experiments of [2] with turbulence generated by a two-dimensional comb in a thin liquid film. In this case, a part of the spectrum with the shape close to k^{-3} was found. This part corresponded to positive values of $B_{LL,L}$ (at the same time, the result for the second moment close to $D_{LL} \sim r^2$ was obtained as was expected in the case of $B_{LL,L} \sim r^3$). However, an interval that could be identified as the $k^{-5/3}$ spectrum was not observed. Apparently, this is associated with both the insufficiently high Reynolds number (on the order of several hundred) and the fact that the largest length scales corresponding to the k^{-3} spectrum part were comparable to the exterior scale of turbulent motion.

Thus, as in the three-dimensional case, the use of exact dynamic equations combined with the self-similarity hypothesis allowed us to obtain for decaying two-dimensional turbulence general results concerning both the shape of the function $T(k)$ and details of the behavior of the spectrum and correlation functions in the self-similarity intervals.

REFERENCES

1. A. S. Monin and A. M. Yaglom, *Statistical Fluid Mechanics* (MIT Press, Cambridge, 1975; Gidrometeoizdat, St. Petersburg, 1996), Vol. 2.
2. A. Belmonte, W. I. Goldburg, H. Kellay, *et al.*, Phys. Fluids **11**, 1196 (1999).
3. R. H. Kraichnan, Phys. Fluids **10**, 1417 (1967).
4. Y. Couder, J. Phys. Lett. **45**, L353 (1984).
5. G. I. Taylor, Proc. R. Soc. London, Ser. A **164** (918), 15 (1938).
6. A. L. Tseskis, Izv. Akad. Nauk SSSR, Mekh. Zhidk. Gaza, No. 5, 19 (1987).
7. L. D. Landau and E. M. Lifshitz, *Course of Theoretical Physics*, Vol. 6: *Fluid Mechanics* (Nauka, Moscow, 1986; Pergamon, New York, 1987).
8. G. Falkovich and V. Lebedev, Phys. Rev. E **49**, R1800 (1994).
9. E. Lindborg, J. Fluid Mech. **388**, 259 (1999).

Doklady Physics, Vol. 47, No. 12, 2002, p. 905.

ERRATA

Erratum: "Change in the Parameters of Surface Thermal Decomposition of Energy-Intensive Materials Near the Phase-State Boundary" [*Doklady Physics* 47, 571 (2002); *Doklady Akademii Nauk* 385, 482 (2002)]

O. F. Shlenskiĭ and Yu. V. Zelenev

In our paper entitled "Change in the Parameters of Surface Thermal Decomposition of Energy-Intensive Materials Near the Phase-State Boundary" published in Doklady Akademii Nauk **385**, 482 (2002) [Doklady Physics **47**, 571 (2002)], expressions (11) and (12) should have the form

$$u = \frac{k\delta}{f} = \sqrt{\frac{ak}{f}} = \frac{a}{\delta}, \tag{11}$$

$$T_{\Pi} = Qf_0\frac{1 - cak/f}{C_p} + T_0. \tag{12}$$

In the first line above Eq. (12), the expression for the velocity should be read as $u^2 = \frac{ka}{f}$.

Translated by G. Merzon

1028-3358/02/4712-0905$22.00